nature neuroscience

Article

https://doi.org/10.1038/s41593-025-01894-6

Synaptic plasticity rules driving representational shifting in the hippocampus

Received: 16 October 2023

Accepted: 17 January 2025

Published online: 20 March 2025

Check for updates

Antoine D. Madar[1] ✉, Anqi Jiang[1], Can Dong[1,2] & Mark E. J. Sheffield[1] ✉

Synaptic plasticity is widely thought to support memory storage in the brain, but the rules determining impactful synaptic changes in vivo are not known. We considered the trial-by-trial shifting dynamics of hippocampal place fields (PF) as an indicator of ongoing plasticity during memory formation and familiarization. By implementing different plasticity rules in computational models of spiking place cells and comparing them to experimentally measured PFs from mice navigating familiar and new environments, we found that behavioral timescale synaptic plasticity (BTSP), rather than Hebbian spike-timing-dependent plasticity (STDP), best explains PF shifting dynamics. BTSP-triggering events are rare, but more frequent during new experiences. During exploration, their probability is dynamic—it decays after PF onset, but continually drives a population-level representational drift. Additionally, our results show that BTSP occurs in CA3 but is less frequent and phenomenologically different than in CA1. Overall, our study provides a new framework to understand how synaptic plasticity continuously shapes neuronal representations during learning.

Since Donald Hebb's influential postulate, learning and the encoding of memories are assumed to be mainly supported by activity-dependent synaptic plasticity[1,2]. The dependencies of long-term plasticity (LTP) on neuronal activity have been studied for decades, but mostly in vitro[3–5]. Yet, because directly measuring both neuronal activity and synaptic changes in vivo in large populations of neurons remains a technical challenge, little is known about the plasticity rules at play during behavior[6–8].

Even in the hippocampus, a brain area essential for memory[9] and where synaptic plasticity has been investigated most intensively[10,11], the learning rules that shape neuronal representations are only starting to be understood. For example, during familiarization with an environment by repeated unidirectional exploration, spatial representations in the CA1 subfield of the hippocampus gradually drift backwards[12–17]. This form of fast representational drift, which correlates with incidental behavioral learning and is dependent on the molecular machinery for LTP[18–20], could support continual memory updating during ongoing experience and help pattern separation to discriminate events close in time[21,22]. The population backward drift is faster in new environments, slows down with familiarization and occurs to a lesser degree in CA3, the main source of inputs to CA1 (ref. 12,17). Overall, this drift, resulting from shifts in the position of individual place fields (PF), is thought to reflect ongoing synaptic plasticity. However, the precise rules and mechanisms explaining differences between familiarity levels and hippocampal subfields are unknown.

A fruitful approach to uncover the synaptic mechanisms supporting cognition has been to use computational modeling to infer the rules that would best fit in vivo recordings[6,23]. Early computational models suggested that classic Hebbian spike-timing-dependent plasticity (STDP)[24] could cause individual PFs to shift backwards[15,25]. The mechanism is intuitive—the asymmetry of the rule favors potentiation of inputs that fire before the output place cell and depress inputs that fire after, such that, combined with repeated unidirectional track traversals, the output cell fires earlier on the track. However, these models were proof-of-concepts that used parameters potentially inflating the effects of STDP without systematically exploring the parameter space. As such, they do not account for the diversity in the dynamics of single PFs, which do not all shift backward and can occasionally shift forward, nor do they explain differences between hippocampal subfields and familiarity levels[12]. Moreover, the effect of classic STDP

[1]Department of Neurobiology, Neuroscience Institute, University of Chicago, Chicago, IL, USA. [2]Present address: Department of Neurobiology, Stanford University School of Medicine, Stanford, CA, USA. ✉e-mail: madar@uchicago.edu; sheffield@uchicago.edu

was not compared to other phenomenological rules. Indeed, classic STDP is an imperfect way to describe synaptic plasticity. First, the STDP kernel itself can vary in shape and amplitude at CA3–CA1 synapses, depending on induction protocols[26,27]. Furthermore, Hebbian STDP rules, in general, have been undermined because (1) their impact may be too weak in natural regimes of firing and physiological conditions[7,26,28] and (2) they operate on timescales too short to support associative memory with long delays[29].

A promising alternative to explain PF dynamics could be behavioral timescale synaptic plasticity (BTSP), a type of non-Hebbian plasticity recently discovered at the CA3–CA1 pyramidal synapse[5,23,30,31]. BTSP has the following three main differences with STDP: (1) It is triggered by rare but large dendritic calcium plateau potentials generally accompanied by a somatic burst of activity called a complex spike, (2) the induced synaptic changes are larger and (3) it operates on the timescale of seconds. So far, BTSP has mostly been considered as a mechanism underlying PF emergence[5,16,31] or remapping[23]. Yet, because dendritic plateaus can spontaneously occur in neurons with an already established PF[31–33] and cause a PF translocation[23], we hypothesized that a series of BTSP-triggering plateaus during exploration could lead to a PF shifting backward or forward, depending on the probability and location of such events.

Here we used computational modeling to test the effect of different STDP and BTSP rules on PF shifting and compared our simulations to experimental observations from large populations of CA1 and CA3 neurons. The large sample size afforded by two-photon calcium imaging allowed us to accurately assess the variability in the shifting dynamics of single PFs. From this, we inferred that BTSP is more likely than STDP to support the evolution of hippocampal representations during learning, we deduced differences in the phenomenology of BTSP in CA1 versus CA3 and determined the dynamics of BTSP-triggering events as a function of familiarity.

Results

To assess the synaptic plasticity rules at play in the hippocampus during familiarization to new experiences, we used our previously published dataset of CA1 and CA3 pyramidal cells recorded in wild-type mice with two-photon calcium imaging[12]. Eleven animals (four for CA1 and seven for CA3) were recorded while unidirectionally running multiple laps through a virtual linear track in a familiar environment and then switched to a new virtual environment (Methods). We considered the lap-by-lap dynamics of the center-of-mass (COM) of individual PFs (2,235 in CA1 and 414 in CA3) as a proxy for ongoing reorganization of their synaptic weights. Our approach was (1) to characterize PF COM dynamics, and the differences between hippocampal subfields and familiarity levels, and (2) to model different plasticity rules and explore their parameter space to match the experimental data and infer the mechanisms that control different aspects of PF dynamics.

As reported in ref. 12, we found that many PFs are stable from lap to lap, whereas some seem to linearly shift their position, usually backward but occasionally forward (Fig. 1a). Here, we quantified shifting dynamics by performing a linear regression on the COM trajectory of each PF (Fig. 1a,b). For all experimental conditions, there was a sizeable proportion of significantly shifting PFs, spanning a large range of shifting speeds. There were also clear differences between hippocampal subfields and familiarity levels (Fig. 1b and Supplementary Fig. 1). CA3 had a lower proportion of significantly shifting PFs, and shifts were slower than in CA1, particularly in the new environment. Familiarity had a strong effect on the proportion of shifting PFs, with a large decrease in backward-shifting PFs in familiar contexts for both CA1 and CA3. There is also a noticeable increase of forward-shifting PFs in the familiar context, this increase being larger in CA3 than in CA1 (Fig. 1b,c). These effects were consistent across all mice (Supplementary Fig. 1).

STDP is too weak to explain PF shifting dynamics

Past computational studies suggested that backward shifting in CA1 could result from STDP at synapses from CA3 spatially modulated inputs[15,25,34]. We thus sought to determine whether the distribution of PF shifts that we observed could be explained by such classic Hebbian plasticity.

First, we experimentally checked whether PF shifting in CA1 depends on CA3. To do this, CA1 neurons were recorded while a subset of CA3 axons in the field-of-view were optogenetically inhibited (Fig. 1d(i)–(iii) and Supplementary Fig. 2; Methods). This subtle manipulation led to a significant decrease in the proportion of shifting PFs, demonstrating that CA3 inputs are an important driver of CA1 shifting dynamics.

Then, we designed a simple model of a spiking place cell with stochastic and plastic inputs following a classic STDP rule (Fig. 2a,b; Methods). Our model is inspired by seminal studies[15,25] but differs from them in several ways (Supplementary Table 2; Methods). Importantly, input parameters were adjusted to ensure a realistic output, with firing rates and PF widths as measured from CA1 recordings in mice (Supplementary Fig. 3 and Fig. 2c(i)–(iv)). In contrast to past reports, this model produced few significantly backward shifting PFs, with a narrow range of small shifting speeds (Fig. 2c(i)–(iv)) unlike what we observed experimentally in CA1 (Figs. 1b and 2e). Past models used higher firing rates, which led to a higher number of pre-post spike pairs and consequently increased the impact of STDP. We thus varied input parameters (Fig. 2f(i)) to cover a wide range of realistic and unrealistic output firing rates (Fig. 2f(ii) and Supplementary Fig. 3d). Consistent backward shifting occurred only for unrealistically high output firing rates (Fig. 2f(i),(ii)). Moreover, high firing rates were not able to produce the large range of shifting speeds observed in our recordings, with shifting being exclusively backward and shifting speeds still constrained to small values (Fig. 2d(iii), e (top), f(ii)).

We explored the parameter space of our model extensively, but no set of parameters offered a good match to the data (Supplementary Figs. 4–10). Using CA3-like dynamic input PFs rather than static ones (Supplementary Fig. 4) improved the proportion of shifting PFs, but still yielded only small shifting speeds (Fig. 2e and Supplementary Fig. 7). Increasing the effect of STDP by allowing runaway potentiation and making the model more realistic by adding spike-rate adaptation to the output neuron and adding a dynamic delay in the update of synaptic weights did not improve the fit (Supplementary Fig. 5). Increasing the animal speed, which also amplifies the effect of STDP on backward shifting (because of the unidirectional movement) did not alter our conclusions either (Supplementary Figs. 7–9). Because we do not know the exact amplitude and timescale of weight changes due to STDP[4] ('Parameterization'), we tested different combinations of parameters for the STDP rule (Supplementary Figs. 8–10). Realistic variations in the amplitude of weight changes and the time constants did not change our results; only unrealistically high values yielded consistent backward shifting (Supplementary Figs. 8,9b,c), without ever matching the range of shifting speeds of our experimental data. Overall, the main effect of STDP is not PF backward shifting, which is weak, but it is an increase in output firing rates leading to PF enlargement (Supplementary Figs. 5d,6,8–10g,h,j,k). In contrast, PF width changes are heterogeneous in CA1, both in our recordings (Supplementary Fig. 4i–j) and across past studies[13,14,17]. The PF enlargement predicted by STDP models is thus inconsistent with experimental observations, providing additional evidence that classic STDP is unlikely to underlie lap-by-lap changes in hippocampal PFs. STDP models used above only consider interactions between pairs of input–output spikes. However, past studies have suggested that experimentally observed synaptic weight changes can be better explained when considering interactions between triplets of spikes[35,36]. STDP triplet rules have also been shown to account for the firing rate dependency of STDP experiments[35]. We thus adapted our model to check the effect of STDP triplet rules

https://doi.org/10.1038/s41593-025-01894-6

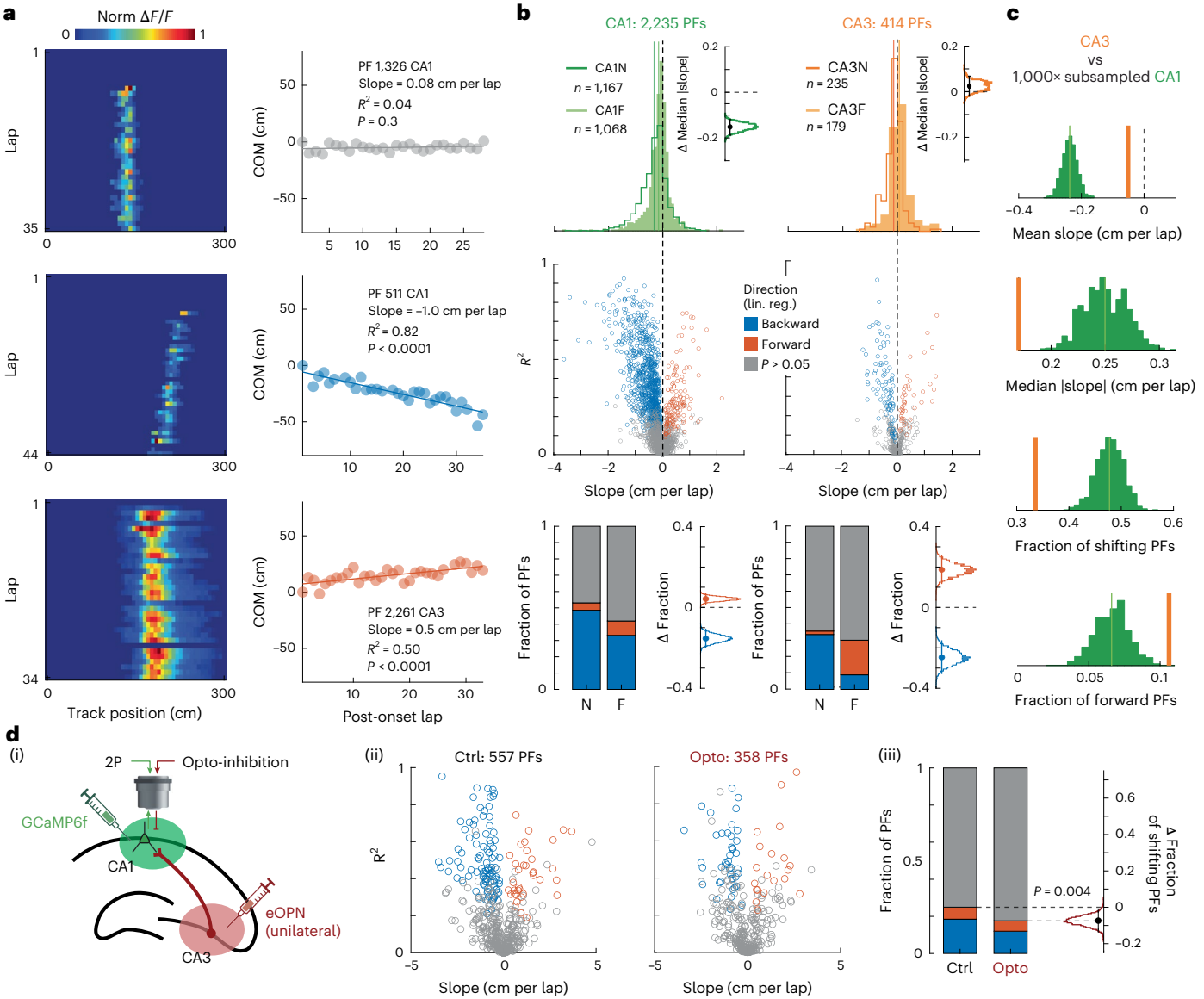

Fig. 1 | Linear shifting of PFs in CA1 and CA3 in new and familiar environments. **a**, Left, examples of CA1 and CA3 PFs recorded using two-photon calcium imaging. Right, linear regression on the onset-centered PF COM was used to classify each PF as shifting backward (blue), forward (red) or nonsignificantly shifting (gray). Regression significance assessed with *F* test. **b**, Characterization of PF linear shifting in CA1 (left) and CA3 (right) for PFs defined over a span of at least 15 laps. Top, probability density distributions of slopes (that is, shifting speeds) for all PFs in CA1 and CA3 during navigation along a new (N) or familiar (F) virtual track (CA1N, 1,167 PFs; CA1F, 1,068 PFs; CA3N, 235 PFs and CA3F, 179 PFs). Delta plots (F-N bootstrapped difference; error bars, 95% CI of the mean) indicate that absolute shifting speed significantly decreases with familiarity in CA1 but not CA3. Middle, estimated shifting speed versus linear regression fit (R^2) for individual PFs. Bottom, proportion of backward, forward and nonsignificantly shifting PFs in each hippocampal subfield and condition. Delta plots indicate that the fraction of backward PFs significantly decreases in F whereas the fraction of forward PFs increases substantially, strongly in CA3 and weakly in CA1. **c**, Resampling exact tests controlling for the sample size difference between CA1 and CA3 (familiar and new environments combined). A total of 414 of the 2,235 CA1 PFs were randomly resampled 1,000 times to match CA3. The CA3 value was outside the resampled distribution for all statistics (green distribution), showing a significant difference between CA1 and CA3. **d**, Linear shifts in CA1 during optogenetic inhibition of projections from CA3 during exploration of a new environment. (i), Experimental setup (graphics made with BioRender.com). (ii), Distributions of slopes (pooled from nine mice) for Ctrl and Opto conditions. Median absolute slopes were similar (bootstrap exact test on difference, $P = 0.5$). (iii), Inhibition of CA3 inputs substantially reduced the fraction of significantly shifting PFs (bootstrap exact test, $P = 0.004$). CI, confidence interval.

on PF shifting. These simulations confirmed that STDP at spatially modulated excitatory synapses does not produce shifting like in CA1 (Supplementary Fig. 11).

BTSP explains PF shifting dynamics in CA1 and CA3

We next tested whether BTSP could support PF shifting dynamics by designing a new BTSP model that could easily replace the STDP rule in our initial spiking place cell model (Fig. 3a). In contrast to past models that considered BTSP as a bidirectional plasticity rule[23,37], our strategy was to combine a pure potentiation rule as discovered in ref. 30 with a simple homeostatic rule preventing runaway potentiation and maintaining a PF with stable width as observed in recordings from ref. 23. The parameters of our model were optimized to fit the in vitro experiments in ref. 30 (Supplementary Fig. 12) and in vivo results in ref. 23 (Supplementary Figs. 13–15). Our simulations of 'Milstein-type' PF translocation experiments revealed that combining a potentiation rule with homeostatic plasticity can lead to an apparent weight-dependent bidirectional plasticity rule (Supplementary

https://doi.org/10.1038/s41593-025-01894-6

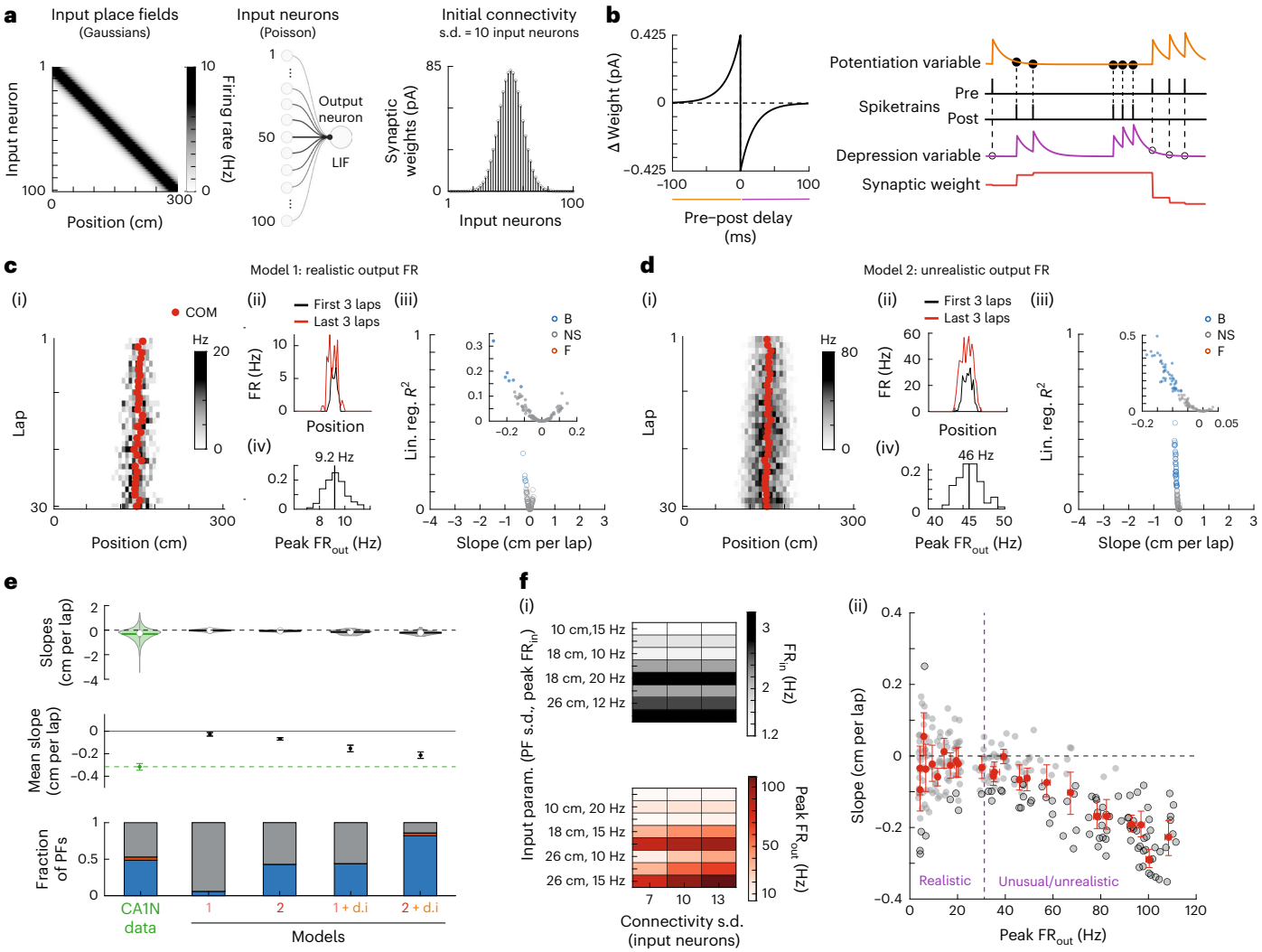

Fig. 2 | STDP does not explain PF shifting in CA1. a, Place cell model (LIF, leaky integrate and fire). **b**, STDP model. **c**, Model 1, baseline parameters as in **a** and **b**. (i) and (ii), Example simulation that resulted in a significantly shifting PF. (i), Lapwise PF (compare with Fig. 1a). (ii), The slight backward shift results from a modest increase in firing rate and PF width. (iii) and (iv), Simulation of 100 PFs with same baseline parameters. (iii), Linear regression fit (R^2) as a function of the shifting speed (regression slope) for 100 simulated PFs. Only a few PFs show a weak but significant backward shift (B). Most PFs show no significant shift (NS) and none show forward shifting (F). (iv), Distribution of the peak firing rate (maximum of the 30-lap average) for all 100 simulated PFs (vertical line is the mean; *y* axis is the fraction of PFs)—output firing rates are realistic (Supplementary Fig. 3). **d**, Same as **c** except a single-input parameter, the peak rate of input PFs, was raised from 10 to 15 Hz. (i) and (ii), Simulated PF with the largest backward shift in **d**(iii). (iii), A large proportion of the 100 simulated PFs significantly but weakly shifted backward. (iv), Output rates are unrealistically high (ref. 61; Supplementary Fig. 3). **e**, Comparison of the shifts measured in CA1 data during navigation of a new environment (same data as in Fig. 1; $n = 1{,}167$ PFs) and four different models ($n = 100$ simulated PFs each)—model 1 (baseline parameters, data in **c**), model 2 with higher input and output firing rates (data in **d**), a modified model 1 with CA3N-like dynamic inputs (d.i.; Supplementary Fig. 4), and a modified model 2 with CA3N-like dynamic inputs. Top, violin plots of the slope distributions (open circle, median; solid line, mean). No model matches the large variance in CA1. Middle, bootstrapped mean slope and 95% CIs of the distributions shown above. The three later models result in consistent backward shifting (significantly below zero) but smaller than in CA1 (green, dashed line). Bottom, model 2 and 1 + d.i. have a proportion of backward shifting PFs (blue) similar to CA1N, but no forward shifting (red). Model 2 + d.i. inherits some forward shifting from the CA3-like dynamic inputs but proportions do not match CA1. **f**, Effect of firing rates on PF shifting induced by classic STDP (Supplementary Fig. 7). (i), A set of three parameters controlling the inputs, and thus the output firing rates, without changing the plasticity rule, were systematically varied to test 24 different conditions. All other parameters were as in **a** and **b**, with static input PFs. Top, the input PF width (PF s.d.) and the peak rate of input PFs (Peak FR_{in}) control FR_{in}, an estimate of the average firing rate of input neurons across the whole track. Bottom, peak FR_{out} (max of 30-lap average PF) averaged across 20 simulated PFs for each condition. (ii), A total of 480 simulated PFs (gray dots, 20 per condition) with significant shifts marked by a black edge. Red dots are means for each condition, with bootstrapped 95% CI in the *x* and *y* axes. For context, the dashed purple vertical line (32 Hz) marks the upper bound from electrophysiological recordings of CA1 PFs in mice (data from ref. 61 adjusted for 6-cm bin size; Supplementary Fig. 3); consistent but modest backward shifting only occurs for unrealistically high output firing rates. Large backward or forward shifts are never observed, not even for highly unrealistic output firing rates.

Figs. 14 and 15) and is appropriate to study the effects of BTSP on PF shifting dynamics (Methods). Overall, the advantage of our model is its simplicity, which allows us to fit the Milstein dataset with a single set of parameters as well as an easy comparison with the parameters of our STDP model from which it was adapted.

To investigate the impact of BTSP on PF shifting during exploration, we simulated PFs as in Fig. 2 but replaced the STDP rule with our BTSP model (Fig. 3a). Because the physiological causes of BTSP-triggering events (referred to in our model as 'complex spikes' (CS)) are not well understood[5], we considered that each output spike

https://doi.org/10.1038/s41593-025-01894-6

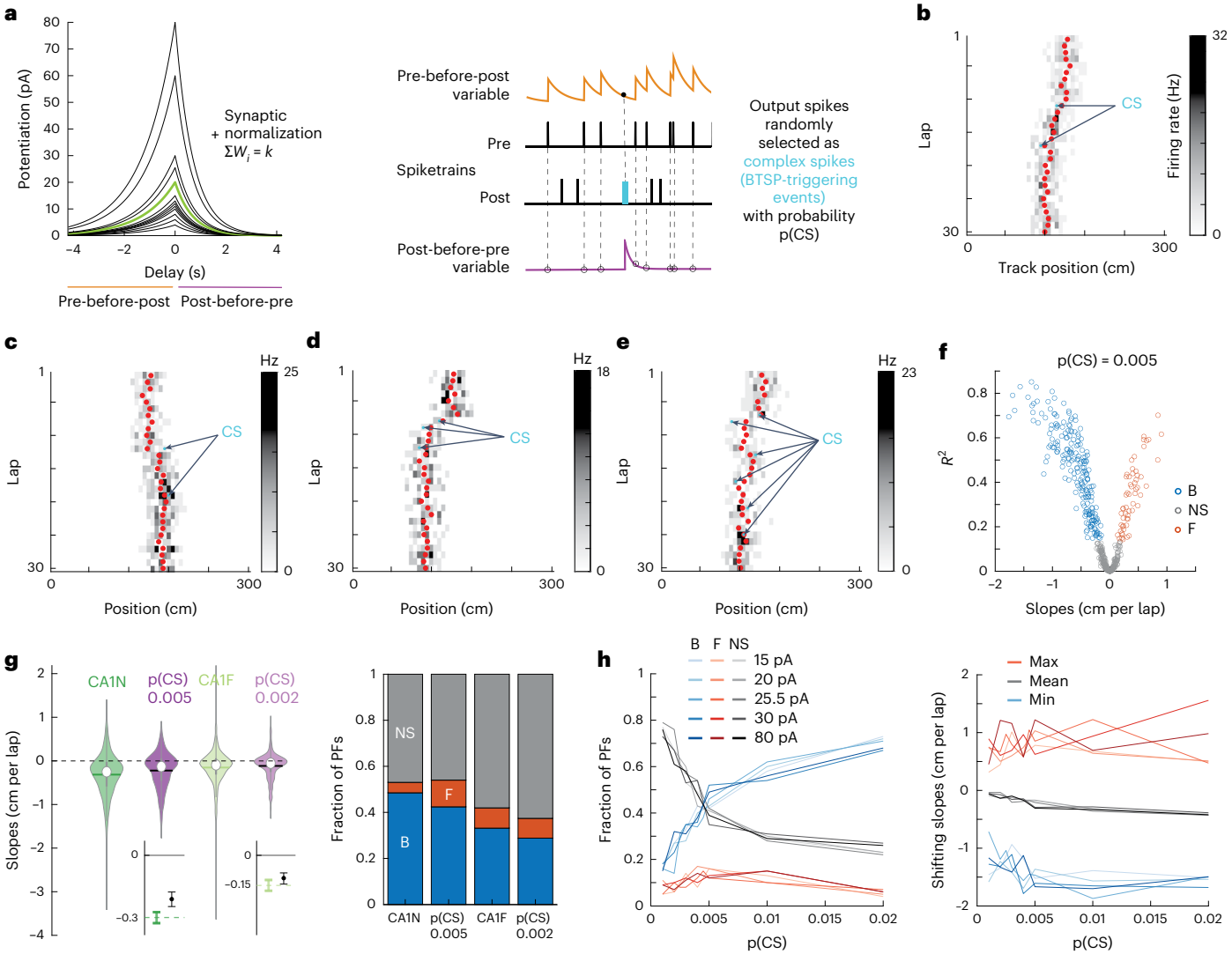

Fig. 3 | BTSP explains PF shifting in CA1. a, Left, plasticity rules tested for optimization (Supplementary Fig. 15h,i). Green—optimized rule. Right, implementation of plasticity adapted from our STDP model. **b**–**e**, Examples of 30-lap simulations of our place cell model with plastic synapses following the optimized homeostatic BTSP rule. Depending on the number and location of complex spikes (CS; cyan dots marked by arrows), the COM trajectory (red dots) can go backward (**b** and **d**) or forward (**c**) and appear somewhat smooth and linear (**b**) or display abrupt shifts and zigzags (**e**). **f**, Simulation of 500 PFs using p(CS) = 0.5% of output spikes. The distribution of backward (B), forward (F) and nonsignificantly (NS) shifting PFs (assessed by linear regression of the COM and *F* test) is reminiscent of CA1 (Fig. 1b). **g**, Comparison of the CA1 data (green, same as in Fig. 1) with two versions of the model where only p(CS) was changed (dark and light purple). Left, violin plots of the shifting speed distributions (median is open circle, mean is solid line and quartiles are gray whiskers). The models ($n = 500$ simulated PFs each) cannot reproduce the most extreme shifts, but the variances are comparable to CA1. Insets show bootstrapped means and 95% CI (significant but small difference between the model and CA1N, nonsignificant for CA1F). Right, proportions of backward, forward and nonsignificantly shifting PFs. The models qualitatively match the data. **h**, Exploration of the parameter space—p(CS) and BTSP amplitude (maximum potentiation before synaptic normalization) were varied systematically. A total of 100 simulated PFs per condition. Left, proportions of backward, forward and nonsignificantly shifting PFs. Right, minimum, mean and maximum shifts. The mean shift monotonically but only slightly decreases with p(CS) due to larger proportions of backward shifting PFs, not by inducing larger shifts.

had the potential to be a BTSP-triggering CS with a certain probability p(CS). Simulations using this strategy could lead to both backward and forward-shifting PFs (Fig. 3b–e). Because of the stochasticity in firing and in determining CSs, the model could produce smooth, sometimes linear-like trajectories (Fig. 3b), but also yield more abrupt shifting when a CS occurred on the edge of the initial PF (Fig. 3d), and even zigzag trajectories when multiple CSs occurred successively on different sides of the PF COM (Fig. 3e). Large-scale simulations of 500 PFs with low p(CS) matched our experimental data well in terms of shifting speeds as well as proportion of shifting PFs (Fig. 3f–h). By exploring the parameter space, we found that a familiarity-dependent decrease in p(CS) was sufficient to explain the lower amount of backward shifting in familiar environments (Fig. 3g,h). Indeed, systematically varying p(CS) revealed that it directly controls the proportion of significantly shifting PFs but has little impact on the shifting speeds (Fig. 3h), which is exactly the effect of familiarity in the experimental dataset (Fig. 1). Testing different amplitudes for the BTSP rule, to control for edge effects in the effective maximum weight change (Supplementary Fig. 15h), did not alter our results (Fig. 3h). Finally, using a different model of BTSP, adapted from the homosynaptic bidirectional rule developed in ref. 23, confirmed our conclusions (Supplementary Fig. 16): (1) BTSP of spatially modulated excitatory inputs can cause CA1-like shifting dynamics and (2) changes in the probability of BTSP-triggering events explain novelty/familiarity differences.

https://doi.org/10.1038/s41593-025-01894-6

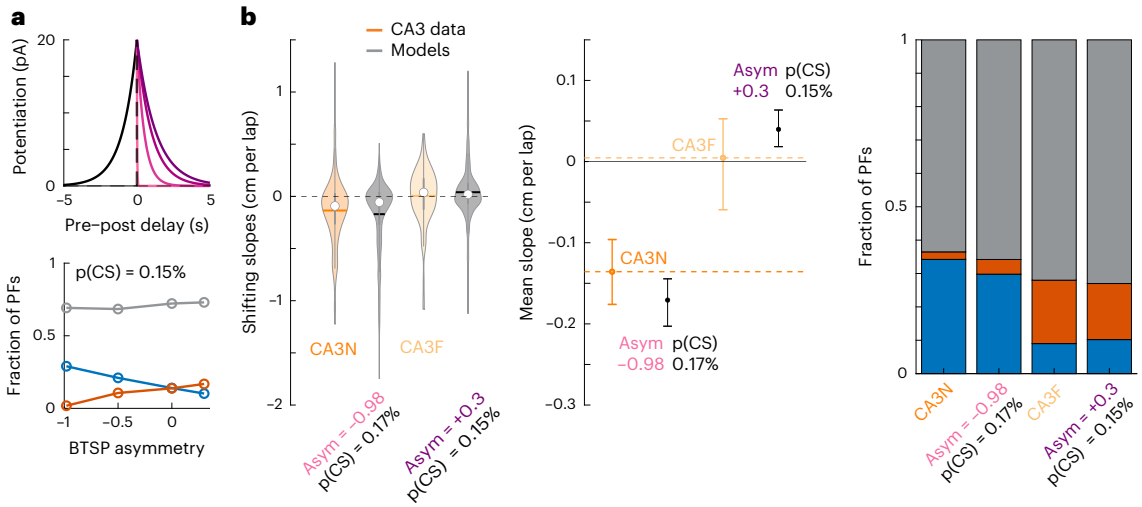

Fig. 4 | A dynamic BTSP rule supports PF shifting in CA3 in new and familiar environments. a, Top, BTSP rules. $\tau_{prepost}$ was set at 1 s, $\tau_{postpre}$ was varied from 20 ms (lighter shade) to 1.3 s (darker shade). Bottom, effect of BTSP rule asymmetry ($\tau_{postpre} - \tau_{prepost}$) on the proportions of backward (blue), forward (red) and nonsignificantly shifting PFs (gray), when p(CS) is held constant (0.15%). A total of 500 simulated PFs per condition. **b**, Comparison of the CA3 data (dark and light orange, same as in Fig. 1) with two versions of the BTSP model ($n = 500$ simulated PFs each). CA3N-like model parameters—p(CS) = 0.17%, $\tau_{postpre}$ = 20 ms. CA3F-like model parameters—p(CS) = 0.15%, $\tau_{postpre}$ = 1.3 s. Left, violin plots of the shifting speed distributions (median is open circle, mean is solid line and quartiles are gray whiskers). Middle, bootstrapped means and 95% CI. Right, proportions of backward (blue), forward (red) and nonsignificantly shifting PFs.

Does BTSP also support PF shifting in CA3? A p(CS) lower than in CA1 could explain the smaller proportion of shifting PFs (Fig. 1b–d). However, forward shifting proportions are also different from CA1, and Fig. 3h shows that p(CS) or BTSP amplitude does not affect that proportion by much. As a result, the BTSP rule measured in ref. 30 in CA1 could not fit our CA3 data well. We therefore hypothesized that a BTSP rule with different time constants could be at play in CA3. Notably, we discovered that the extent of asymmetry of the BTSP rule strongly determines the ratio of backward/forward shifting PFs (Fig. 4a). Because this ratio changes dramatically from familiar to new environments in the experimental data (Fig. 1b and Supplementary Fig. 1), it suggests that the symmetry in the BTSP rule may be dynamic in CA3 (Fig. 4b)—in a familiar environment, the predicted BTSP rule must be close to symmetric, which is consistent with recent findings from in vivo patch–clamp experiments[38], whereas the very high ratio of backward/forward shifting observed during a new experience is best explained by a highly asymmetric rule. Our simulations thus show that a BTSP rule different from CA1 could support PF shifting dynamics in CA3, with a familiarity-dependent change in its time constants, and lower p(CS) than in CA1.

Nonlinear PF trajectories reveal dynamic probability of BTSP-triggering events

If CS-triggered BTSP is the mechanism underlying PF shifting in the hippocampus, COM trajectories in experimental data should frequently look nonlinear as they do in our simulations (Fig. 3e–g). However, experimental reports have mostly focused on linear trajectories. We thus asked whether we could detect different types of COM trajectories in our experimental dataset (Figs. 5 and 6). First, we used an unsupervised approach, performing principal component analysis (PCA) on the ensemble of COM trajectories from our CA1 and CA3 recordings (Fig. 5a,b). This dimensionality reduction analysis revealed one main component explaining 77% of the variance in COM trajectories (Fig. 5b and Supplementary Fig. 17). This template trajectory was nonlinear with a large shift occurring through the first few laps. Further analysis, including all principal components, did not reveal meaningful clusters, suggesting that hippocampal PF shifting dynamics, regardless of familiarity levels, are best described as a continuum of a single type of nonlinear plateauing trajectory but with different amplitudes and polarities (Fig. 5c,d and Supplementary Fig. 17b). Although different conditions did not define separate clusters, as confirmed by a separate nonlinear dimensionality reduction method (Fig. 5e), there were differences in the distribution of absolute PC1 score, that is, shift amplitudes (Fig. 5c).

To verify that individual PFs exhibited the type of trajectory identified by PCA, and to further characterize this phenomenon, we performed nonlinear regression and fitted a plateauing exponential to each COM trajectory (Fig. 6). This supervised approach shows that most PFs are better described by such a nonlinear trajectory than a continuous linear drift, for both backward and forward shifting PFs, allowing us to detect dynamic PFs previously considered not significantly shifting by the linear analysis (Fig. 6b–d). The distribution of amplitudes and time constants reveals three classes of trajectories as follows: shifting early, stable and linear-like (Supplementary Fig. 18), with a majority of PFs having an early shift (Fig. 6e). These shifts can be very abrupt, occurring on the first lap after PF emergence, but they can also develop more slowly over the course of several laps (Fig. 6d,e). Overall, the nonlinear trajectories are consistent with a BTSP mechanism triggered by occasional events. The prevalence of early shifts suggests that the probability of BTSP-triggering events, p(CS), is dynamic and that these events tend to occur soon after PF emergence. We checked for differences between conditions and subfields (Fig. 6f,g and Supplementary Fig. 19); shifting amplitudes were smaller in the familiar environment in CA1, but also in CA3 (this was not detected for linear shifts; Fig. 1b). Consistent with our analysis of linear shifts, familiarity also had an effect on the proportion of nonlinearly shifting PFs (Fig. 6g). However, there was no evidence for time-constant differences (Supplementary Fig. 19), which suggests that the dynamics of p(CS) are similar across regions and familiarity levels.

The plateauing shape of the main component of PF trajectories shows that p(CS) is the largest right after PF emergence. But do BTSP-driven shifts continue to happen later? The zigzagging trajectories of secondary PCA dimensions (Fig. 5b), for which individual PFs can have a high score (Supplementary Fig. 17), suggest they do. Although later shifts seem rare, as evidenced by the lower amount of variance explained by these components, we found several examples of sinuous or zigzagging PF trajectories in our experimental data (Fig. 7a) as predicted by our BTSP model (Fig. 3g). Quantification of

https://doi.org/10.1038/s41593-025-01894-6

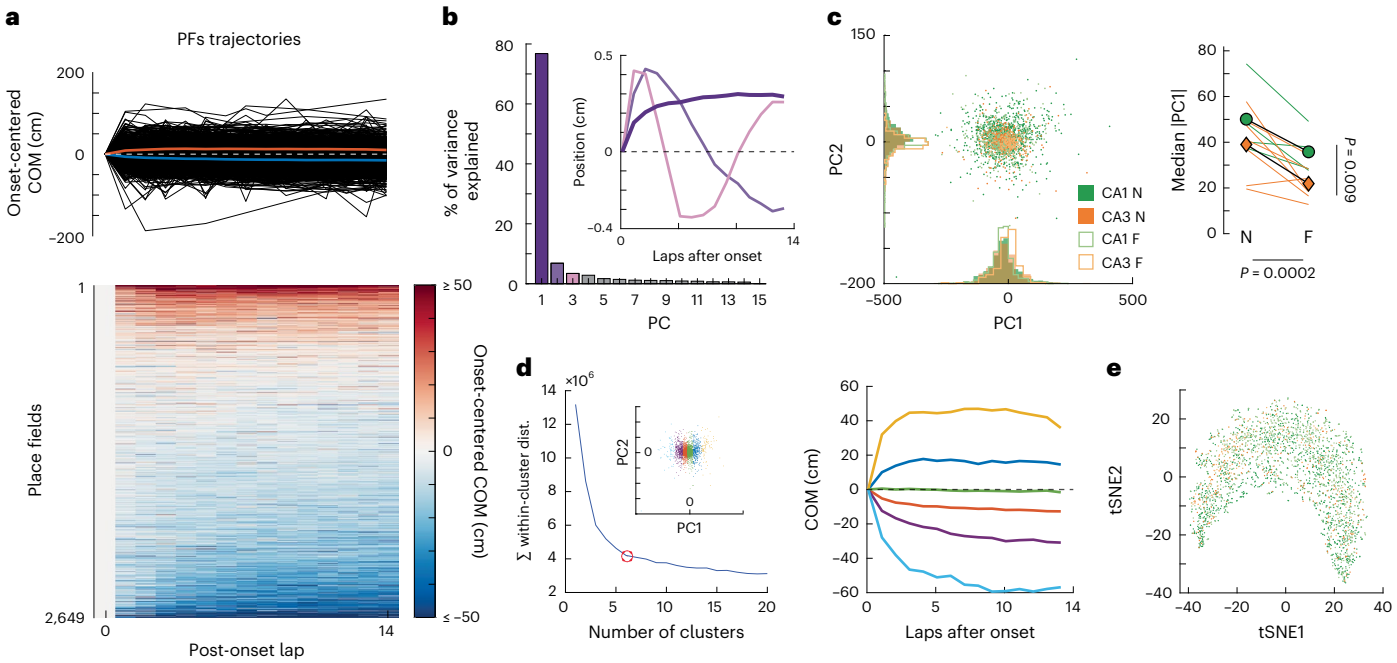

Fig. 5 | CA1 and CA3 PFs show a continuum of a single type of nonlinear trajectory in experimental data. a, COM trajectories for all PFs recorded in CA1 and CA3 (same data as in Fig. 1). Top, superimposed trajectories (black). Colored curves correspond to averages of PFs with negative (blue) or positive (red) average COM position. Bottom, same data in matrix form—each row is a PF trajectory. **b**, PCA was performed on the ensemble of trajectories shown in **a**. The first principal component PC1 explained 76.8% of the variance, revealing a nonlinear trajectory template with a large shift during the first few laps (inset, dark purple bold curve—note that the polarity of the trajectory is irrelevant here because projection scores can be positive or negative; Supplementary Fig. 17b). All other principal components revealed nonlinearities but explained little variance each. **c**, Left, scatterplot of the PC1 and PC2 projections of all recorded PFs, color-coded by subfield and familiarity. Right, animal-wise ANOVA (colored lines are individual mice and symbols are averages). There is a significant effect of both the subfield and familiarity on PC1 scores. Median absolute PC1 score ~1 + subfield + familiarity + (1 + familiarity | mice): subfield—$F(1,19) = 8.32$, $P = 0.0095$; familiarity—$F(1,19) = 20.33$, $P = 0.00024$; the interaction was excluded because not significant. **d**, Left, *k*-means clustering of all PFs trajectories using all principal components. Goodness-of-fit was optimal for six clusters (red dot = elbow), but clusters simply corresponded to segments of the PC1 scores (inset). Right, the color code is the same as in the left inset. Average COM trajectory for each *k*-means cluster reveals a continuum of the same PC1-like nonlinear trajectory. **e**, Nonlinear dimensionality reduction (tSNE) confirmed the PCA analysis—COM trajectories do not form separate clusters but are spread along a continuum, with CA1N, CA1F, CA3N and CA3F PFs distributed in a salt-and-pepper fashion (color code as in **c**).

lap-to-lap COM displacement shows that these examples of zigzagging trajectories are representative of a global phenomenon—large shifts are more likely on the first few laps but continue to occur with a constant, nonzero probability long after PF emergence (Fig. 7b,c and Supplementary Fig. 20). Using Einstein's theory of Brownian motion[39], we considered the PF COM as a moving particle in a one-dimensional space (Methods); individual particles can have heterogeneous trajectories, but the average square of these trajectories (mean squared displacement, MSD) will be linear if it follows a random walk. Diffusion analysis of our experimental data shows that the average PF trajectory is made of frequent individual nonlinear jumps on the first few laps, but it rapidly relaxes to a linear diffusion process (Fig. 7c and Supplementary Fig. 20f). Simulations without synaptic plasticity show that such a random walk is not the result of stochastic firing, but adding BTSP explains the phenomenon—the constant diffusion of the COM during later laps thus corresponds to a constant p(CS).

CA1/CA3 and novelty/familiarity differences in the diffusion coefficient (that is, the speed of the random walk) can be explained by differences in p(CS) (Figs. 3 and 4). However, the largest differences are in the amplitude of early shifts (laps 1–3 in Fig. 7c). Our initial BTSP model is not able to produce such large early shifts (Fig. 7c) because CSs necessarily occur in-field. We thus designed a more complex model where CSs are more likely in-field but may occur out-of-field, and where p(CS) exponentially decays from lap to lap (Fig. 7d(i)). This model best captures the dynamics of PF shifting observed in CA1, both in familiar and new environments (Fig. 7d(ii) and Supplementary Fig. 21).

Discussion

Our main results (Fig. 8) have fundamental implications for theories of learning and memory, not only because we show that, in contrast to classic Hebbian STDP, BTSP can support the shifting dynamics of hippocampal representations, but also by revealing (1) how the patterned dynamics of BTSP-triggering events explain the heterogeneity of PF trajectories, (2) how the BTSP rule and the frequency of its induction differ between CA1 and CA3 and change between new and familiar environments and (3) how CA3 inputs partially control the probability of BTSP induction in CA1.

Our modeling suggests that classic Hebbian STDP cannot explain the shifting trajectories observed in PFs recorded in the hippocampus. This conclusion contrasts with that of seminal studies[15,25,34]. We showed that this discrepancy comes from the fact that (1) previous models used high firing rates, which enhances the effect of STDP by increasing the number of prepost spike pairs, and (2) we had access to a much larger sample of recordings to compare to. Using a range of realistic and unrealistic firing rates, we found that STDP is always too weak to induce, in a simple place cell model, the large shifting speeds that can occur in real PFs.

Our model, like past ones, did not consider some complexities of real place cells. For instance, neurons of the hippocampal formation tend to fire at different phases of the theta rhythm, with CA3 inputs repeatedly firing before superficial CA1 place cells[40], which would amplify the potentiating effects of STDP and increase backward shifts. Similarly, phase precession in the CA3 inputs was shown to increase shifting speeds up to what we experimentally measured[34], although

https://doi.org/10.1038/s41593-025-01894-6

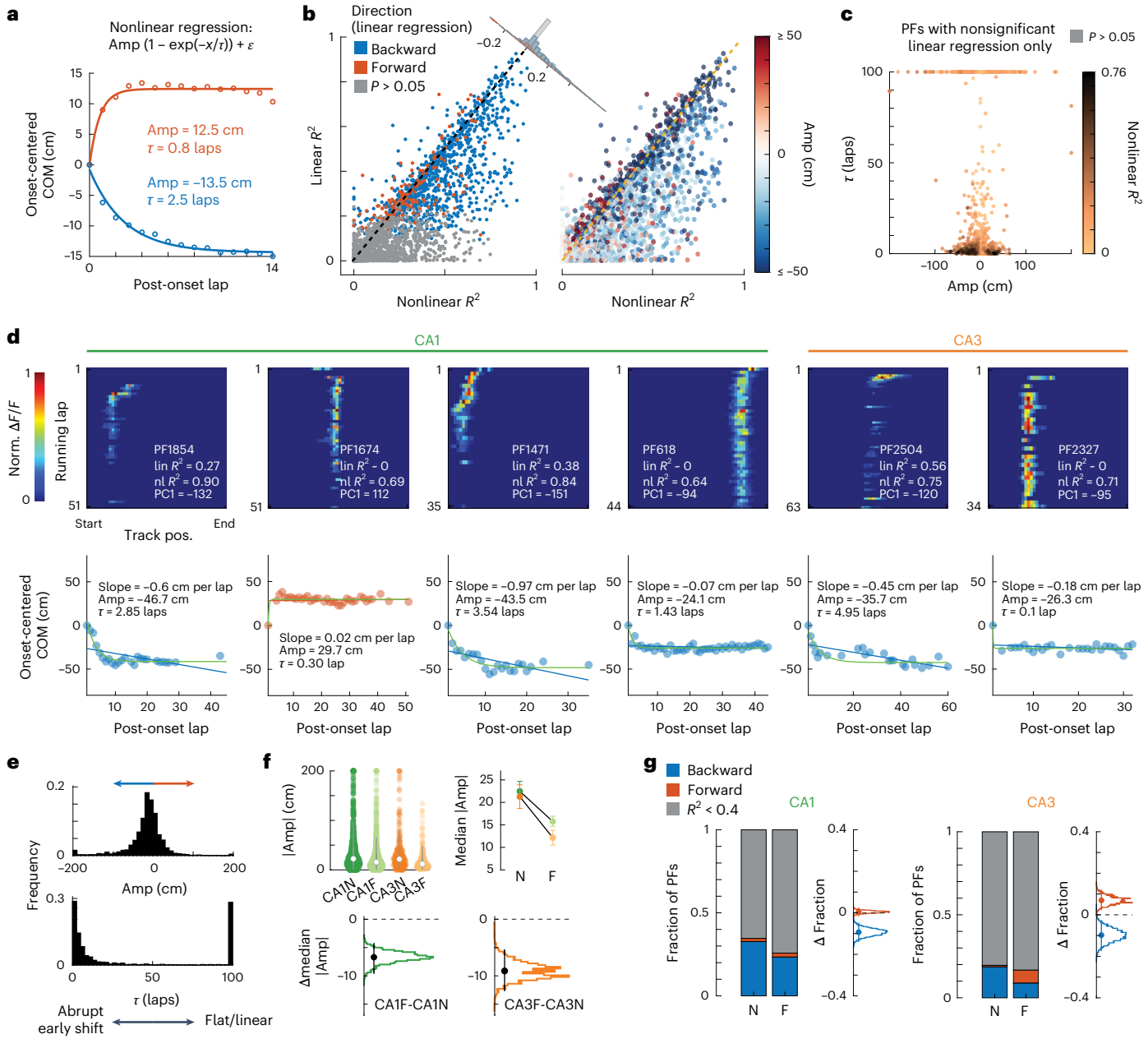

Fig. 6 | Single PF trajectories consistently show nonlinear shifts early after PF emergence. a, Average trajectory (data points) of PFs with negative (blue) or positive (red) mean COM position (as in Fig. 5a) fitted by a plateauing exponential similar to PC1 in Fig. 5b. **b**, Comparison of the goodness-of-fit (R^2) between this nonlinear regression and linear regression (as in Fig. 1) for all 2,649 PFs. The nonlinear regression fits most individual PF trajectories as well or better (data points under the identity dashed line). The difference of fit (corner histogram) is skewed towards positive values (Wilcoxon signed-rank test $-z = 27.5$, $P < 0.0001$), showing PFs are better described by a plateauing exponential. **c**, Many PFs that were categorized as nonsignificantly shifting with linear regression are well fitted (dark dots) by a plateauing exponential with an abrupt shift (small τ), going backward (Amp < 0) or forward (Amp > 0). **d**, Examples of PFs recorded in CA1 or CA3 with dynamics well described by a plateauing exponential. Top, lap-wise PF activity, with goodness-of-fit values (R^2) for the linear and nonlinear regressions, and the PC1 score for comparison. Bottom, linear and nonlinear regressions on the lap-wise COM (data points). Backward shift in blue and forward in red. Note that in some PFs, the shift occurs on lap 1 after onset (for example, PFs 618 and 2327), whereas in others, the shift is more gradual. **e**, Distribution of Amp and τ values for all PFs combined (Amp and τ covariance in Supplementary Fig. 13). **f**, Statistics on absolute Amp. Top left, violin scatter plots of |Amp| for all conditions. Open white circle is median and gray bars indicate quartiles. Top right, bootstrapped median and 95% CI for each condition. Bottom, bootstrapped difference between F and N. Black error bar, 95% CI of the mean. Shift amplitude decreases with familiarity in both CA1 and CA3. **g**, Proportions of nonlinearly shifting PFs ($R^2 \geq 0.4$). Bootstrapped exact test (error bars are 95% CI) shows that the fraction of backward PFs significantly decreases in the familiar environment both in CA1 and CA3. A significant increase in nonlinear forward PFs is only detected in CA3.

that effect would be attenuated if precession in CA1 is not fully inherited from CA3, and if lower, more realistic firing rates were used. Overall, improving the realism of the place cell model by accounting for phase preference and precession may at best amplify the linear backward shifting due to the asymmetry of the STDP rule. Yet, consistent with previous reports of heterogenous PF trajectories[16,17,20,41], we showed that not all PFs drift backward linearly—(1) forward shifting exists above chance level (Figs. 1 and 2) and (2) PFs generally follow a nonlinear trajectory with shifts more frequent on early laps (Figs. 5–7). In our simulations (Supplementary Figs. 5–10), STDP, even when strong enough,

https://doi.org/10.1038/s41593-025-01894-6

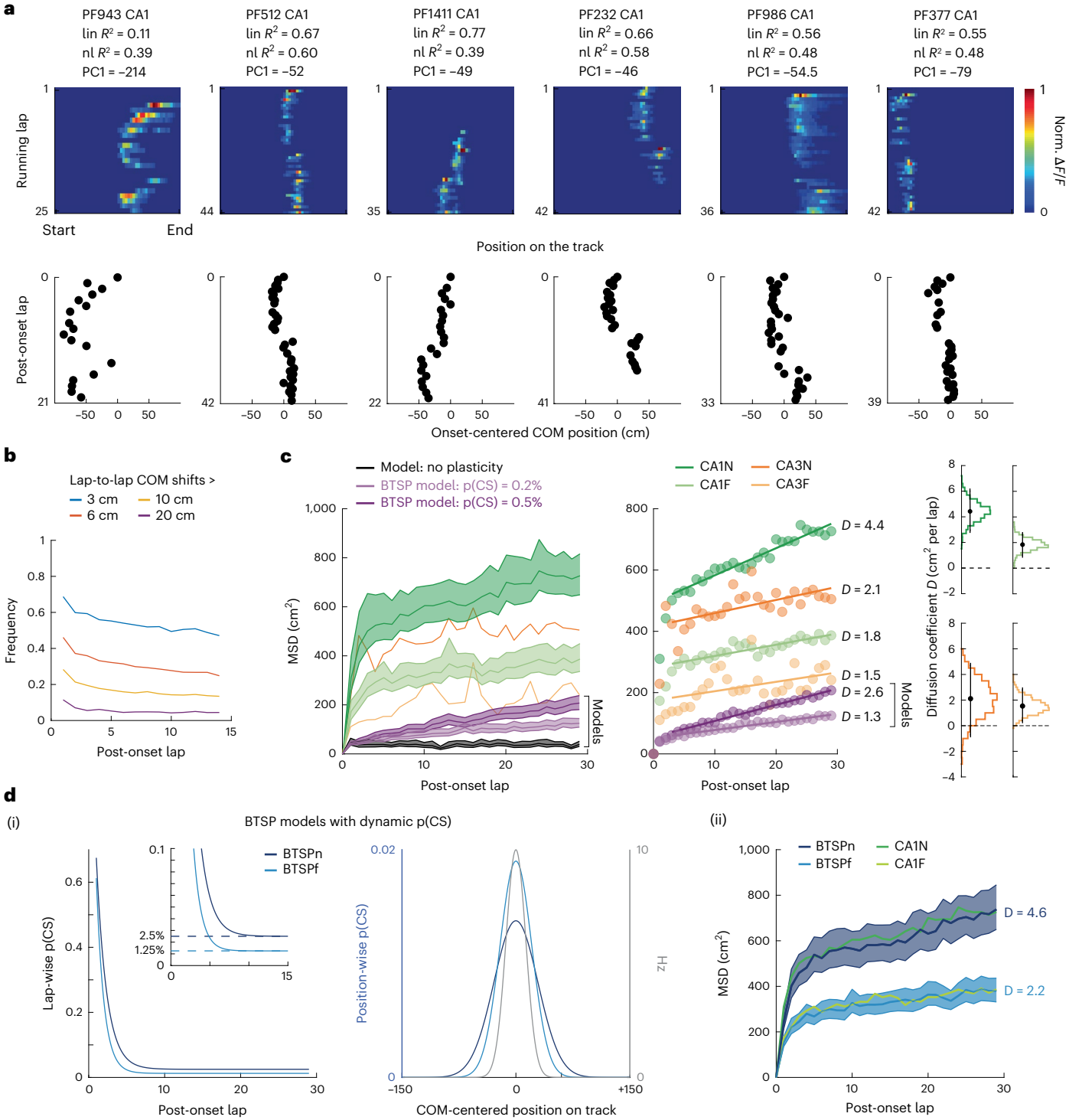

Fig. 7 | The probability of shift-triggering BTSP-induction decays to a constant after PF emergence. a, Example of PFs showing abrupt shifting late after PF emergence (bottom). CA1, PF1471 and CA3, PF2504 in Fig. 6d are other examples with zigzag trajectories. **b**, Frequency of occurrence (fraction of PFs per lap) of lap-to-lap shifts > 3, 6, 10 or 20 cm (n = 2,649 PFs, all conditions pooled). **c**, Diffusion analysis on PFs defined over at least 30 laps. Mean squared displacement (MSD) of the COM as a function of post-onset laps (n = 942 for CA1N, 880 for CA1F, 222 for CA3N, 100 for CA3F and 500 for each model. BTSP simulations are taken from Fig. 3). For a one-dimensional random walk, MSD = 2 × D × laps (D, diffusion coefficient). Left, MSD with 95% bootstrapped CI. CA3 CIs were omitted for readability. Middle, same data as in left. Regression lines from laps 4–30 show that PF shifting after lap 3 is well explained by a constant D, that is, a random walk (Supplementary Fig. 20f). CA1N–R^2 = 94.2%, P < 0.0001; CA1F–R^2 = 80.1%, P < 0.0001; CA3N–R^2 = 43.1%, P = 0.0002; CA3F–R^2 = 20.1%, P = 0.019; BTSP model p(CS) = 0.005–R^2 = 98.3%, P < 0.0001; BTSP model p(CS) = 0.002–R^2 = 94.5%, P < 0.0001 (P values from F test). Right, bootstrapped exact tests that D, estimated by linear regression, is positive (error bars, 95% CI of the mean). CA1N/F, P = 0; CA3N, P = 0.072 and CA3F, P = 0.002. **d**, BTSP models with dynamic p(CS) explain CA1 shifting dynamics. (i), Models of p(CS) fitted to CA1N and CA1F data. Left, the probability of a CS occurring on a given lap follows an exponential decay with positive asymptote. Right, if a CS occurs, its location is randomly selected from a Gaussian distribution (blue curves) centered on the current COM of the synaptic weights. CSs can occur out-of-field when Gaussians are larger than the PF (gray—typical PF with PF s.d. = 13 cm). (ii), MSD resulting from BTSPn and BTSPf models described in (i) (500 simulated PFs each). CA1 data in green for comparison (same as in **c**).

https://doi.org/10.1038/s41593-025-01894-6

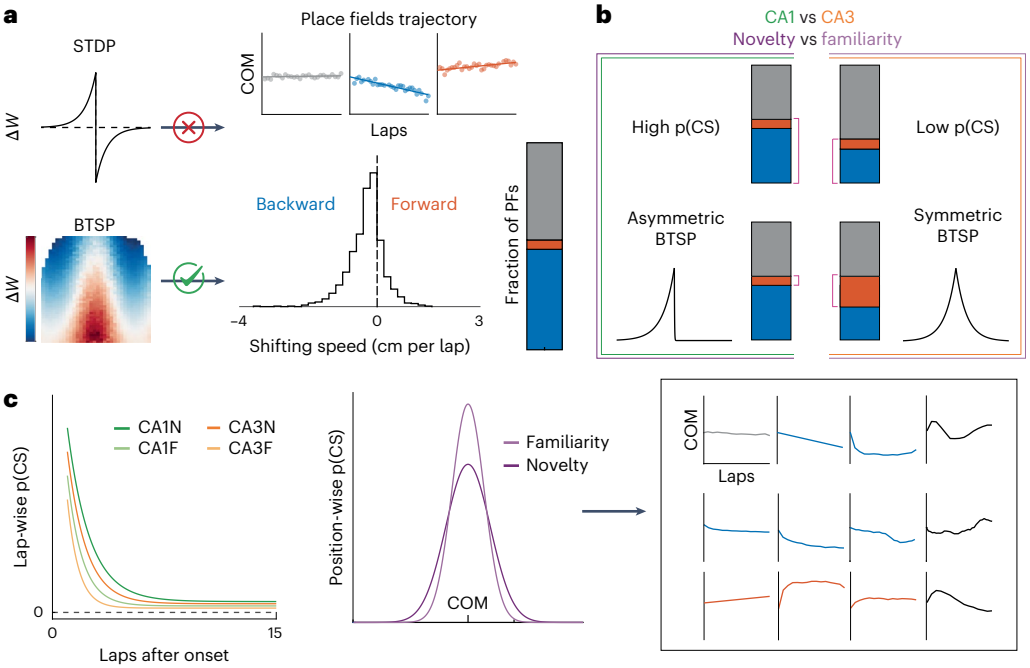

Fig. 8 | Graphical summary. a, BTSP (but not STDP) of spatial inputs on pyramidal cells explains PF shifting in CA1 and CA3. **b**, The probability of BTSP-triggering events, p(CS), controls the fraction of shifting PFs (top). The shape of the BTSP rule controls the ratio of forward versus backward shifting (bottom). **c**, A dynamic p(CS) with plateauing decay combined with occasional out-of-field BTSP induction explains the diversity of PF trajectories.

never explained the diversity of hippocampal PF trajectories and never showed nonlinear shifts. Sharp wave ripples[42], occurring during pauses in or between laps and associated with brief bouts of high firing rates that may temporarily amplify STDP effects, could potentially induce forward or nonlinear PF shifts[43]. However, ripples are population events that would result in synchronous shifts across many PFs, which were never detected in the population average[12,17], and seem inconsistent with the PF-centered dynamics that we uncovered (Figs. 5–7).

Could an improved model of classic synaptic plasticity, accounting for STDP but also for rate and heterosynaptic effects[44], better explain hippocampal PF shifting dynamics? Our work (Supplementary Fig. 11) as well as previous studies[34,45] suggest that it is not sufficient to yield large enough PF shifts. In particular, a biophysically realistic calcium-dependent rule combined with metaplasticity led only to backward trajectories with small amplitudes (~0.2 cm per lap) and a plateauing decay much slower than what we observed[45]. However, all models above only considered homogeneous excitatory inputs to pyramidal cells; the effect of interactions between multiple types of plastic synapses on PF shifting remains to be tested.

Nevertheless, we show that non-Hebbian BTSP at excitatory–pyramidal synapses is a clear and simple mechanism explaining hippocampal PF shifting because it causes large synaptic weight changes and is triggered by rare dendritic events (associated with CSs) that can induce a diversity of trajectories, both backward and forward, linear and nonlinear, depending on where on the track the CSs occur (Fig. 3). In our model, the probability of BTSP-triggering events controls the proportion of significantly shifting PFs, and the asymmetry of the BTSP rule determines the ratio of backward versus forward shifting PFs (Fig. 8b). Surprisingly, varying the amplitude of BTSP did not strongly affect the magnitude of shifts (Fig. 3j), at least not in the range that we investigated, but this is due to the dampening effects of the simple homeostatic rule that we used (Methods). In theory, the magnitude of shifts should depend on the following three factors: the location of BTSP-triggering events, the amplitude of BTSP and its time constants (the larger the time constant, the more inputs are potentiated).

BTSP is a recent discovery and its phenomenology and mechanisms are not fully worked out. The original finding suggested a purely potentiating rule[30], which would lead to runaway potentiation. Even with bounded synaptic weights, this rule would eventually saturate all synapses, in contrast to what recent experiments showed—two successive BTSP-triggering events potentiated inputs near the second CS location but depressed activity at other locations[23]. Recent work has suggested that a weight-dependent bidirectional homosynaptic rule could explain the phenomenon[23,37], but these models did not consider alternatives involving interactions between the original BTSP potentiating rule and fast heterosynaptic effects known to prevent runaway synaptic dynamics[3,46]. Heterosynaptic competition and cooperativity are prevalent in the hippocampus[47,48] and can modulate BTSP[49]. To model BTSP, we thus chose to combine the original BTSP rule with synaptic normalization, a simple heterosynaptic rule mediating homeostasis. The simplicity of that strategy allowed us to implement BTSP in a spiking network, optimize a single set of parameters to match the most recent experimental data (Supplementary Fig. 14) and was important to directly compare with our results on STDP. Our model has potential limitations (Methods), but our results hold when using a homosynaptic bidirectional rule (Supplementary Fig. 16). Our work thus offers an alternative to the homosynaptic model, but future experimental and modeling work is needed to select between the two, including implementation of more realistic heterosynaptic and homosynaptic processes[3,50–52].

Regardless of its homosynaptic or heterosynaptic nature, our study provides essential insights into the phenomenology and role of BTSP.

First, our simulations of BTSP induction experiments precisely quantified the amplitude of synaptic weight changes (Supplementary Figs. 12–14)—the maximum weight change due to an input spike–CS pairing was ~4 pA in single input in vitro stimulations[30] and 6–8 pA in PF translocation experiments[23], that is, 8–16 times higher than for STDP (~0.5 pA).

Second, our modeling of spontaneous PF dynamics during exploration, in combination with our characterization of PF trajectories in vivo,

provides crucial information on when and how often BTSP-triggering events occur. We found that these events are most likely at or right after PF onset, often leading to abrupt early shifts (Figs. 5–7). We extended previous in vivo research that reported CSs in CA1 neurons with an already established PF[23,31–33] by providing evidence that BTSP-triggering events do happen long after PF formation, with a dynamic probability that relaxes a few laps after PF emergence to a positive constant (Figs. 7 and 8c). We also showed that CSs must occasionally occur outside the PF to explain the large early shifts (Fig. 7b,c).

Direct measures of the frequency of CSs are inconsistent across past studies, likely due to low sample sizes (7–30 cells). Ref. 32 reported an average of 1.8 CSs per 100 spikes in a familiar environment, with higher p(CS) during the peak of θ-oscillations, whereas ref. 33 reported much lower frequencies. The study in ref. 31, using voltage imaging rather than patch–clamp, detected many CSs of short duration. Our analysis, based on hundreds of PFs, points to a high probability of BTSP-triggering events at PF onset (Fig. 7c), but a very low average probability (~0.2 per 100 spikes in a familiar environment, which is an upper bound, given that some shifting may be inherited from dynamic CA3 inputs). Our results thus suggest that not all experimentally recorded CSs necessarily trigger BTSP, or not to the same degree, perhaps depending on the duration of the dendritic plateau potential[53] or the number of involved dendrites. Our finding that the probability of BTSP-triggering event decays after PF emergence could thus be due to shorter CSs in established place cells[31,32].

Furthermore, our optogenetic silencing of CA3 inputs to CA1 showed that the proportion of shifting PFs in CA1 depends on CA3 (Fig. 1d(i)–(iii)). Because our modeling showed that CA1 shifting is not directly inherited from shifting CA3 PFs (Fig. 2e), and that the proportion of shifting PFs reflects p(CS) (Fig. 3), together, our results suggest that CA3 inputs control, at least in part, the probability of BTSP-triggering events. This is consistent with the idea that CSs are triggered by the coincidence of CA3 and entorhinal cortex inputs[5].

Finally, our study suggests that BTSP is not restricted to CA1, where it was discovered, but also occurs in CA3 in vivo, albeit with phenomenological differences (Fig. 4). Dendritic calcium plateaus and associated CSs are indeed not specific to CA1; they have been recorded in cortical[54] and CA3 pyramidal cells[55], but their role in plasticity and their frequency were not known. Our study suggests that they can trigger BTSP in CA3, inducing PF shifting, and that their probability follows similar dynamics to CA1, decaying after PF emergence (Figs. 5–7). Unlike CA1 however, we found that (1) the lower proportion of shifting PFs demonstrates a lower probability of BTSP-triggering events, even in new environments, (2) the smaller shifts suggest that fewer events occur out-of-field (Figs. 7 and 8c) and (3) the BTSP rule must be close to symmetric to explain the equal proportion of forward and backward shifting in familiar environments. This third point is consistent with recent in vivo patch–clamp experiments that measured symmetric potentiation profiles following spontaneous and induced CSs[38]. Intriguingly, in new environments, CA3 PF shifting proportions are dramatically skewed backward, suggesting a highly asymmetric rule. This novelty-dependent change in the time constants of the BTSP kernel could reflect changes in the duration of the dendritic plateaus—CSs appear longer in CA3 than CA1 in familiar environments[38], but a CA3-specific short calcium spike[56] could be more prevalent in new contexts.

In conclusion, our study of PF shifting dynamics offers a unique perspective on the synaptic mechanisms at play during incidental learning and memory formation. We showed (Fig. 8) that (1) BTSP is the likeliest mechanism driving the dynamics of hippocampal representations during familiarization, (2) the average probability of BTSP-triggering events is higher during new experiences than familiar ones, especially in CA1 and (3) the shape of the BTSP rule changes with familiarity, especially in CA3. Novelty-dependent neuromodulatory and inhibitory signals[57–59] could mediate these changes by modulating both synaptic eligibility traces and the probability and duration of BTSP-triggering calcium plateaus[5,60].

Online content

Any methods, additional references, Nature Portfolio reporting summaries, source data, extended data, supplementary information, acknowledgements, peer review information; details of author contributions and competing interests; and statements of data and code availability are available at https://doi.org/10.1038/s41593-025-01894-6.

References

1. Dringenberg, H. C. The history of long-term potentiation as a memory mechanism: controversies, confirmation, and some lessons to remember. *Hippocampus* **30**, 987–1012 (2020).
2. Moldakarimov, S. & Sejnowski, T. J. Neural computation theories of learning. In *Learning and Memory: A Comprehensive Reference* 2nd edn, Vol. 1 (ed. Byrne, J. H.) 579–589 (Elsevier, 2017).
3. Chistiakova, M., Bannon, N. M., Chen, J.-Y., Bazhenov, M. & Volgushev, M. Homeostatic role of heterosynaptic plasticity: models and experiments. *Front. Comput. Neurosci.* **9**, 89 (2015).
4. Feldman, D. E. The spike-timing dependence of plasticity. *Neuron* **75**, 556–571 (2012).
5. Magee, J. C. & Grienberger, C. Synaptic plasticity forms and functions. *Annu. Rev. Neurosci.* **43**, 95–117 (2020).
6. Aljadeff, J., Gillett, M., Pereira Obilinovic, U. & Brunel, N. From synapse to network: models of information storage and retrieval in neural circuits. *Curr. Opin. Neurobiol.* **70**, 24–33 (2021).
7. Graupner, M., Wallisch, P. & Ostojic, S. Natural firing patterns imply low sensitivity of synaptic plasticity to spike timing compared with firing rate. *J. Neurosci.* **36**, 11238–11258 (2016).
8. Lim, S. et al. Inferring learning rules from distributions of firing rates in cortical neurons. *Nat. Neurosci.* **18**, 1804–1810 (2015).
9. Morris, R. Theories of hippocampal function. In *The Hippocampus Book* (eds Andersen, P. et al.) 581–714 (Oxford University Press, 2006).
10. Bliss, T. V. P., Collingridge, G. L., Morris, R. G. M. & Reymann, K. G. Long-term potentiation in the hippocampus: discovery, mechanisms and function. *Neuroforum* **24**, A103–A120 (2018).
11. Buchanan, K. A. & Mellor, J. R. The activity requirements for spike timing-dependent plasticity in the hippocampus. *Front. Synaptic Neurosci.* **2**, 11 (2010).
12. Dong, C., Madar, A. D. & Sheffield, M. E. J. Distinct place cell dynamics in CA1 and CA3 encode experience in new environments. *Nat. Commun.* **12**, 2977 (2021).
13. Lee, I., Rao, G. & Knierim, J. J. A double dissociation between hippocampal subfields: differential time course of CA3 and CA1 place cells for processing changed environments. *Neuron* **42**, 803–815 (2004).
14. Mehta, M. R., Barnes, C. A. & McNaughton, B. L. Experience-dependent, asymmetric expansion of hippocampal place fields. *Proc. Natl Acad. Sci. USA* **94**, 8918–8921 (1997).
15. Mehta, M. R., Quirk, M. C. & Wilson, M. A. Experience-dependent asymmetric shape of hippocampal receptive fields. *Neuron* **25**, 707–715 (2000).
16. Priestley, J. B., Bowler, J. C., Rolotti, S. V., Fusi, S. & Losonczy, A. Signatures of rapid plasticity in hippocampal CA1 representations during novel experiences. *Neuron* **110**, 1978–1992 (2022).
17. Roth, E. D., Yu, X., Rao, G. & Knierim, J. J. Functional differences in the backward shifts of CA1 and CA3 place fields in novel and familiar environments. *PLoS ONE* **7**, e36035 (2012).
18. Burke, S. N., Maurer, A. P., Yang, Z., Navratilova, Z. & Barnes, C. A. Glutamate receptor-mediated restoration of experience-dependent place field expansion plasticity in aged rats. *Behav. Neurosci.* **122**, 535–548 (2008).

19. Ekstrom, A. D., Meltzer, J., McNaughton, B. L. & Barnes, C. A. NMDA receptor antagonism blocks experience-dependent expansion of hippocampal 'place fields'. *Neuron* **31**, 631–638 (2001).
20. Kaganovsky, K. et al. Dissociating encoding of memory and salience by manipulating long-term synaptic potentiation. Preprint at *bioRxiv* https://doi.org/10.1101/2022.01.04.474865 (2022).
21. Masset, P., Qin, S. & Zavatone-Veth, J. A. Drifting neuronal representations: bug or feature? *Biol. Cybern.* **116**, 253–266 (2022).
22. Mau, W., Hasselmo, M. E. & Cai, D. J. The brain in motion: how ensemble fluidity drives memory-updating and flexibility. *eLife* **9**, e63550 (2020).
23. Milstein, A. D. et al. Bidirectional synaptic plasticity rapidly modifies hippocampal representations. *eLife* **10**, e73046 (2021).
24. Bi, G. & Poo, M. Synaptic modification by correlated activity: Hebb's postulate revisited. *Annu. Rev. Neurosci.* **24**, 139–166 (2001).
25. Yu, X., Knierim, J. J., Lee, I. & Shouval, H. Z. Simulating place field dynamics using spike timing-dependent plasticity. *Neurocomputing* **69**, 1253–1259 (2006).
26. Inglebert, Y., Aljadeff, J., Brunel, N. & Debanne, D. Synaptic plasticity rules with physiological calcium levels. *Proc. Natl Acad. Sci. USA* **117**, 33639–33648 (2020).
27. Wittenberg, G. M. & Wang, S. S.-H. Malleability of spike-timing-dependent plasticity at the CA3–CA1 synapse. *J. Neurosci.* **26**, 6610–6617 (2006).
28. Lisman, J. & Spruston, N. Questions about STDP as a general model of synaptic plasticity. *Front. Synaptic Neurosci.* **2**, 140 (2010).
29. Gallistel, C. R. & Matzel, L. D. The neuroscience of learning: beyond the Hebbian synapse. *Annu. Rev. Psychol.* **64**, 169–200 (2013).
30. Bittner, K. C., Milstein, A. D., Grienberger, C., Romani, S. & Magee, J. C. Behavioral time scale synaptic plasticity underlies CA1 place fields. *Science* **357**, 1033–1036 (2017).
31. Fan, L. Z. et al. All-optical physiology resolves a synaptic basis for behavioral timescale plasticity. *Cell* **186**, 543–559 (2023).
32. Bittner, K. C. et al. Conjunctive input processing drives feature selectivity in hippocampal CA1 neurons. *Nat. Neurosci.* **18**, 1133–1142 (2015).
33. Cohen, J. D., Bolstad, M. & Lee, A. K. Experience-dependent shaping of hippocampal CA1 intracellular activity in novel and familiar environments. *eLife* **6**, e23040 (2017).
34. D'Albis, T., Jaramillo, J., Sprekeler, H. & Kempter, R. Inheritance of hippocampal place fields through Hebbian learning: effects of theta modulation and phase precession on structure formation. *Neural Comput.* **27**, 1624–1672 (2015).
35. Pfister, J.-P. & Gerstner, W. Triplets of spikes in a model of spike timing-dependent plasticity. *J. Neurosci.* **26**, 9673–9682 (2006).
36. Wang, H.-X., Gerkin, R. C., Nauen, D. W. & Bi, G.-Q. Coactivation and timing-dependent integration of synaptic potentiation and depression. *Nat. Neurosci.* **8**, 187–193 (2005).
37. Cone, I. & Shouval, H. Z. Behavioral time scale plasticity of place fields: mathematical analysis. *Front. Comput. Neurosci.* **15**, 640235 (2021).
38. Li, Y., Briguglio, J. J., Romani, S. & Magee, J. C. Mechanisms of memory-supporting neuronal dynamics in hippocampal area CA3. *Cell* **187**, 6804–6819 (2024).
39. Einstein, A. B. On the motion of small particles suspended in liquids at rest required by the molecular-kinetic theory of heat. *Ann. Phys.* **322**, 549–560 (1905).
40. Valero, M. & de la Prida, L. M. The hippocampus in depth: a sublayer-specific perspective of entorhinal–hippocampal function. *Curr. Opin. Neurobiol.* **52**, 107–114 (2018).
41. Lee, I. & Knierim, J. J. The relationship between the field-shifting phenomenon and representational coherence of place cells in CA1 and CA3 in a cue-altered environment. *Learn. Mem.* **14**, 807–815 (2007).
42. Buzsáki, G. Hippocampal sharp wave-ripple: a cognitive biomarker for episodic memory and planning. *Hippocampus* **25**, 1073–1188 (2015).
43. Ponzi, A. Forward shift from reverse replay. *Cogn. Neurodyn.* **3**, 39–46 (2009).
44. Shouval, H., Wang, S. & Wittenberg, G. M. Spike timing dependent plasticity: a consequence of more fundamental learning rules. *Front. Comput. Neurosci.* **4**, 19 (2010).
45. Yu, X., Shouval, H. Z. & Knierim, J. J. A biophysical model of synaptic plasticity and metaplasticity can account for the dynamics of the backward shift of hippocampal place fields. *J. Neurophysiol.* **100**, 983–992 (2008).
46. Zenke, F. & Gerstner, W. Hebbian plasticity requires compensatory processes on multiple timescales. *Philos. Trans. R. Soc. B Biol. Sci.* **372**, 20160259 (2017).
47. Chater, T. E. & Goda, Y. My neighbour hetero—deconstructing the mechanisms underlying heterosynaptic plasticity. *Curr. Opin. Neurobiol.* **67**, 106–114 (2021).
48. Magó, Á., Weber, J. P., Ujfalussy, B. B. & Makara, J. K. Synaptic plasticity depends on the fine-scale input pattern in thin dendrites of CA1 pyramidal neurons. *J. Neurosci.* **40**, 2593–2605 (2020).
49. O'Dell, T. J. Behavioral timescale cooperativity and competitive synaptic interactions regulate the induction of complex spike burst-dependent long-term potentiation. *J. Neurosci.* **42**, 2647–2661 (2022).
50. Ebner, C., Clopath, C., Jedlicka, P. & Cuntz, H. Unifying long-term plasticity rules for excitatory synapses by modeling dendrites of cortical pyramidal neurons. *Cell Rep.* **29**, 4295–4307 (2019).
51. Moldwin, T., Kalmenson, M. & Segev, I. Asymmetric voltage attenuation in dendrites can enable hierarchical heterosynaptic plasticity. *eNeuro* **10**, ENEURO.0014-23.2023 (2023).
52. Triesch, J., Vo, A. D. & Hafner, A.-S. Competition for synaptic building blocks shapes synaptic plasticity. *eLife* **7**, e37836 (2018).
53. Takahashi, H. & Magee, J. C. Pathway interactions and synaptic plasticity in the dendritic tuft regions of CA1 pyramidal neurons. *Neuron* **62**, 102–111 (2009).
54. Xu, N. et al. Nonlinear dendritic integration of sensory and motor input during an active sensing task. *Nature* **492**, 247–251 (2012).
55. Balind, S. R. et al. Diverse synaptic and dendritic mechanisms of complex spike burst generation in hippocampal CA3 pyramidal cells. *Nat. Commun.* **10**, 1859 (2019).
56. Magó, Á., Kis, N., Lükő, B. & Makara, J. K. Distinct dendritic Ca^{2+} spike forms produce opposing input-output transformations in rat CA3 pyramidal cells. *eLife* **10**, e74493 (2021).
57. Heer, C. M. & Sheffield, M. E. J. Distinct catecholaminergic pathways projecting to hippocampal CA1 transmit contrasting signals during behavior and learning. *eLife* **13**, RP95213 (2024).
58. Pedrosa, V. & Clopath, C. The interplay between somatic and dendritic inhibition promotes the emergence and stabilization of place fields. *PLoS Comput. Biol.* **16**, e1007955 (2020).
59. Sheffield, M. E. J., Adoff, M. D. & Dombeck, D. A. Increased prevalence of calcium transients across the dendritic arbor during place field formation. *Neuron* **96**, 490–504 (2017).
60. Fuchsberger, T. et al. Postsynaptic burst reactivation of hippocampal neurons enables associative plasticity of temporally discontiguous inputs. *eLife* **11**, e81071 (2022).
61. Mou, X., Cheng, J., Yu, Y. S. W., Kee, S. E. & Ji, D. Comparing mouse and rat hippocampal place cell activities and firing sequences in the same environments. *Front. Cell. Neurosci.* **12**, 332 (2018).

Methods

All experimental procedures were in accordance with the University of Chicago Animal Care and Use Committee guidelines.

Experimental recordings of CA1 or CA3

Most experimental data analyzed in this study were previously published in ref. 12. Briefly, GCaMP6f was first expressed in CA1 or CA3 principal neurons of the dorsal hippocampus of 10- to 12-week-old male mice. AAV1-CamkII-GCaMP6f was injected in the CA1 subfield of C57Bl6 mice, whereas, to specifically target CA3 and exclude other hippocampal subfields, a CRE-dependent version of the same genetically encoded calcium indicator was injected in C57BL/6-Tg(Grik4-cre)G32-4Stl/J mice (CA1 coordinates −1.7 mm lateral and −2.3 caudal from Bregma, 1.25 mm below dura; CA3 coordinates −2 mm lateral and −1.7 mm caudal of Bregma, 1.9 mm below dura). To record the activity of large populations of neurons, mice were head-fixed under the objective of a two-photon microscope. Field-of-view positions along the transverse axis were centered on intermediate CA1 (CA1b) and proximal CA3 (CA3a) (Supplementary Fig. 1d).

Mouse behavior consisted of running on a Styrofoam wheel to move through a virtual environment using ViRMEn (https://github.com/Tank-Lab/ViRMEn) and displayed on surrounding screens. Mouse behavior including speed, position and licking was collected using the PicoScope Oscilloscope (Pico Technology, PICO4824). Mice could only go forward or backward on a 300 cm virtual linear track and were trained through positive reinforcement to run forward multiple laps. Water was provided as a reward at the end of each lap, at which point the display was paused for 1.5 s before the animal was 'teleported' back to the start of the track to start a new lap. Five days after window implantation surgery, mice were trained for 10–14 days in a virtual environment defined as the familiar context (F) until they reached a consistent speed criterion of at least 10 cm s^{-1} (that is, more than 2 laps per min). Engagement with the virtual environment was evident from the preemptive licking and the slowing down shown by animals before they reached the reward zone at the end of a lap[12,62].

Imaging was performed on the following days: on day 1, mice were exposed to the familiar environment and allowed to run at least 20 laps, followed by exposure to a new environment (N1), with another 300 cm track in which they were allowed to run in at least 35 laps. A similar procedure was followed on day 2, during which a new field of view was recorded, with mice navigating again the familiar environment and then switched to a second new environment (N2). In the present study, all PFs detected on days 1 and 2 were combined and labeled either F or N. Calcium imaging was done with a laser-scanning two-photon microscope (Neurolabware) with a femtosecond-pulsed two-photon laser (Insight DS + Dual, Spectra-Physics), 8 kHz resonant scanning module (Thorlabs), a ×16/0.8 NA/3 mm WD water immersion objective (Nikon, MRP07220) and GaAsP PMT (Hamamatsu H11706).

Motion correction of the raw movies, cell detection and signal extraction were performed as previously published using custom MATLAB scripts[12]. Significant fluorescence transients were identified as described in past studies[12,59,63] as events that started when signal was >2σ from the corrected baseline (computed from the full-time series but excluding large transients and corrected for slow fluctuations), and ended when it returned below 0.5σ of baseline. A 2σ threshold allowed to detect less than 1% of false positives (downward deflections).

Experimental recordings of CA1 during optogenetic inhibition of CA3

These experiments were performed by A.J. Eleven- to 15-week-old male and female Grik4-cre mice (same mouse line as mice used for the CA3 recordings described above) were injected either in the left or the right CA3 region (2.0 mm lateral, 1.7 mm or −1.7 mm caudal respective to Bregma) with a viral vector allowing CRE-dependent expression of the fast inhibitory opsin eOPN3 (ref. 64)—100 nl of pAAV-hSyn1-SIO-eOPN3-mScarlet-WPRE (Addgene, 125713) at a depth of 1.9 mm below the dura. After at least 2 weeks, another injection was performed to express GCaMP6f in the right CA1 region, following the same routine protocol as reported before[12].

Behavioral training on virtual tracks was performed as reported before[12], using the same virtual environments except that track length was shortened from 300 to 200 cm. The expression of eOPN3 in CA3 terminals was checked throughout training starting 4 weeks after injection. Experiments started once behavioral criterion was reached (2 laps per min for 5 days in a row) and the day after a visually obvious reduction in CA1 pyramidal cell activity had been observed during optostimulation (Supplementary Fig. 2b), which corresponded to 43.6 ± 20 days after GCaMP6f injection. Experiments reported here were part of a 6-day protocol, recording the same field of view, that will be detailed in further publications. Each imaging day consisted of navigation in the familiar environment (10 min) before switching to a new environment A, B or C (20 min). On some days, no optostimulation was provided, constituting the control condition. On other days, optostimulation was turned on for 3 min, either at the very start of the session in the new environment (opto-early) or after at least 16 laps during the session (opto-late). All mice experienced all three conditions (control, opto-early and opto-late) on different days. The order of conditions and their association with environments A, B or C was randomized. Opto-early and opto-late were combined for analysis.

Optostimulation consisted of 625 nm light delivered by an LED (Thorlabs) through the microscope objective, with pulse width of 30 ms (during which two-photon imaging was stopped), pulse margin of 5.25 ms (during which two-photon imaging was performed), frequency of 28.37 Hz, and ~3 min of duration. Two-photon imaging was performed as reported before[12] except no rubber tube was used to prevent stray light from the VR screens to enter the microscope lens. Average laser power after the objective was ~80 mW. Sampling rate was 31 Hz. A shutter stopped imaging during an opto-pulse but scanning continued at the same speed. The asynchrony between optostimulation and scanning resulted in missing lines for some frames. Each region of interest (ROI) had a slightly different effective sampling rate from the varying number of missing scan lines. The lowest effective sampling rate for a given ROI was ~10 Hz during optostimulation.

Imaging planes acquired on different days were combined and preprocessed using Suite2p[65]. Time-series images went through two times of rigid and nonrigid transformations in Suite2p to remove movement artifacts. Motion-corrected videos were visually assessed to ensure the absence of drifts in the z direction. Datasets with visible z drifts were discarded. ROIs were identified by suite2p and manually inspected for accuracy. For each ROI, baseline corrected $\Delta F/F$ traces were generated within each day and filtered for significant calcium transients as reported before[12]. When generating baseline corrected $\Delta F/F$ traces for a given ROI, missing frames in optogenetic conditions were linearly interpolated using the 'fillmissing' function in MATLAB. Downsampling the control data to match optostimulation conditions did not significantly affect the lap-wise PF COM (slope and R^2 of the regression both close to 1); we thus used the full dataset for our analysis.

PF selection

For the dataset from ref. 12, PFs were identified and defined as reported before, using a method combining criteria about the peak fluorescence, stability and size of the PF compared against chance levels[12,59,63,66]. Importantly, the criteria previously established were loose enough to not exclude shifting PFs. PFs too close to the beginning or end of the track were excluded[12]. PFs from the same cell were considered independent. All analyses were performed on PFs in which nonsignificant transients and transients outside the defined PF region were removed. PF onset, the emergence lap of a given PF, was detected as in ref. 12 by finding the first lap where (1) a significant transient occurred in the PF region and (2) this lap was followed by significant PF activity in two of five of the following laps.

A similar algorithm was used on the optogenetic experiment dataset but adapted to the different track length, larger number of laps and noisier recordings due to multiple experimental differences (lower sampling rate, longer GCaMP expression window before imaging necessary for opsin expression, light noise from the VR screens and more complex and randomized behavioral protocol). Note that because of these experimental differences, both datasets are not directly comparable. Potential PFs were identified as contiguous points on the mean tuning curve that had a minimum amplitude of 0.1 $\Delta F/F$ and >20% (instead of 15%) of the difference between peak ΔF/F and baseline values. PF width was constrained between 6% and 50% of the track length (as in ref. 12), and at least 30% of laps had to have a significant transient within the PF boundaries. We also tried a more stringent set of criteria, which did not affect our conclusions.

Analysis of PF trajectories

Analysis of PF shifting dynamics was based on the COM of the lap-wise binned activity of a given PF. Tracks of 300 cm were divided in 50 spatial bins of 6 cm whereas tracks of 200 cm were divided in 40 bins of 5 cm. The lap-wise normalized fluorescence F_i was averaged for each bin i. The COM on lap n was computed as follows:

$$\mathrm{COM}_n = \frac{\sum_i F_i \times x_i}{\sum_i F_i} \quad (1)$$

where x_i is the position of bin i on the track (that is, the distance from the start). For simulated data, the COM was computed in the same way, except that F_i was the firing rate (that is, the number of action potentials in bin i divided by the time spent in bin i). COM_n locations were then centered on $\mathrm{COM}_{\mathrm{onset}}$, that is, on the COM position during the emergence lap.

In recorded PFs, not all laps after onset necessarily show substantial activity. For the dimensionality reduction (Fig. 5) and diffusion analyses (Fig. 7c), we interpolated the COM location for the laps without activity that were intercalated with active laps. If PF activity disappeared and did not come back during the session, the final laps without activity were excluded. For all analyses except in Fig. 7b,c, we only included PFs that, after interpolation, were defined on at least 15 laps. For Fig. 7c, the inclusion criterion was set at a minimum of 30 laps (reducing the number of PFs but allowing a better picture of the long-term dynamics of PFs). A minimum number of laps with a defined PF is an obvious but important prerequisite to assess PF dynamics. However, neither the interpolation nor the minimum number of laps (0, 15 or 30) affected our conclusions.

To detect significant backward or forward linear shifts of the lap-wise COM, linear regression between onset-centered COM position (response variable) and lap number n (predictor variable) was performed using the Matlab 'regress' function, which provides a P value based on an F test. For the optogenetic dataset (Fig. 1d), the regression analysis was done on PFs that emerged during optostimulation (or equivalent laps in control condition) and defined for at least 15 laps during stimulation (laps after stimulation were excluded).

For the nonlinear regression analysis (Fig. 5), we used the Matlab 'fit' function with the nonlinear least squares method and trust region algorithm to fit the following function to each PF:

$$\mathrm{COM}_n = \mathrm{Amp}\left(1 - e^{-\frac{n}{\tau}}\right) + \varepsilon \quad (2)$$

where Amp (in cm), τ (in laps) and ε (in cm) are the parameters to fit and n is the lap number. The parameter search starting point was [14 cm, 2 laps, 0 cm] if the linear regression slope was positive and [−15 cm, 2 laps, 0 cm] otherwise. Parameter search was bounded and stopped in case absolute(Amp) = 200 cm or τ = 100 laps, or absolute(ε) = 25 cm.

To compare goodness-of-fit between linear and nonlinear regressions, we chose to compare the respective R^2 statistics (coefficient of determination). We did not use the adjusted R^2 for the nonlinear regression because the nonlinear model only has one parameter more than the linear model; overfitting was not a concern and the goal of the analysis was to determine the best description of a given PF trajectory, not to find an optimal model that would best predict out-of-sample data.

For the principal component analysis (PCA) and t-distributed stochastic neighbor embedding (tSNE) analyses (Fig. 5), all PF trajectories (a PF trajectory being a vector of onset-centered COM position) were truncated to only include the first 15 laps where the PF was defined (that is, 14 laps post-onset). We performed PCA ('pca' Matlab function) on the matrix of all the truncated PF trajectories aligned on their respective onset lap using the singular value decomposition algorithm. COM position was onset-centered, as described above, but trajectories were not centered on the average trajectory. Note that we also tried the same PCA analysis on noninterpolated data using the alternating least squares algorithm—conclusions were not affected. Nonlinear dimensionality reduction using tSNE was performed on the same matrix of interpolated and truncated PF trajectories as for the PCA singular value decomposition analysis.

For the diffusion analysis (Fig. 7c), PFs defined on less than 30 laps were excluded. All interpolated PF trajectories (interpolation ensuring that the sample size is constant from lap to lap) were onset-aligned and truncated at 30 laps. The MSD on a given lap was defined as the square of the onset-centered COM position averaged across all PFs. For a random walk in a one-dimensional environment such as our linear track, MSD = 2 × D × number of laps, where D is the diffusion coefficient[39]. In other words, COM shifts can be described by a random walk when D is constant, that is, when the MSD is a linear function of post-onset lap. D was assessed by linear regression of the MSD as a function of lap number, using the Matlab 'regress' function (excluding the first three laps, where we observed large nonlinear changes in MSD). Alternatively, to avoid assumptions about when the relationship becomes linear, we assessed the instantaneous diffusion coefficient D_n of lap n (Eq. 3) and fitted it with a decaying exponential to estimate D as the asymptote value of D_n (equation (4)).

$$D_n = \frac{\mathrm{MSD}_n - \mathrm{MSD}_{n-1}}{2} \quad (3)$$

$$D_n = p1\left(e^{-\frac{n-1}{p2}}\right) + D \quad (4)$$

Parameters $p1$, $p2$ and D were optimized using the Matlab 'fit' function with the nonlinear least squares method and trust region algorithm. The parameter search starting point was [100, 2, 0]. Parameter search was bounded such that $0 \le p1 \le 1{,}000$, $0 \le p2 \le 100$ and $0 \le D \le 20$.

PF width

Throughout the study, PF width was characterized by the standard deviation (s.d.) of PF activity:

$$\text{PF s.d.} = \sqrt{\sum_i \left(\frac{F_i}{\sum_i F_i} \times (x_i - \mathrm{COM})^2\right)} \quad (5)$$

where i is the spatial bin index on the track, F_i is either the normalized fluorescence (for experimental data) or firing rate (for simulated data) in bin i, x_i is the position of bin i and COM is the PF center of mass. PF width was the PF s.d. of PF activity averaged across all laps. We also computed the lap-wise PF s.d. and assessed the change in width (PF Δ width) as the difference between the first three laps and the last three laps.

Place cell model with plastic synapses following an STDP rule

To simulate experiments like in ref. 12, we considered a virtual mouse running unidirectionally on a 300-cm linear track at constant speed for 30 laps (the unidirectional motion with immediate teleportation

from end to start makes it equivalent to a circular track, as in ref. 25). We designed a simple feed-forward place cell model (Fig. 2a) that consisted of a leaky integrate-and-fire output neuron receiving weighted synaptic inputs from n_{in} spatially modulated input neurons, with one synapse per input neuron. Each input neuron generated spikes stochastically based on a nonhomogeneous Poisson process governed by a single Gaussian PF defined by its COM, peak firing rate (peak FR_{in}) and width (PF_{in} s.d.). The COM of input PFs regularly tiled the length of the track, and the initial connectivity vector followed a Gaussian defined by its s.d. (connectivity s.d.) and a maximum synaptic weight (W_{max}^{init}) for the input neuron with COM in the middle of the track. In this model, an input spike from neuron j results in an excitatory postsynaptic current (EPSC) with maximum amplitude at the time of the spike defined by the current synaptic weight, $w_j(t)$, of synapse j. EPSCs then exponentially decay with time constant τ_{EPSC}. The input current $I(t)$ to the LIF output neuron was computed based on the following ordinary differential equation (ODE):

$$\frac{dI}{dt} = -\frac{I(t)}{\tau_{EPSC}} + \sum_{j=1:n_{in}} w_j(t) \times \delta\left(t - t_j^{\text{input spike}}\right) \quad (6)$$

where $t_j^{\text{input spike}}$ is the time of an input spike at synapse j and $\delta(x)$ is 1 for $x = 0$ and 0 otherwise.

The membrane potential V_m of the LIF output neuron was governed by the following ODE[67]:

$$\tau_m \frac{dV_m}{dt} = V_{rest} - V_m(t) + I(t) \times R_m \quad (7)$$

where τ_m is the membrane time constant, V_{rest} is the resting membrane potential and R_m is the membrane resistance. Each time V_m reaches the spiking threshold V_{thresh}, an output spike is fired and V_m is reset to V_{reset}.

In Supplementary Figs. 5 and 6, we added spike-rate adaptation to the LIF equation using an additional variable, SRA, that exponentially relaxes to 0 after an increment of potassium leak current at each new output spike, as described in ref. 67:

$$\tau_m \frac{dV_m}{dt} = V_{rest} - V_m(t) - \text{SRA}(t) \times (V_m(t) - E_K) + I(t) \times R_m \quad (8)$$

$$\frac{d\text{SRA}}{dt} = -\frac{\text{SRA}(t)}{\tau_{SRA}} + a_{SRA} \times \delta(t - t_{\text{output spike}}) \quad (9)$$

where $E_K = -70$ mV is the equilibrium potential of potassium, $a_{SRA} = 0.06$ is the increment value for the SRA variable, and $\tau_{SRA} = 100$ ms is the time constant controlling the decay of the SRA variable. Parameter values were as in the example provided in Figs. 5 and 6 in ref. 67.

The synaptic weight of each synapse evolved independently following a pair-based STDP rule (Fig. 2b), where the weight of synapse j potentiates or depresses depending on the delay between a presynaptic spike and a postsynaptic spike as follows:

$$\Delta W_j = \begin{cases} A_{STDP} \times e^{-\frac{\Delta t}{\tau_{prepost}}}, \text{ if } \Delta t \le 0 \\ -A_{STDP} \times e^{-\frac{\Delta t}{\tau_{postpre}}}, \text{ if } \Delta t \ge 0 \end{cases} \quad (10)$$

where ΔW is the change in synaptic weight, A_{STDP} is the maximum amplitude that ΔW can take, $\tau_{prepost}$ and $\tau_{postpre}$ are the time constants of the exponential decay and $\Delta t = t_j^{\text{input spike}} - t^{\text{output spike}}$ (referred to as the pre-post delay in the rest of the study). Synaptic weights were updated additively using local eligibility variables for each input and output neurons[25,68,69]. For a given synapse j, the pre-before-post variable $P_{prepost}$ (corresponding to a negative prepost delay and thus to the potentiating portion of the STDP rule) is triggered on input spike times and decays with time constant $\tau_{prepost}$, whereas the post-before-pre variable $P_{postpre}$ (corresponding to a positive prepost delay and thus to the depressing portion of the STDP rule) is triggered on output spike times, decaying with time constant $\tau_{postpre}$. Time constants $\tau_{postpre}$ and $\tau_{prepost}$ were equal for antisymmetric rules. Weights were updated at each input and output spike times, evaluating $P_{prepost}$ on output spike times and $P_{postpre}$ on input spike times (Fig. 2b). Weight dynamics thus evolved as follows:

$$\frac{dP_j^{\text{prepost}}}{dt} = -\frac{P_j^{\text{prepost}}(t)}{\tau_{prepost}} + \delta\left(t - t_j^{\text{input spike}}\right) \quad (11)$$

$$\frac{dP_{postpre}}{dt} = -\frac{P_{postpre}(t)}{\tau_{postpre}} + \delta\left(t - t_{\text{output spike}}\right) \quad (12)$$

$$\frac{dW_j}{dt} = A_{STDP} \times P_j^{\text{prepost}}(t) \times \delta\left(t - t_{\text{output spike}}\right) - A_{STDP} \times P_{postpre}(t) \times \delta\left(t - t_j^{\text{input spike}}\right) \quad (13)$$

Weights were updated instantaneously unless otherwise stated (Fig. 2b). Because this is not realistic and that a previous model resulting in PF backward shifting implemented a delay (updating at the end of each lap)[15], we added some dynamics to the weight update in some simulations (Supplementary Figs. 5 and 6 and Fig. 7c). We designed a phenomenological model where the target weight W_{target} is set by equation (13), and the true weight W exponentially adjusts to that target with a time constant τ_{update} of 5 s ('Parameterization') based on the following equation (14):

$$\tau_{update} \frac{dW_j}{dt} = -W_j(t) + W_{target}(t) \quad (14)$$

Throughout, ODEs were solved using Euler's forward method, with a time step of 1 ms. Initial conditions were as follows: $V(0) = V_{rest}$; all other variables started at 0. Synapses were saturating unless otherwise stated—weights were hard-bounded by $EPSC_{min}$ (0 pA) and $EPSC_{max}$ (same value as W_{max}^{init}). The baseline parameters, corresponding to model 1 in Fig. 2c, are shown in Supplementary Table 1. Alternative parameters are directly mentioned in the figures and legends.

Parameterization

Virtual animal speeds (15 or 25 cm s^{-1}) generally corresponded to realistic individual average speeds in mouse experiments[12,23]. Speed of 50 cm s^{-1} was also tested for comparison with ref. 15, which modeled rats; however, this speed is unrealistically high for mice.

The parameters for the output LIF neuron were taken from ref. 69. They correspond to generic cortical pyramidal cell parameters and are within the range of observed values for CA1 pyramidal neurons[70,71] (https://neuroelectro.org/neuron/85/).

Input parameters were chosen to obtain CA1-like output PFs, with realistic width and firing rates (Supplementary Fig. 3). In mice, the median output peak FR_{out} in dorsal CA1 is ~10 Hz[61] and the median PF s.d. is 13.5 cm in the ref. 12 dataset. Realistic ranges are shown in Supplementary Fig. 3. We used inputs with Gaussian PFs inspired by CA3 recordings, but they can also be understood as an average of all spatial inputs to a pyramidal cell, including from the entorhinal cortex[38,72]. PF_{in} s.d. was chosen to be close to the median value that we observed in CA3 (Supplementary Fig. 3c). Peak FR_{in} matches reports from rats in CA3 (refs. 13,73) which are very close to firing rates observed in the CA1 of rats and mice[13,61]. τ_{EPSC} is within the range of observed values in CA pyramidal cells[70]. The number of input neurons (that is, synapses) was the same as in ref. 15, and the connectivity s.d. and maximum initial weight W_{max}^{init} were adjusted to obtain CA1-like PF_{out} s.d. and peak FR_{out} as defined above.

We also performed simulations with 1,000 input place cells (with connectivity s.d. at 100 i.n. and $W_{max}^{init} = 12$ pA), which is a more realistic

number of inputs and was used in other models[25,34], but results were similar and we thus kept 100 inputs as our baseline for computation speed. Although 100 input place cells are not realistic, note that the distribution of synaptic weights with W_{max}^{init} = 85 pA fits well with the amplitude of CA1 excitatory postsynaptic potentials (EPSPs) recorded in vivo or in vitro—EPSPs in vivo are 1.4 mV on average[70] and EPSPs evoked by Schaffer stimulation in slices were ~2 mV on average[30], which corresponds to 77 pA with our LIF parameters (Supplementary Fig. 12); dual patch experiments between CA3 and CA1 pyramidal cells yield excitatory postsynaptic currents (EPSCs) of similar amplitudes[74] and miniature EPSCs from a single synapse are 15 pA on average (range = 0–30 pA)[75].

In Fig. 2f and Supplementary Fig. 5, PF_{in} s.d., peak FR_{in} and connectivity s.d. were varied systematically within a realistic range for CA3. But to cover both realistic and unrealistic PF properties for CA1, we did not vary W_{max}^{init}, which also controls the output firing rates, because in our model it also conditioned the absolute maximum weight change, and we wanted to determine the effect of output rates without changing the amplitude of STDP. STDP parameters (A_{STDP} and time constants) were varied independently of input parameters in Supplementary Figs. 8–11.

STDP parameters were inspired from ref. 69. First, to maintain PFs with realistic peak FR_{in}, synapses were saturated with an upper bound of synaptic weights $EPSC_{max} = W_{max}^{init}$ unless otherwise noted (Supplementary Figs. 5 and 6). Concerning the amplitude of weight changes, although most STDP experiments report them relative to the initial weight of the recorded synapse and thus assume that synaptic modifications depend on the synaptic weight, we considered an additive weight update scheme where A_{STDP} is a constant, like in refs. 25,69. We made this choice for several reasons—(1) for simplicity and comparison with past models, (2) the weight dependency of STDP is not clear[68,76], especially given that initial weight is just one of many factors potentially influencing long-term synaptic modifications and generally not taken into account by a single STDP rule[11,26,27,44], (3) the additive scheme is a reasonable approximation, especially in the range of EPSCs used in our model[24,68,76] and (4) if synaptic modifications were weight dependent, an additive scheme like ours would slightly overestimate the effect of STDP for small initial weights, and thus overestimate, not underestimate, the effect of STDP on PF shifting. The baseline value for A_{STDP} was thus set at 0.5% of the maximum synaptic weight, as in ref. 69. However, please note that in contrast to refs. 25,69, synaptic weights were defined as EPSC amplitudes, not unitless conductances. In our model, the baseline absolute maximum weight change is thus 0.425 pA. The amplitude of weight changes due to single pairs of input–output spikes is difficult to assess[77], but the relative and absolute values that we used were in the range of previous estimates; ref. 24 estimates A_{STDP} to be ~1% of the initial EPSC, and, for initial EPSCs between 30 and 100 pA, their data show a maximum weight change between ~0.15 and ~0.5 pA[68]. For different STDP protocols and rules, and for a range of initial EPSCs comprising the value of our $EPSC_{max}$, the data in ref. 27 suggest A_{STDP} to be ~0.5% of the initial EPSCs like we used. To make sure we were not underestimating the effects of STDP, we also explored a range of A_{STDP} values in Supplementary Figs. 9 and 10—0.5%, 1%, 2%, 4% or 10% of $EPSC_{max}$, that is, 0.425, 0.85, 1.7, 3.4 and 8.5 pA (most of these values being outside a realistic range). We did similarly for STDP's time constants and explored a range of values in Supplementary Figs. 8–10, including the usual estimates (10 ms or 20 ms) and up to unrealistic values (100 ms).

For models including a synaptic update with dynamic delay, the value of τ_{update} (5 s) was not optimized but grossly corresponds to the dynamics of the early expression phase of LTP[78] and is consistent with the seconds-long timescale of the calcium-dependent enzymatic activation controlling the rapid surface diffusion of AMPA receptors necessary for the earliest phase of LTP[79,80].

A comparison of our baseline model with the seminal models of backward PF shifting using STDP can be seen in Supplementary Table 2.

BTSP + homeostasis model

The model described above was adapted to have BTSP rather than STDP as the plasticity rule (baseline parameters of Supplementary Table 1 were used unless otherwise stated).

BTSP is known to be triggered by a dendritic plateau potential resulting in a large depolarization with a somatic burst of spikes also called a complex spike (CS)[23,30,32,33]. Because the mechanisms leading to a CS and triggering BTSP are not well understood, we first opted to model BTSP-triggering events simply as a special subset of output spikes, with each regular output spike having a probability p(CS) to be labeled as a CS. In Figs. 3 and 4, p(CS) was constant. In Fig. 7, we designed a more complex model where p(CS) was dynamic—the lap-wise p(CS) followed a decaying exponential $A_{cs} \times \exp(-\text{lap}/\tau_{cs}) + B_{cs}$, where B_{cs} is the baseline frequency of CSs per lap, $A_{cs} + B_{cs}$ is the maximum p(CS) on the first lap after PF emergence and τ_{cs} is the time constant of the decay. Moreover, to allow for occasional out-of-field CSs, the CSs were not directly selected from output spikes, but their location on the track was randomly sampled from a Gaussian distribution with s.d. σ_{cs} and centered on the COM of the synaptic weights at the beginning of the lap. To ensure that the average PF width stayed within the bounds of what we observed in CA1, CSs could only occur ±60 cm around the initial PF COM.

The BTSP rule was defined as a pure potentiation rule, as reported in ref. 30, with the following kernel (Fig. 3a):

$$\Delta W_j^P = \begin{cases} A_{BTSP} \times e^{-\frac{\Delta t}{\tau_{prepost}}}, \text{if } \Delta t \le 0 \\ A_{BTSP} \times e^{-\frac{\Delta t}{\tau_{postpre}}}, \text{if } \Delta t \ge 0 \end{cases} \quad (15)$$

where ΔW_j^P is the potentiation at synapse j due to BTSP and A_{BTSP} is the maximum potentiation. To avoid runaway potentiation and maintain a PF, as observed in ref. 23, synaptic weights were not bounded like for the STDP model but obeyed a simple homeostatic rule keeping the total sum of weights constant at each time step. We implemented that homeostatic heterosynaptic plasticity as a weight-dependent synaptic normalization, using a multiplicative scheme[3,81], such that for all synapses.

$$W_j(t+1) = \left(W_j(t) + \Delta W_j^P\right) \times \frac{\sum_{j=1:n_{in}} W_j(t_0)}{\sum_{j=1:n_{in}} \left(W_j(t) + \Delta W_j^P\right)} \quad (16)$$

with $\Delta W_j^P = 0$ when no potentiation occurred at synapse j.

BTSP-triggered synaptic potentiation was implemented like for STDP (equations (11) and (12)), using two plasticity variables $P_{prepost}$ and $P_{postpre}$. However, $P_{postpre}$ was not triggered on all output spikes but on CSs, and $P_{prepost}$ was evaluated at the times of CSs only:

$$\frac{dP_{postpre}}{dt} = -\frac{P_{postpre}(t)}{\tau_{postpre}} + \delta\left(t - t_{output\ CS}\right) \quad (17)$$

$$\frac{dW_j^P}{dt} = A_{BTSP} \times P_j^{prepost}(t) \times \delta\left(t - t_{output\ CS}\right) + A_{BTSP} \times b \times P_{postpre}(t) \times \delta\left(t - t_j^{input\ spike}\right) \quad (18)$$

Because there is more temporal summation in the $P_{prepost}$ variable than in $P_{postpre}$, as there are generally more input spikes than output CSs, we added a scaling constant b to fit the BTSP kernel on the post-before-pre side ('Validation of our BTSP + homeostasis model'; Supplementary Fig. 12).

Updating dynamics of synaptic weights after BTSP are not well characterized. In the initial version of the model (Figs. 3 and 4), we opted for an instantaneous weight update like for our baseline STDP model. This lack of realism does not impair our conclusions on PF dynamics—most changes due to BTSP are visible on the lap following a BTSP-triggering event[23,30]. So, in our simulations, even if the PF activity

is perturbed after a CS on the lap the CS occurred, the PF activity and overall shift will be as expected on the next lap.

Parameters used in Fig. 3 are as follows: $\tau_{prepost} = 1.31$ s, $\tau_{postpre} = 0.69$ s, $A_{BTSP} = 20$ pA, $b = 1.1$ and instantaneous weight update. Same for CA3-like models in Fig. 4, except for $\tau_{prepost}$ and $\tau_{postpre}$ (reported in legend of Fig. 4). Parameters used in Fig. 7 are as follows: $\tau_{prepost} = 1.5$ s, $\tau_{postpre} = 0.2$ s, $A_{BTSP} = 80$ pA, $b = 1.1$ and dynamic weight update with $\tau_{update} = 15$ s. The dynamic p(CS) parameters for the novel/familiar-like conditions, are as follows, respectively: $A_{cs} = 0.65/0.6$, $B_{cs} = 0.025/0.0125$, $\tau_{cs} = 1.3/1$ lap and $\sigma_{cs} = 29/21$ cm.

Validation of our BTSP + homeostasis model

We optimized the BTSP model parameters to account for the experimental findings from the Magee lab[23,30]. BTSP time constants $\tau_{prepost}$ and $\tau_{postpre}$ were directly taken from ref. 30 (based on the exponential fit of their in vitro dataset). The scaling constant b was adjusted by simulating in vitro experiments like in ref. 30, so that the maximum potentiation due to BTSP (that is, without synaptic normalization) would match for both the pre-before-post and post-before-pre part of the kernel and fit the data (Supplementary Fig. 12). The optimized value of b is very close to 1, so it does not influence our conclusions.

For our homeostatic plasticity rule, we preferred a multiplicative scheme (rather than subtractive) because competition between synaptic resources has been shown to result in such rapid synaptic scaling[52]. By design, synaptic normalization operated on the same rapid timescale as BTSP, which is justified on theoretical grounds and has some experimental support[3].

To optimize A_{BTSP} and to verify that our modeling strategy of combining a BTSP potentiation rule with synaptic normalization yields bidirectional weight changes dependent on the initial weight observed in vivo in ref. 23, we simulated the same kind of experiments and analyzed our resulting dataset in the same way they reported (Supplementary Figs. 13–15). 'Milstein-type' experiments consisted of simulating a place cell for 21 laps, with a single CS occurring on lap 11 at a time t_{CS}, which was varied systematically to cover the length of the track (there was no relationship between output spikes and the CS in these experiments; t_{CS} was hard-coded). Baseline parameters of our place cell model were used except for the track length (185 cm) and virtual animal speed (25 cm s^{-1}), which were the same as in ref. 23. Synaptic weights were updated following the combined BTSP and synaptic normalization rule.

We analyzed subthreshold V_m ramps like in ref. 23. First, the V_m output of the LIF neuron was low-pass filtered (<3 Hz) with zero-phase lag ('filtfilt' Matlab function) using a FIR filter with a 2 s Hamming window and wrap-around padding of the V_m trace on each lap. For the V_m spatial profiles, the low-passed filtered V_m traces were binned using 1.85 cm regularly spaced bins and averaged across the ten laps before or after the CS induction lap. These average traces were smoothed with a Savitzky–Golay filter of order three with a window size of 21 spatial bins and wrap-around padding. Temporal profiles of the low-pass filtered V_m (Supplementary Fig. 13c) were binned using the same number of bins as for spatial profiles but not smoothed. The relative amplitude of V_m ramps (used in Supplementary Figs. 14g and 15g) was computed as the difference of the average V_m trace with the V_m baseline, that is, $V_{rest} = -70$ mV.

Because our goal was to develop a model accurately predicting PF shifting based on BTSP, the optimization objective was to match the high correlation observed in ref. 23 between the ramp peak shift and the distance between the initial peak and CS, while maintaining a low correlation between pre and post-CS V_m (Supplementary Figs. 14 and 15). Our model reproduced key experimental findings, including an apparent weight-dependent bidirectional rule very similar to what was estimated in ref. 23 (Supplementary Fig. 14). This rule was computed by linear interpolation of the simulated V_m temporal profiles and the corresponding relative amplitudes of the V_m ramps, using the MATLAB 'fit' function.

Our approach offers a good fit to the available data on BTSP but is different from past modeling approaches[23,37] and thus has different potential shortcomings:

1. In our model, only one CS is needed to reach a steady state—adding more induction laps in our Milstein-type simulations does not significantly change the shape of the connectivity vector, which is why we used only one induction lap rather than three like in the calibration procedure used in ref. 23 for the network model. Whether this one-shot reconfiguration of weights is supported or not by the data is not clear—in ref. 23, multiple induction laps were generally used, but the number of artificially triggered CSs necessary to induce a new PF was variable (Supplementary Fig. 1 in ref. 23 and Supplementary Fig. 7 in ref. 82). Moreover, there is experimental evidence that a single spontaneous CS can be sufficient for a new PF to emerge in one shot[23,32]. Some of the variability could be due to artificial somatic inductions that may not always trigger calcium plateaus in every dendrite consistently, or not trigger the exact same molecular chain of events than spontaneous dendritic plateaus. More data are needed to clarify how the phenomenology of dendritic plateaus and BTSP covary. Similarly, more experiments and analysis are needed to determine whether BTSP-induced depression of the initial PF is slower than emergence of a new one, as predicted by previous models[23,37].
2. Because synaptic normalization affects all synapses irrespective of the recency of their activity, synaptic potentiation may be underestimated (and depression overestimated) when the CS occurs far from the initial PF. This can result in a relative flattening of the connectivity (Supplementary Fig. 13) and a dilution of the PF activity rather than its translocation, which does not seem to match the Milstein dataset (the maximum increase in V_m was on average larger than the maximum decrease, which was not the case in our simulations). Moreover, connectivity flattening, and thus PF dilution, increases with animal speed (because more inputs are potentiated), making it hard to study the effects of this parameter. However, PF dilution can be limited by increasing the amplitude of the potentiating rule.

Despite these limitations, our model fits Milstein-type translocation experiments well when CSs occur in-field (Supplementary Fig. 14), which was always the case, by definition, in our in silico experiments for the study of PF dynamics (Figs. 3, 4 and 7d), because CS occurrence was tied to PF activity. PF dilution did not occur in these simulations; our model is therefore well suited to study the effect of BTSP on PF dynamics.

Homosynaptic bidirectional BTSP model

To confirm results based on our BTSP + homeostasis model described above, where BTSP was a purely potentiating rule, we adapted the homosynaptic weight-dependent bidirectional BTSP model developed in ref. 23. This homosynaptic model relies on two plasticity variables $P_{prepost}$ (synaptic eligibility trace defined by equation (11)) and $P_{postpre}$, a global instructive signal triggered on CSs (equation (17)). As before, output spikes are randomly selected as CSs with probability p(CS). However, to match Milstein's original model, a CS was not a single spike as before but a plateau of 300 ms, starting at the time of the selected output spike. Synaptic weights were updated at the end of each lap, using the following weight-dependent rule with lower bound at 0 pA and upper bound at W_{max}.

$$\frac{dW_j}{dt} = (W_{max} - W_j) \times k_p \times q_p(t) - W_j \times k_d \times q_d(t) \quad (19)$$

where k_p and k_d are the potentiation and depression rates, and q_p and q_d are the gains for potentiation and depression. To compute q_p and q_d, the synaptic eligibility trace of synapse j (ET_j) and global

instructive signal (IS) of each lap are normalized to be constrained between 0 and 1 (normET$_j$, normIS), by dividing with the peak of the respective trace up to that point. The product of normET$_j$ and normIS determines the gains as follows: $q_p(t) = s_p(\text{normET}(t) \times \text{normIS}(t), a_p, b_p)$ and $q_d(t) = s_d(\text{normET}(t) \times \text{normIS}(t), a_d, b_d)$, with s being a sigmoid function defined by its threshold a and slope b, such that $s(0) = 0$, $s(1) = 1$ and with s_d saturating faster than s_p (see ref. 23 for the exact formula). In practice, q_p and q_d were computed by integrating over the whole lap, using the MATLAB 'trapz' function, before updating synaptic weights at the end of each lap.

Parameters used in Supplementary Fig. 16 are as follows: $W_{max} = 125$ pA, $\tau_{prepost} = 2$ s, $\tau_{postpre} = 1.5$ s, $k_p = 1.2\ s^{-1}$, $k_d = 0.2\ s^{-1}$, $a_p = 0.5$, $b_p = 4$, $a_d = 0.01$, $b_d = 44$. Except for W_{max}, which is specific to our place cell model and expressed as a current, these parameters were slightly adapted from Fig. 5. of ref. 23. W_{max} was optimized to lead to PF translocation after a single CS, maintain a PF if the CS occurred near the current COM and keep realistic firing rates and PF width (baseline place cell parameters were used).

Statistics and reproducibility

No statistical method was used to predetermine the sample size. No data that passed the objective criteria detailed in 'PF selection' were excluded. Experimenters were not blinded to CA1 or CA3 groups. For optogenetic experiments, the experimental design was randomized as described above. Analysis was performed by someone different from the experimenters, blind to treatments. Data collection and analysis were performed with automated software, with the same settings used across all animal subjects. Analyses and simulations were performed using MATLAB (R2021b) on a Dell laptop (Mobile Precision Workstation 3560, i7-1185G7 processor, 16GB RAM, NVIDIA T500 2GB GPU). Statistical details can be found in figure legends. In general, we aimed to use estimation statistics as our main line of evidence, focusing on the effect size and CI estimates rather than the significance of *P* values[83,84]. Exact tests based on resampling were favored because the sample size was too large for classic hypothesis testing to provide meaningful *P* values[85]. Bootstrapped estimates and CIs were computed with the 'bootci' function or the DABEST package[84], with 5,000 or 10,000 bootstrap samples and BCa method. The effect on medians rather than means was evaluated when the sample distribution was not Gaussian. In Fig. 5c, we performed a two-way ANOVA with the Matlab function 'anova' based on a linear mixed-effects model built using the function 'fitlme'. Violin plots were generated using code from ref. 86 to visualize distributions, mean (horizontal bar), median (open circle) and quartiles (gray whiskers).

Reporting summary

Further information on research design is available in the Nature Portfolio Reporting Summary linked to this article.

Data availability

Experimental data were previously reported in ref. 12 and will be made available upon request. The processed data used for analysis are available at https://github.com/antoinemadar/BTSPvsSTDP. Source data are provided with this paper.

Code availability

Data preprocessing and PF selection were performed with code available at: https://github.com/Candong/Distinct_CA1_CA3. Additional Matlab custom code used for the present study is available at: https://github.com/antoinemadar/BTSPvsSTDP.

References

62. Krishnan, S., Heer, C., Cherian, C. & Sheffield, M. E. J. Reward expectation extinction restructures and degrades CA1 spatial maps through loss of a dopaminergic reward proximity signal. *Nat. Commun.* **13**, 6662 (2022).
63. Dombeck, D. A., Harvey, C. D., Tian, L., Looger, L. L. & Tank, D. W. Functional imaging of hippocampal place cells at cellular resolution during virtual navigation. *Nat. Neurosci.* **13**, 1433–1440 (2010).
64. Mahn, M. et al. Efficient optogenetic silencing of neurotransmitter release with a mosquito rhodopsin. *Neuron* **109**, 1621–1635 (2021).
65. Pachitariu, M. et al. Suite2p: beyond 10,000 neurons with standard two-photon microscopy. Preprint at *bioRxiv* https://doi.org/10.1101/061507 (2017).
66. Grijseels, D. M., Shaw, K., Barry, C. & Hall, C. N. Choice of method of place cell classification determines the population of cells identified. *PLoS Comput. Biol.* **17**, e1008835 (2021).
67. Dayan, P. & Abbott, L. F. *Theoretical Neuroscience: Computational and Mathematical Modeling of Neural Systems* (MIT Press, 2005).
68. Morrison, A., Diesmann, M. & Gerstner, W. Phenomenological models of synaptic plasticity based on spike timing. *Biol. Cybern.* **98**, 459–478 (2008).
69. Song, S., Miller, K. D. & Abbott, L. F. Competitive Hebbian learning through spike-timing-dependent synaptic plasticity. *Nat. Neurosci.* **3**, 919–926 (2000).
70. Kowalski, J., Gan, J., Jonas, P. & Pernía-Andrade, A. J. Intrinsic membrane properties determine hippocampal differential firing pattern in vivo in anesthetized rats. *Hippocampus* **26**, 668–682 (2016).
71. Tripathy, S. J., Savitskaya, J., Burton, S. D., Urban, N. & Gerkin, R. C. NeuroElectro: a window to the world's neuron electrophysiology data. *Front. Neuroinform.* **8**, 40 (2014).
72. Solstad, T., Moser, E. I. & Einevoll, G. T. From grid cells to place cells: a mathematical model. *Hippocampus* **16**, 1026–1031 (2006).
73. Lee, H., Wang, C., Deshmukh, S. S. & Knierim, J. J. Neural population evidence of functional heterogeneity along the CA3 transverse axis: pattern completion versus pattern separation. *Neuron* **87**, 1093–1105 (2015).
74. Dürst, C. D. et al. Vesicular release probability sets the strength of individual Schaffer collateral synapses. *Nat. Commun.* **13**, 6126 (2022).
75. Forti, L., Bossi, M., Bergamaschi, A., Villa, A. & Malgaroli, A. Loose-patch recordings of single quanta at individual hippocampal synapses. *Nature* **388**, 874–878 (1997).
76. Morrison, A., Aertsen, A. & Diesmann, M. Spike-timing-dependent plasticity in balanced random networks. *Neural Comput.* **19**, 1437–1467 (2007).
77. Froemke, R. C., Tsay, I. A., Raad, M., Long, J. D. & Dan, Y. Contribution of individual spikes in burst-induced long-term synaptic modification. *J. Neurophysiol.* **95**, 1620–1629 (2006).
78. Gustafsson, B., Asztely, F., Hanse, E. & Wigstrom, H. Onset characteristics of long-term potentiation in the guinea-pig hippocampal CA1 region in vitro. *Eur. J. Neurosci.* **1**, 382–394 (1989).
79. Penn, A. C. et al. Hippocampal LTP and contextual learning require surface diffusion of AMPA receptors. *Nature* **549**, 384–388 (2017).
80. Rodrigues, Y. E., Tigaret, C., Marie, H., O'Donnell, C. & Veltz, R. A stochastic model of hippocampal synaptic plasticity with geometrical readout of enzyme dynamics. *eLife* **12**, e80152 (2023).
81. Kim, S., Jung, D. & Royer, S. Place cell maps slowly develop via competitive learning and conjunctive coding in the dentate gyrus. *Nat. Commun.* **11**, 4550 (2020).
82. Milstein, A. D. et al. Bidirectional synaptic plasticity rapidly modifies hippocampal representations independent of correlated activity. Preprint at *bioRxiv* https://doi.org/10.1101/2020.02.04.934182 (2020).
83. Gardner, M. J. & Altman, D. G. Confidence intervals rather than *P* values: estimation rather than hypothesis testing. *Br. Med. J. (Clin. Res. Ed.)* **292**, 746–750 (1986).
84. Ho, J., Tumkaya, T., Aryal, S., Choi, H. & Claridge-Chang, A. Moving beyond *P* values: data analysis with estimation graphics. *Nat. Methods* **16**, 565–566 (2019).

85. White, J. W., Rassweiler, A., Samhouri, J. F., Stier, A. C. & White, C. Ecologists should not use statistical significance tests to interpret simulation model results. *Oikos* **123**, 385–388 (2014).
86. Bechtold, B. Violin plots for Matlab. *Github* https://github.com/bastibe/Violinplot-Matlab; https://doi.org/10.5281/zenodo.4559847 (2016).

Acknowledgements

We thank A. Milstein (Rutgers University) and Y. Burak (Hebrew University of Jerusalem) for helpful discussions and J. Jaramillo (University of Chicago) and L. Giocomo (Stanford University) for their feedback on the manuscript. This work was supported by the National Institute of Neurological Disorders and Stroke of the NIH (DP2NS111657 to M.S.) and the National Institute of Mental Health of the NIH (F32MH126643; to A.M.), the Whitehall Foundation (to M.S.), the Searle Scholars Program (to M.S.) and the Sloan Foundation (to M.S.). The funders had no role in study design, data collection and analysis and the decision to publish or preparation of the manuscript.

Author contributions

A.M. and M.S. conceptualized the project, acquired funding and administered the project. A.J. and C.D. collected the data. A.J., C.D. and A.M. curated the data. M.S. supervised the project. A.M. conducted formal analysis, developed the methodology and software, created illustrations and data visualization and wrote the original draft of the manuscript. A.M., M.S., C.D. and A.J. reviewed and edited the manuscript.

Competing interests

The authors declare no competing interests.

Additional information

Supplementary information The online version contains supplementary material available at https://doi.org/10.1038/s41593-025-01894-6.

Correspondence and requests for materials should be addressed to Antoine D. Madar or Mark E. J. Sheffield.

Peer review information *Nature Neuroscience* thanks the anonymous reviewers for their contribution to the peer review of this work.

nature portfolio

Corresponding author(s): Antoine Madar, Mark Sheffield

Last updated by author(s): 11/22/2024

Reporting Summary

Nature Portfolio wishes to improve the reproducibility of the work that we publish. This form provides structure for consistency and transparency in reporting. For further information on Nature Portfolio policies, see our Editorial Policies and the Editorial Policy Checklist.

Statistics

For all statistical analyses, confirm that the following items are present in the figure legend, table legend, main text, or Methods section.

n/a	Confirmed	
☐	☒	The exact sample size (*n*) for each experimental group/condition, given as a discrete number and unit of measurement
☐	☒	A statement on whether measurements were taken from distinct samples or whether the same sample was measured repeatedly
☐	☒	The statistical test(s) used AND whether they are one- or two-sided *Only common tests should be described solely by name; describe more complex techniques in the Methods section.*
☐	☒	A description of all covariates tested
☐	☒	A description of any assumptions or corrections, such as tests of normality and adjustment for multiple comparisons
☐	☒	A full description of the statistical parameters including central tendency (e.g. means) or other basic estimates (e.g. regression coefficient) AND variation (e.g. standard deviation) or associated estimates of uncertainty (e.g. confidence intervals)
☐	☒	For null hypothesis testing, the test statistic (e.g. *F*, *t*, *r*) with confidence intervals, effect sizes, degrees of freedom and *P* value noted *Give P values as exact values whenever suitable.*
☒	☐	For Bayesian analysis, information on the choice of priors and Markov chain Monte Carlo settings
☐	☒	For hierarchical and complex designs, identification of the appropriate level for tests and full reporting of outcomes
☐	☒	Estimates of effect sizes (e.g. Cohen's *d*, Pearson's *r*), indicating how they were calculated

Our web collection on statistics for biologists contains articles on many of the points above.

Software and code

Policy information about availability of computer code

Data collection	Software used to collect the data were previously reported in Dong, Madar and Sheffield (2021) in Nature Communications: VR environments were created using VIRMEn, an open source software for VR experiment design. Imaging data collection was done using a laser scanning two-photon microscope (Neurolabware). Mice behavior including treadmill running speed, position, and licking and imaging signal were collected using the PicoScope Oscilloscope (PICO4824, Pico Technology).
Data analysis	Data preprocessing and place field selection was performed with code available at the following Github public repository: https://github.com/Candong/Distinct_CA1_CA3. Additional Matlab custom codes used for the present study is available at https://github.com/antoinemadar/BTSPvsSTDP

For manuscripts utilizing custom algorithms or software that are central to the research but not yet described in published literature, software must be made available to editors and reviewers. We strongly encourage code deposition in a community repository (e.g. GitHub). See the Nature Portfolio guidelines for submitting code & software for further information.

Data

Policy information about availability of data

All manuscripts must include a data availability statement. This statement should provide the following information, where applicable:

- Accession codes, unique identifiers, or web links for publicly available datasets
- A description of any restrictions on data availability
- For clinical datasets or third party data, please ensure that the statement adheres to our policy

Experimental data was previously reported in Dong et al. (2021) and will be made available upon request. The processed data used for analysis is available at: https://github.com/antoinemadar/BTSPvsSTDP

Research involving human participants, their data, or biological material

Policy information about studies with human participants or human data. See also policy information about sex, gender (identity/presentation), and sexual orientation and race, ethnicity and racism.

Reporting on sex and gender	N/A
Reporting on race, ethnicity, or other socially relevant groupings	N/A
Population characteristics	N/A
Recruitment	N/A
Ethics oversight	N/A

Note that full information on the approval of the study protocol must also be provided in the manuscript.

Field-specific reporting

Please select the one below that is the best fit for your research. If you are not sure, read the appropriate sections before making your selection.

☒ Life sciences ☐ Behavioural & social sciences ☐ Ecological, evolutionary & environmental sciences

For a reference copy of the document with all sections, see nature.com/documents/nr-reporting-summary-flat.pdf

Life sciences study design

All studies must disclose on these points even when the disclosure is negative.

Sample size	No statistical method was used to predetermine sample size.
Data exclusions	No data that passed the objective criteria detailed in the “PF selection” section were excluded.
Replication	CA1 recordings were done in 4 mice, CA3 recordings in 7 mice and optogenetic experiments in 9 mice. All replications were successful, as reported in Fig 1, Supplementary Fig 1 and 2.
Randomization	Mice were randomly chosen and the data was collected from multiple groups from different litters. For optogenetic experiments, the order of conditions and their association with environment A, B or C was randomized.
Blinding	All data collection and analysis was performed with automated software, with the same settings used across all animal subjects. Two Investigators handled the animals, following the same procedure. Investigators were not blinded to CA1 or CA3 groups. The analysis was performed by a different investigator, blind to treatments.

Reporting for specific materials, systems and methods

We require information from authors about some types of materials, experimental systems and methods used in many studies. Here, indicate whether each material, system or method listed is relevant to your study. If you are not sure if a list item applies to your research, read the appropriate section before selecting a response.

Materials & experimental systems

n/a	Involved in the study
☒	☐ Antibodies
☒	☐ Eukaryotic cell lines
☒	☐ Palaeontology and archaeology
☐	☒ Animals and other organisms
☒	☐ Clinical data
☒	☐ Dual use research of concern
☒	☐ Plants

Methods

n/a	Involved in the study
☒	☐ ChIP-seq
☒	☐ Flow cytometry
☒	☐ MRI-based neuroimaging

Animals and other research organisms

Policy information about studies involving animals; ARRIVE guidelines recommended for reporting animal research, and Sex and Gender in Research

Laboratory animals	10-12 week old C57BL/6J wildtype (WT) male mice (23-33g) (4 WT for CA1 population imaging, Jackson Lab 000664) and C57BL/6-Tg(Grik4-cre)G32-4Stl/J (7 for CA3 population imaging, Jackson Lab, 006474; 10 for optogenetic experiments) were used.
Wild animals	No wild animals were used for this study.
Reporting on sex	Experiments were conducted on male and female mice, as reported.
Field-collected samples	No samples were collected from the field.
Ethics oversight	IACUC of the University of Chicago

Note that full information on the approval of the study protocol must also be provided in the manuscript.

Plants

Seed stocks	*Report on the source of all seed stocks or other plant material used. If applicable, state the seed stock centre and catalogue number. If plant specimens were collected from the field, describe the collection location, date and sampling procedures.*
Novel plant genotypes	*Describe the methods by which all novel plant genotypes were produced. This includes those generated by transgenic approaches, gene editing, chemical/radiation-based mutagenesis and hybridization. For transgenic lines, describe the transformation method, the number of independent lines analyzed and the generation upon which experiments were performed. For gene-edited lines, describe the editor used, the endogenous sequence targeted for editing, the targeting guide RNA sequence (if applicable) and how the editor was applied.*
Authentication	*Describe any authentication procedures for each seed stock used or novel genotype generated. Describe any experiments used to assess the effect of a mutation and, where applicable, how potential secondary effects (e.g. second site T-DNA insertions, mosiacism, off-target gene editing) were examined.*

21 Supplementary Figures and 2 Tables

Associated to Fig. 1:

- Supplementary Figure 1. Animal-wise effects of novelty on proportion and amplitude of PF shifting
- Supplementary Figure 2. Optogenetic inhibition of unilateral CA3 projections during 2P imaging of CA1

Associated to Fig. 2:

- Supplementary Table 1. Baseline Parameters
- Supplementary Table 2. Comparison of our baseline model with seminal studies
- Supplementary Figure 3. Place Field width and output firing rates in simulated and recorded place cells
- Supplementary Figure 4. Model of dynamic input PFs
- Supplementary Figure 5. More realistic weight update and output firing patterns do not increase PF backward shifting.
- Supplementary Figure 6. STDP main effect is an unrealistic increase in output rates and PF width.
- Supplementary Figure 7. Exploration of the parameter space: inputs and animal speed
- Supplementary Figure 8. Exploration of the parameter space: anti-symmetric STDP rules
- Supplementary Figure 9. Exploration of the parameter space: anti-symmetric STDP rules at high input rates and high speed
- Supplementary Figure 10. Exploration of the parameter space: asymmetric STDP rules
- Supplementary Figure 11. Effects of STDP triplet rules on PF shifting

Associated to Fig. 3:

- Supplementary Figure 12. Optimization of our BTSP model to match findings from Bittner et al. 2017
- Supplementary Figure 13. Simulations of experiments as in Milstein et al. 2021: Effect of a single BTSP-triggering event on the pre-existing PF of our place cell model
- Supplementary Figure 14. A combination of BTSP and synaptic normalization yields an emergent weight-dependent bidirectional plasticity rule and accounts for PF shifts observed in Milstein et al. 2021.
- Supplementary Figure 15. Characterization of CS-induced PF shifts and emergent weight-dependence of the model used in Figure 3
- Supplementary Figure 16. BTSP modeled as a weight-dependent bidirectional rule can also cause CA1-like PF shifting.

Associated to Fig. 5:

- Supplementary Figure 17. Principal components and their distribution for all CA1 and CA3 PFs trajectories combined

Associated to Fig. 6:

- Supplementary Figure 18. Covariation of the non-linear regression parameters in single PFs
- Supplementary Figure 19. Distributions of non-linear regression parameters grouped by conditions

Associated to Fig. 7:

- Supplementary Figure 20. COM shifts after onset
- Supplementary Figure 21. Linear regression analysis on BTSP models with dynamic p(CS)

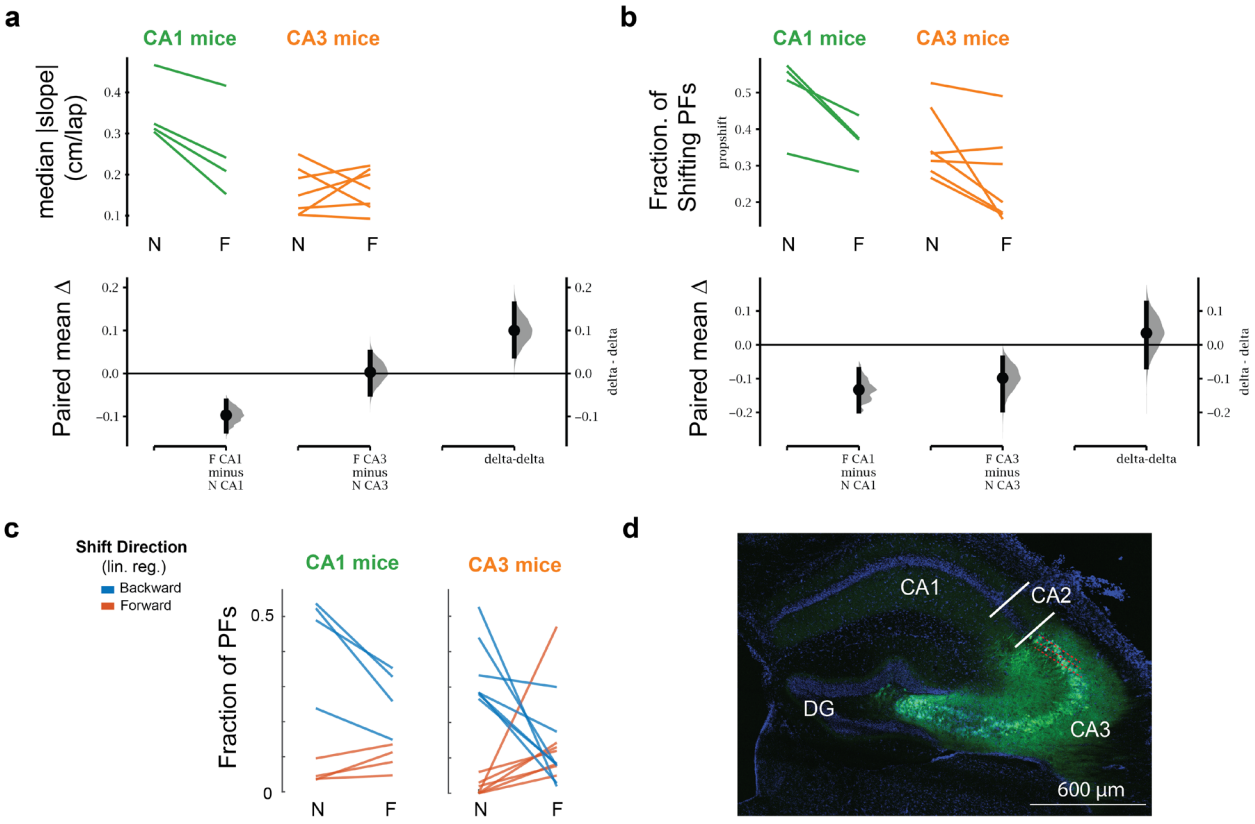

Supplementary Figure 1 (associated to Fig. 1).

Animal-wise effects of environment novelty on amplitude and proportion of PF shifting

Colored lines are individual mice (n = 4 for CA1, 7 for CA3), in the Novel condition (N) or Familiar condition (F).

a. Effect on median absolute slope (shifting speed) from the linear regressions computed on all the PFs for each mouse. The bottom graph shows the bootstrapped distribution of the difference between F and N conditions (grey) and the mean difference and 95% CI (black). The animal-wise median shifting speed significantly decreases in CA1 in familiar environments but not in CA3. The delta-delta plot corresponds to the bootstrapped distribution of the difference between the CA1 and CA3 distributions on the left: it indicates the interaction between the Hippocampal Subfield (CA1 vs CA3) and the Familiarity (N vs F) variables. Here, the interaction is significant.

b. Same as A but for the fraction of significantly shifting PFs (i.e. with F-test p-value of the linear regression on a given PF < 0.05, Backward and Forward combined). The interaction is not significant between Subfield and Familiarity, as both CA1 and CA3 have a significant decrease of shifting PFs in the familiar environment.

c. Fraction of significantly backward (blue) and forward (red) shifting PFs in CA1 and CA3. For all animals, the proportion of backward shifting decreases and the proportion of forward shifting increases.

d. Representative example confocal image of a brain slice from one of the recorded Grik4-cre mouse, showing DAPI staining in blue and specific CA3 expression of cre-dependent GCaMP6f in green. Red dashed lines represent the position of 3 fields of view during recording. Imaging planes were separated by at least 40µm. Similar histology was replicated on 3 animals.

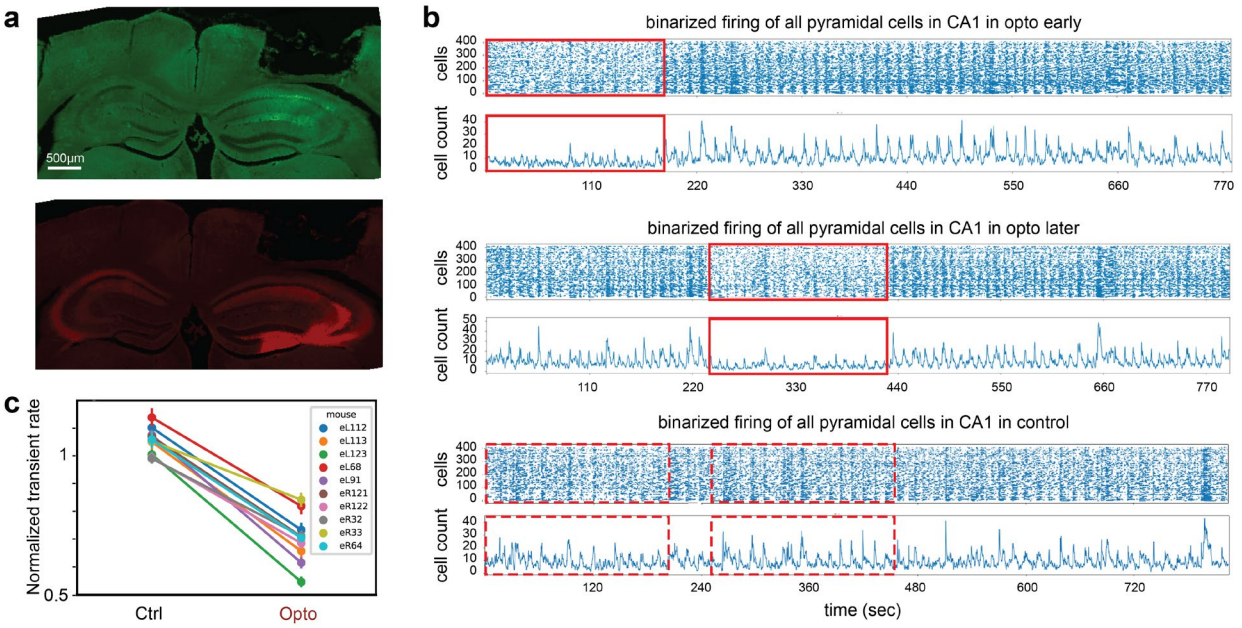

Supplementary Figure 2 (associated to Fig. 1).

Optogenetic inhibition of unilateral CA3 projections during 2P imaging of CA1

a. Representative example confocal image of a brain slice from one of the recorded Grik4-cre animal used for optogenetic experiments, showing GCaMP6f expression in right CA1 (top) and expression of cre-dependent opsin eOPN3 in CA3 and its projections to bilateral CA1 (bottom). Histology was performed on 7 of 10 animals.

b. Example activity of the same population of CA1 pyramidal cells during navigation through 3 different novel tracks. Rasters are binarized Ca^{2+} transient activity per 100ms. Below each raster is the number of active cells per 100ms. Solid red box: period of optogenetic stimulation of CA3 axons in CA1. Dashed red box: same number of frames in control condition, i.e. without optogenetic inhibition. Opto-inhibition occurred either from the start of the exploration of the new environment (top, "opto early") or in the middle of the session (middle, "opto later"). The control environment (bottom) was a different new environment with the LED off at all times.

c. Mean normalized neuronal activity (transient rate during period highlighted by red box divided by transient rate during the whole exploration of the environment) in control vs opto conditions ("opto early" and "opto later" combined), for each mouse. For all 10 animals, neuronal activity decreased during opto-inhibition. Error bars are 95% CI of mean across all cells of a given animal (eL112: n = 764 cells, eL113: n = 409, eL123: n = 771, eL68: n = 666, eL91: n = 946, eR121: n= 926, eR122: n= 1085, eR32: n = 1387, eR33: n= 829, eR64: n = 485)

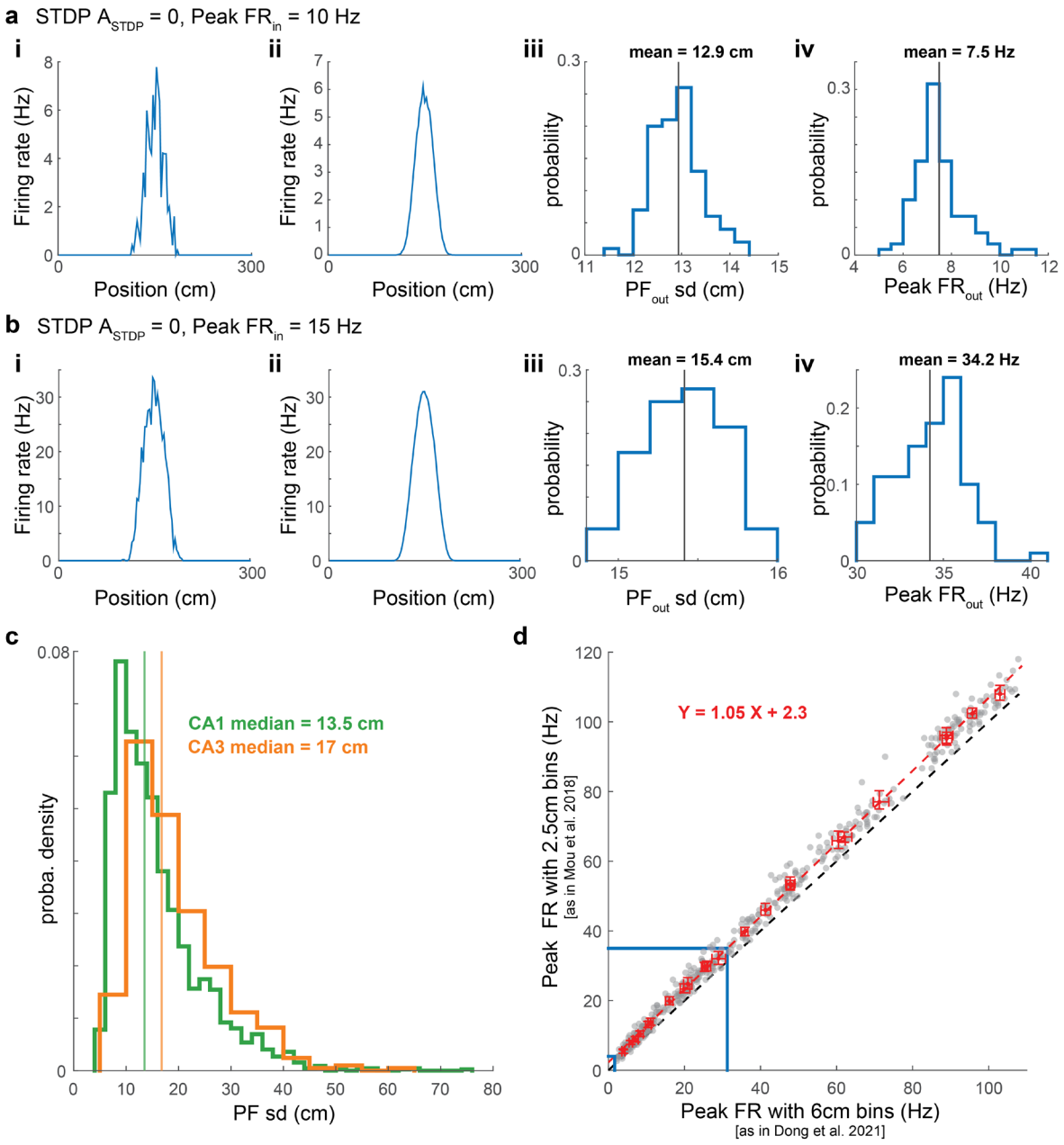

Supplementary Figure 3 (associated to Fig. 2).

Place Field width and output firing rates in simulated and recorded place cells

a-b. PF models without plasticity, for baseline parameters (A) and higher input rates (B) measured with 2.5 cm spatial bins (like in Mou et al. 2018, but unlike in the rest of the paper which uses 6 cm bins). **i:** Example output PF averaged over 30 laps, **ii**: mean output averaged over 100 simulated PFs, **iii**: distribution of output PF width (measured as the standard deviation, sd) for all 100 PFs (each a 30-lap average), **iv**: distribution of peak firing rate of the 100 PFs (30-lap average).
c. Distribution of PF width measured in CA1 and CA3 PFs reported in Dong et al. 2021 (same data as in Figure 1). This shows that our model's input PFs (PFin sd = 18 cm unless otherwise stated) and output PFs have realistic width (e.g. see panel **a**-**b**iii or Fig. S7b,f).
d. Peak firing rates of the 480 simulated PFs in Fig 2f2, using 6 cm spatial bins (as in Dong et al 2021, Fig 2 and the rest of this study) or 2.5 cm bins as in Mou et al. (2018) (errorbars: bootstrapped 95% CI of the mean for each set of input parameters). Data points are slightly above the identity line (dashed black) showing that using 6 cm bins slightly underestimates firing rates compared to Mou et al.'s methods. Solid blue lines mark the range of Peak Firing rates in data recorded in mice by Mou et al. (2018), and the estimated equivalent when using 6 cm bins based on a linear regression (dashed red). Output PFs in panels **a-b** and Fig. 2c fall in this range, but not PFs in Fig. 2d.

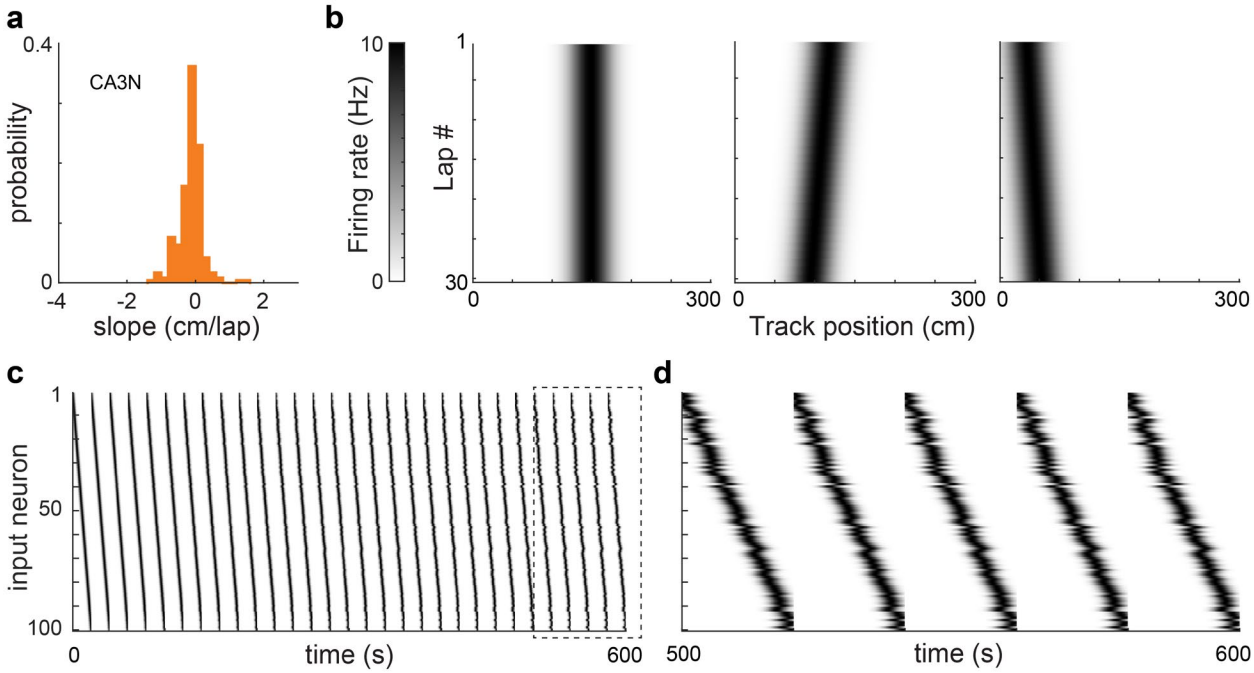

Supplementary Figure 4 (associated to Fig. 2).
Model of CA3-like dynamic input PFs

a. Probability distribution of the slope of the linear regression describing the COM shift for each PF recorded in CA3 during exploration of a novel environment (same data as in Fig 1b).

b. The lap-wise PFs of inputs to our output LIF neuron were designed to have a shifting slope randomly drawn from the distribution in panel a (different draw for each simulation). Shown are 3 examples of input PFs: stable on left, backward shifting in the middle (-0.8 cm/lap) and forward shifting on the right (0.6 cm/lap).

c. Input PFs during a full example 30-lap simulation.

d. Last 5 laps of the example in panel c (dashed box).

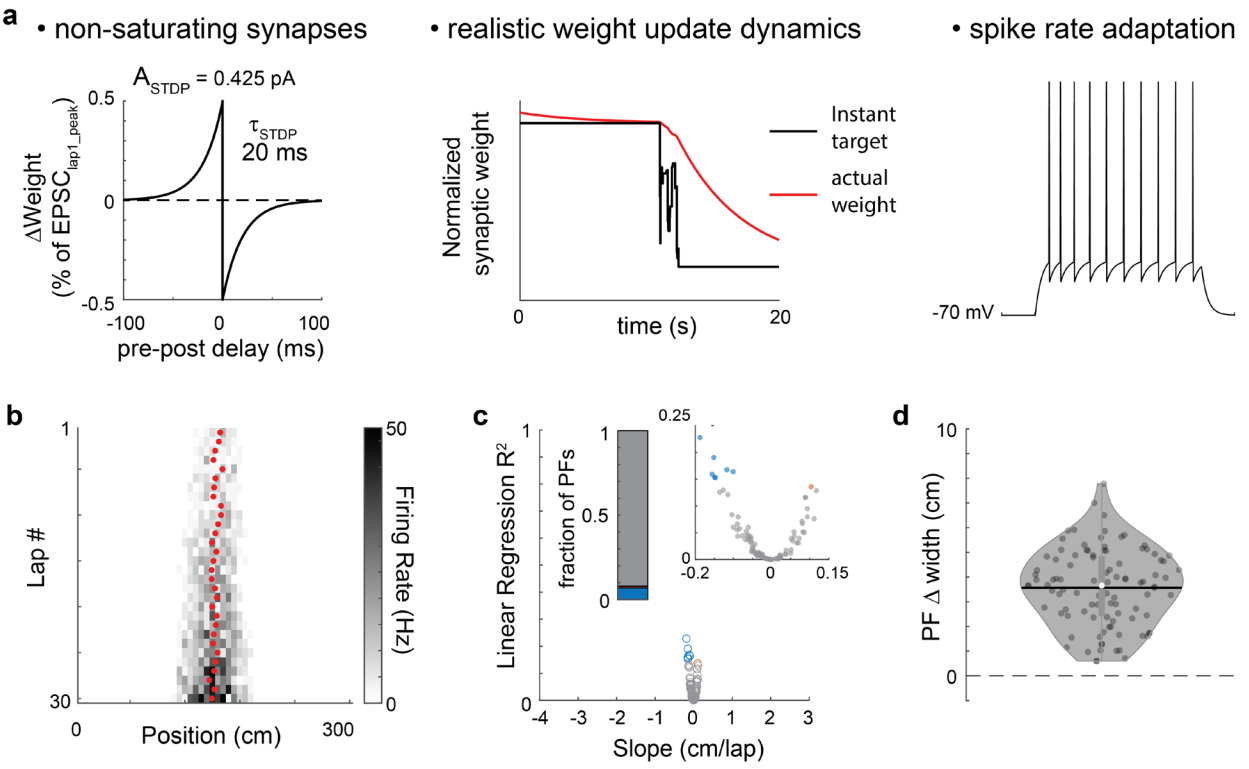

Supplementary Figure 5 (associated to Fig. 2).

More realistic weight update and output firing patterns do not increase PF backward shifting.

a. The model presented here used baseline parameters except that synaptic weights were allowed to grow without bounds (left: STDP rule), weight update was not instantaneous (middle: example synapse during a single lap) and spike-rate adaptation was added to the LIF output model (right: output neuron response to 500 ms current step of 180 pA). See methods.

b. Example simulated PF (not significantly shifting). Lap-wise PF center of mass shown as red dots.

c-d. 100 simulations with the same parameters.

c. Few PFs are significantly shifting and the shifts are weak. Left inset shows the proportion of PFs backward (blue), forward (red) or not significantly shifting (grey) (same as in Fig 1). Right inset is the same data zoomed in.

d. PF Δ width is computed as the difference of PF sd averaged on the first 3 laps with the PF sd averaged on the last 3 laps. As seen in panel b, PF width increases for all simulations.

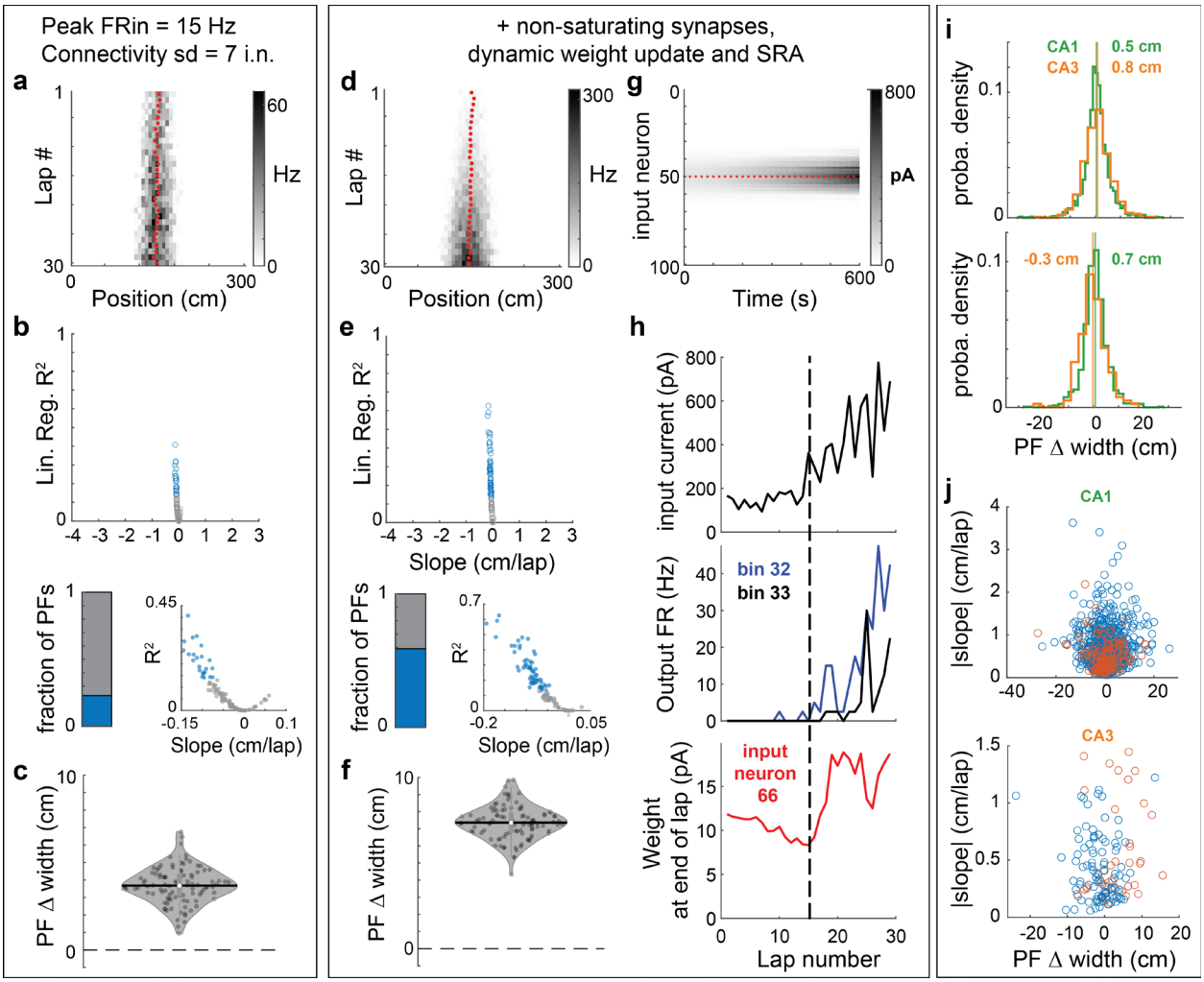

Supplementary Figure 6 (associated to Fig. 2).

STDP main effect is an unrealistic increase in output rates and PF width.

a. Example simulation with a model with baseline parameters except for a higher input rate (like in Fig 2d) and a narrower initial connectivity vector (this particular set of parameters was also tested in Fig 2f). The PF shows a small backward shift accompanied with an increase in output rates and PF width.

b-c. n = 100 simulated PFs with the same parameters as in A. Only ~20% of PFs show a significant but small backward shift, and no forward shift (**b**). However, all PFs display an increase in PF width (computed as the difference of PF sd averaged on the first 3 laps with the PF sd averaged on the last 3 laps). See Fig S5d for a similar result with different parameters but similar output firing rates.

d-h. Same model as in panels a-c except that, as in Fig S5, synaptic weights were allowed to grow without bounds, weight update was not instantaneous and spike-rate adaptation (SRA) was added to the LIF output model.

d-f. Same as a-c. Allowing runaway plasticity leads to an unrealistically large increase in output firing rates (**d**), which yields consistent backward shifting of small amplitude (**e**) and a large increase in PF width (**f**). (n = 100 simulated PFs)

g. Evolution of the synaptic weight of all 100 input neurons during the 30-lap example simulation in D, illustrating the runaway dynamics (red plus-signs mark the start of a new lap; input 50 correspond to the initial peak weight). Note that the increase in weights is bilateral and happens from inside-out. The COM backward shift is small because weights of inputs > #50 (i.e. with COM in front of the PF center of mass) also increase, albeit slightly slower than inputs < #50.

h. The bilateral increase in PF width is due to an inside-out increase in output rates and synaptic weights (same example simulation as in d and g). ***Top***: For each lap, the total input current to the LIF output neuron was averaged over 50 ms preceding the first spike of input neuron #66, which has its PF COM located in bin 33 (the output PF COM being around bin 25). This current corresponds to the sum of inputs < #66 producing the front edge of the output PF. It starts to increase before input 66 weight potentiates (dashed line). ***Middle***: Output firing rate in bin 33 (black) and 32 (blue): note that FR starts to increase in bin 32 (closer to the center) before it does in bin 33, and before input 66 weights start to

increase. ***Bottom***: Input 66 synaptic weight depresses first but starts to increase (dashed line) after the output PF has enlarged sufficiently (due to the increased rate in the middle of the PF) to produce output spikes after input 66 spikes. As suggested by past studies, the weights on the forward edge initially tend to depress due to the unidirectional movement and the absence of output firing (thus participating in backward shifting) but STDP makes the output rate increase in the center of the PF, which leads to a higher probability of potentiating input-output spike pairs on the edges.
i-j. Change in width for PFs recorded in CA1 and CA3 (same data and color codes as in Fig. 1). The distribution is centered around 0, in contrast to models above (**I**: top histogram includes all PFs, bottom only the significantly shifting ones. Vertical lines and associated values are medians). Moreover, PF width changes are not correlated with the shifting speed (**j**: only includes significantly shifting PFs, blue for backward, red for forward).

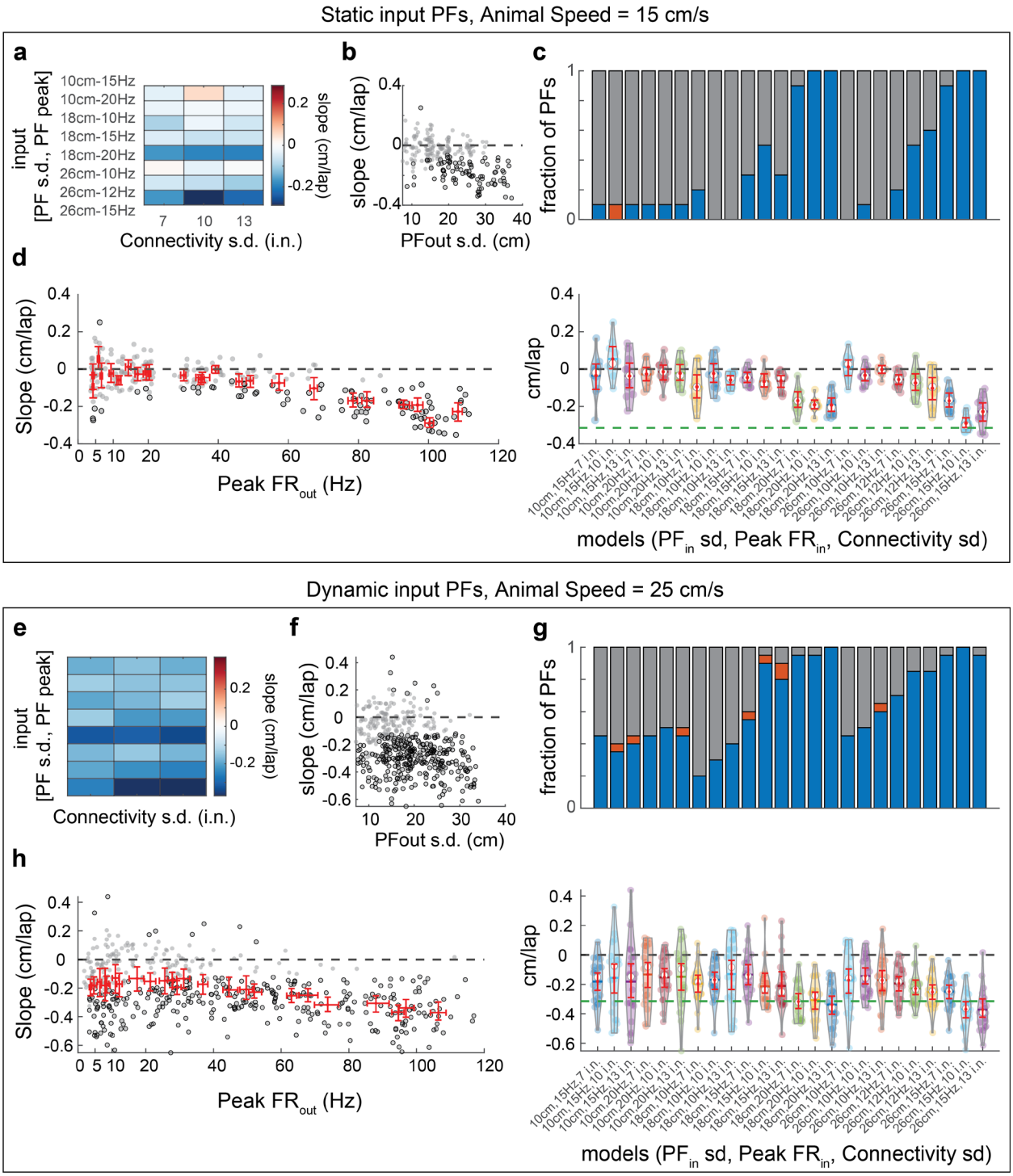

Supplementary Figure 7 (associated to Fig. 2).
Exploration of the parameter space: inputs and animal speed

a-d. Same data as in Fig 2f (480 simulated PFs).

a. Parameters controlling the input rates and width of the initial connectivity vector are systematically varied to explore a wide range (realistic and unrealistic) of output firing rates. For each parameter set, n = 20 PFs are simulated. The matrix shows for each parameter set the mean COM shifting slope estimated from linear regression (represented as red dots in Fig 2f and panel d here).

b. Shifting slope as a function of output PF width (averaged over the 30 laps). Widths are in a realistic range (see Fig S3c), with an expected correlation with the slope (significantly shifting PFs artefactually leading to a wider average width).
c. Proportion of backward (blue), forward (red) and non-significantly shifting PFs for each set of parameters (Top). The corresponding slope distributions and bootstrapped mean and 95% CI (red) are shown in the bottom panel. The green dashed line marks the mean shifting slope from PFs recorded in CA1 in a novel environment.
d. Same plot as right panel in Fig 2f. Red error bars: means for each condition, with bootstrapped 95% CI in the x and y-axes.
e-h. Same as a-d but with models including dynamic inputs mimicking PFs recorded in CA3N (see Fig S4) and with a higher but realistic mouse speed (higher speed promotes backward shifting, because input spikes from farther away can fall in the potentiating time window). Consistent but modest backward shifting (mostly inherited from CA3-like inputs) is seen for all conditions. Some parameter sets yield proportions of backward and forward shifts similar to CA1N but are associated to a mean shift smaller than in real CA1N conditions. Other sets of parameters can yield a mean COM shift similar to CA1N but only because there is a much higher proportion of weakly backward shifting PFs. Moreover, they correspond to unrealistic output firing rates. Overall, no model matched the CA1N dataset well.

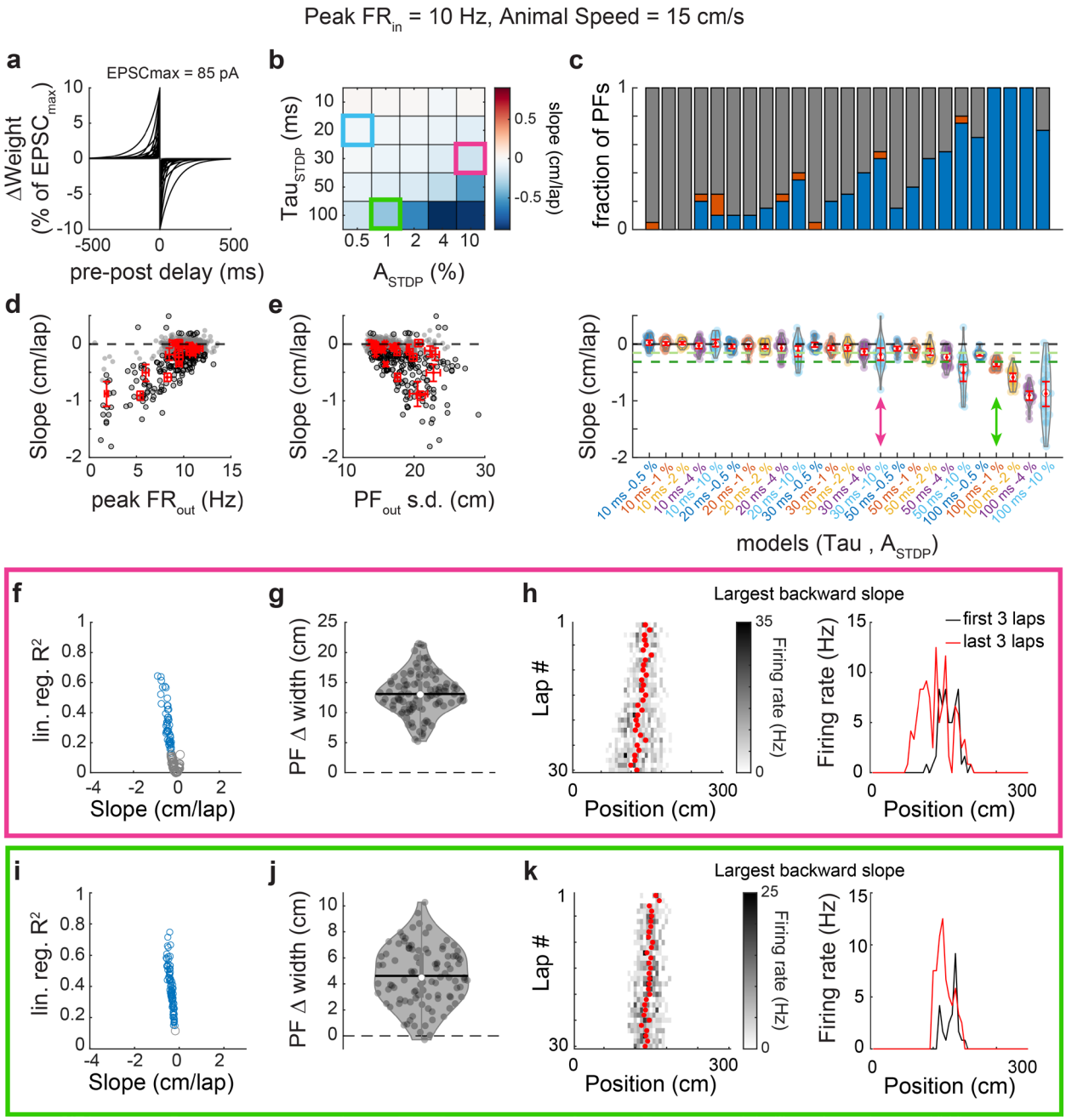

Supplementary Figure 8 (associated to Fig. 2).

Exploration of the parameter space: anti-symmetric STDP rules

a. Different antisymmetric STDP rules were tested, each with a specific time constant Tau (from 10 to 100 ms) and maximum weight change A_{STDP} (0.5%-10% of EPSCmax, i.e. 0.425-8.5 pA). All other parameters were kept as in the baseline model. Note that Tau > 30 ms and A_{STDP} > 2% (i.e. 1.7 pA here) are far from classic STDP rules.

b. Mean shift (average across n = 20 simulated PFs) as a function of the STDP parameters. The light blue square corresponds to our baseline parameter set (model 1 in Fig 2). The pink and green squares highlight 2 sets of parameters that lead to a mean shift similar to CA1F or CA1N, respectively (see panel C bottom).

c. *Top*: Proportion of backward (blue), forward (red) and non-significantly shifting PFs for each set of parameters. *Bottom:* The corresponding slope distributions and bootstrapped mean and 95% CI (red). The light and dark green dashed lines mark the mean shifting slope from PFs recorded in CA1F and CA1N, respectively. Pink and green arrows point to the parameter sets highlighted in B, that match the mean shift observed in CA1 (F or N): these correspond to unrealistic A_{STDP} or Tau, respectively, and do not match the range of slopes observed in CA1.

d-e. Shifts of all simulated PFs (n = 500) as a function of their average peak output firing rate (**d**) or average width (**e**). Note that large shifts correspond here to a decrease in output firing rates and large PFs (in other words, the PF is diluting away). The low rates and disappearance of the PF are driving the higher variance observed in the most extreme parameter sets. Red error bars: means for each condition, with bootstrapped 95% CI in the x and y-axes.
f-h. n = 100 simulations using the same parameters set highlighted in pink in panels b and c(i.e. that matches the mean shift observed in CA1F). **F.** No forward shift is observed. The range of slope values does not match CA1F. **g.** STDP leads to an unrealistic increase in PF width (see Fig. S6i for physiological range). **h.** Example PF with the largest backward slope in panel f.
i-j. n = 100 simulated PFs using the same parameters set highlighted in green in panels b and c (i.e. that matches the mean shift observed in CA1N). Here again, the range of slopes, the proportion of backward and forward shifting and the consistent PF enlargement do not match what we observed in CA1N.

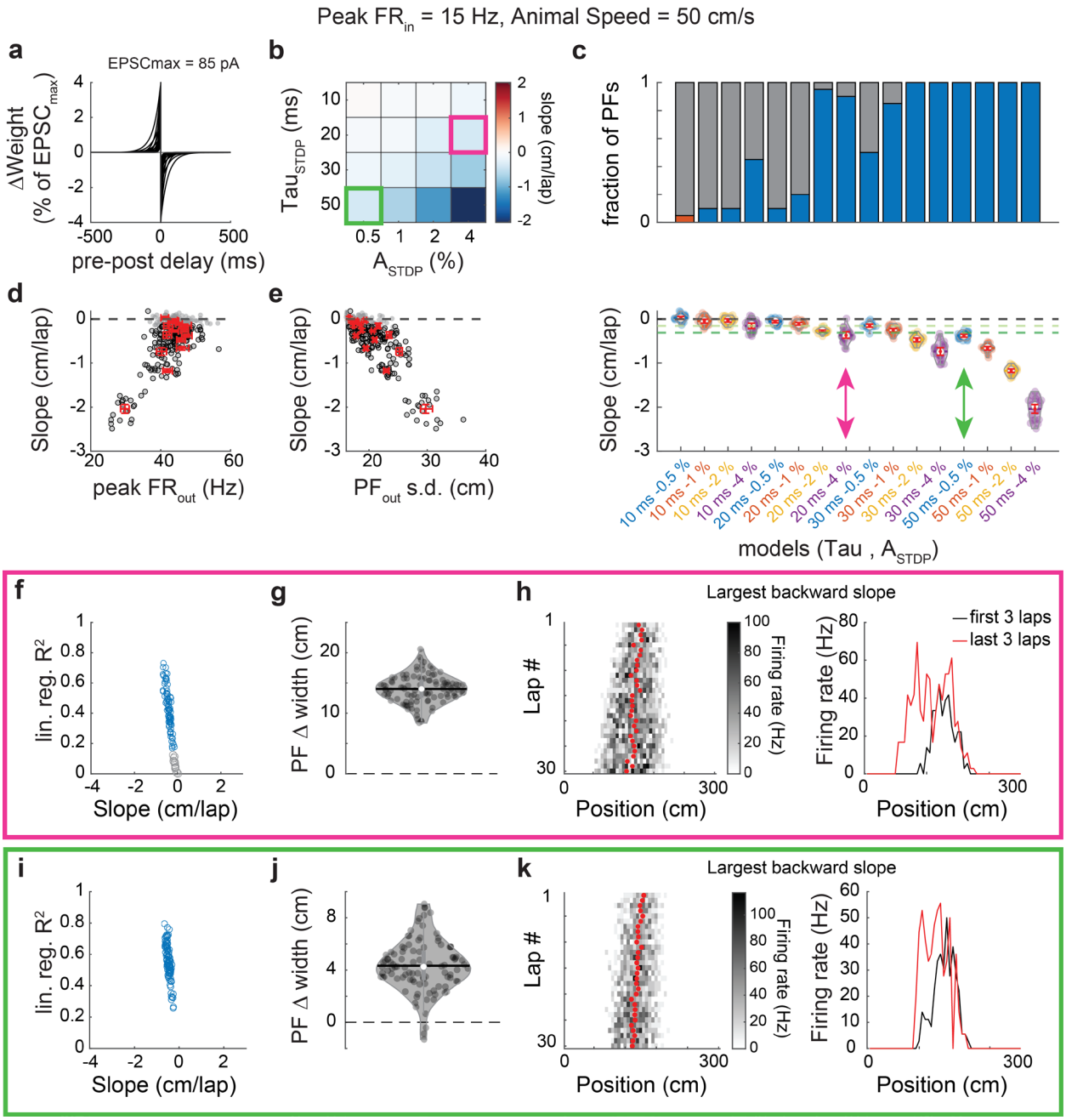

Supplementary Figure 9 (associated to Fig. 2).

Exploration of the parameter space: anti-symmetric STDP rules at high input rates and high speed

Same as Fig. S8 but with 15 Hz Peak FR_{in} and a virtual animal speed of 50 cm/s (which is unrealistically high for a mouse, but matches the speed used in the model of Mehta et al. (2000), which was inspired by observations in rats). Increasing these parameters promotes the effects of STDP.

a-e. Systematic variation of Tau and A_{STDP} (n = 20 simulations per condition). Note that Mehta and Wilson's model used Tau = 10 ms and A_{STDP} = 0.6 pA (which would correspond to ~0.7% of our EPSCmax). Conditions that match the mean shift observed in CA1N are highlighted in pink and green. They exhibit a high proportion of backward shifting PFs unlike what we observed in CA1 and they correspond to unrealistic STDP parameters (high amplitude or high Tau). Backward shifts as large as what we observed in some CA1 PFs (e.g. < - 1 cm/lap, which is not that uncommon, see Fig 1 and 2e) can only be achieved with unrealistically high STDP parameters.

f-k. n = 100 simulations for each of the parameter sets highlighted in pink (f-h) or green (i-k). The range of slopes, the proportion of backward and forward shifting and the consistent PF enlargement do not match what we observed in CA1.

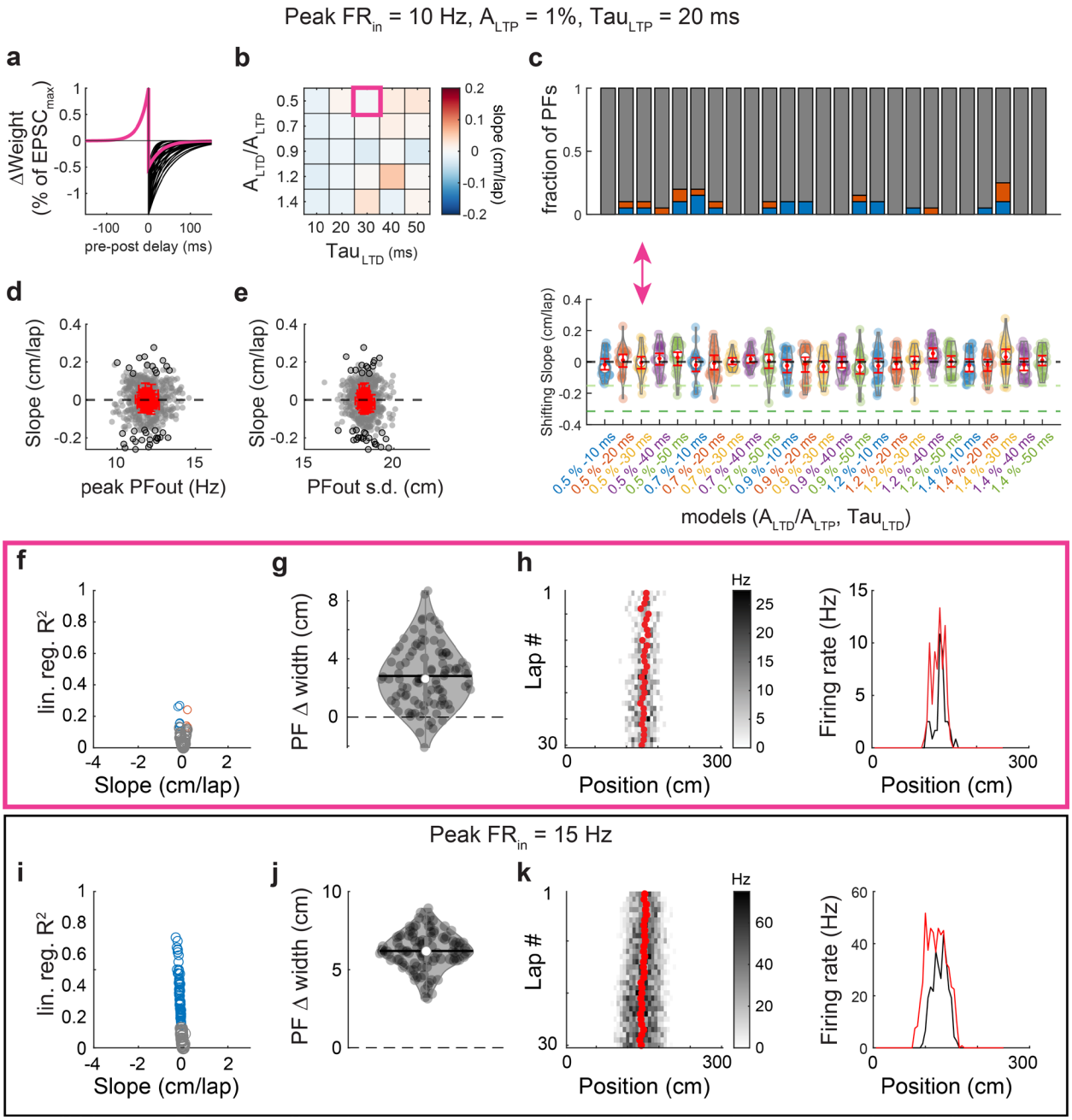

Supplementary Figure 10 (associated to Fig. 2).

Exploration of the parameter space: asymmetric STDP rules

a-e. Systematic variation of the postsynaptic time constant τ_{LTD} and the ratio of amplitudes A_{LTD}/A_{LTP}, such that the amplitude and decay of the LTD variable were varied while the LTP parameters were kept fixed (n = 20 simulations per condition). The pink trace in panel **a** (also highlighted in **b** and **c**) corresponds to the STDP rule reported by Bi and Poo (1998) from cultured CA1 pyramidal cells. No condition led to much shifting. Panels **d** and **e** show that output firing rates and PF width were realistic and did not vary much.

f-k. n = 100 simulations for the STDP rule highlighted in a (pink). Panels **f-h** correspond to 10Hz inputs (as in b-e) whereas panels **i-k** correspond to 15Hz inputs, leading to high output firing rates. The range of slopes, the proportion of backward and forward shifting and the consistent PF enlargement do not match what we observed in CA1.

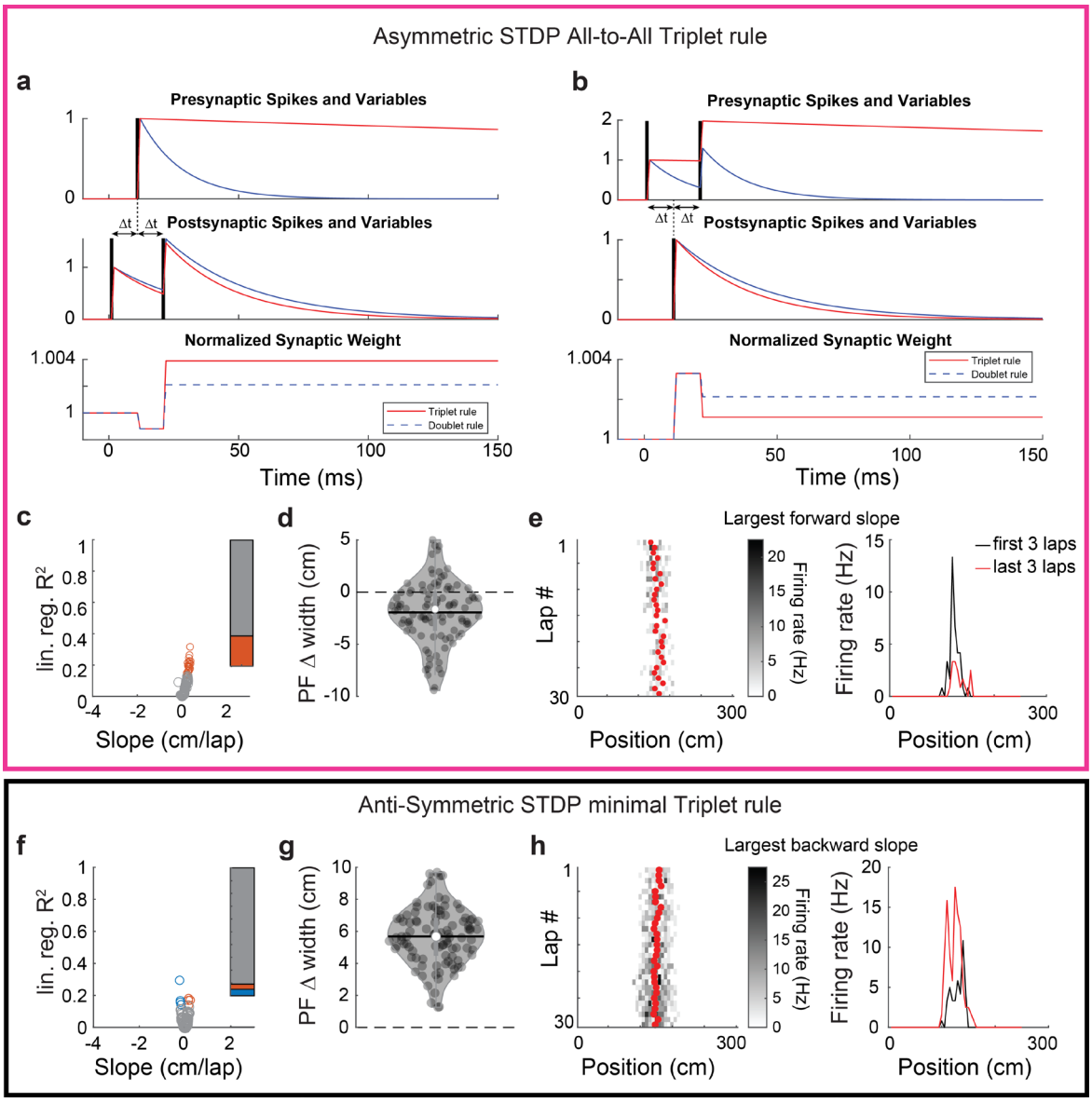

Supplementary Figure 11 (associated to Fig. 2). Effects of STDP triplet rules on PF shifting

a-e. Implementation of the All-to-All triplet model designed by Pfister and Gerstner (2006) and fitted to hippocampal data from Wang et al (2005) and Bi and Poo (1998). Parameters: $A_{2}+ = 0.61\%$, $A_{2}- = 0.16\%$, $A_{3}- = 0.14\%$, $A_{3}+ = 0.67\%$, $\tau_{2}+ = 16.8ms$, $\tau_{2}- = 33.7ms$, $\tau_{3}+ = 27ms$, $\tau_{3}- = 946ms$. Subscript 2 denotes doublet variables parameters, whereas subscript 3 denotes triplet variables parameters. + and – denote variables associated to potentiation or depression, respectively. A doublet rule based on these values of $\tau_{2}+$ and $\tau_{2}-$ correspond to a classic asymmetric STDP rule with similar time constants as the pink trace in Fig S10a.

a-b. Post-Pre-Post (A) and Pre-Post-Pre triplet STDP protocols (B): input and output spikes in black, $\Delta t = 10ms$. Doublet STDP variables in blue and additional triplet variables in red. A classic doublet STDP rule yields the same weight change regardless of the protocol, whereas the triplet rule accounts for the asymmetry reported in past experimental studies.

c-d. n = 100 simulations of 30-lap place fields with the asymmetric triplet rule (the rest of the parameters are as in Fig 1c)

c. Only non-significant and forward shifting PFs are observed, and shifting speeds are unrealistically small. **d.** The triplet rule by itself occasionally leads to an unrealistic decrease in PF width (due to a decrease in firing rates). **e.** Example PF with the largest forward slope in C.

f-h. Same as C-D but with the triplet rule used by Zenke et al. (2015): $A_{2}+ = A_{3}+ = A_{2}- = 0.5\%$, $A_{3}- = 0$, $\tau_{2}+ = \tau_{2}- = 20ms$, $\tau_{3}+ = 100ms$. **f.** The amplitudes and proportions of forward and backward shifts are much smaller than in our CA1 data. **g.** This symmetric triplet rule leads to an increase in PF width. **h.** Example PF with the largest backward slope in panel f.

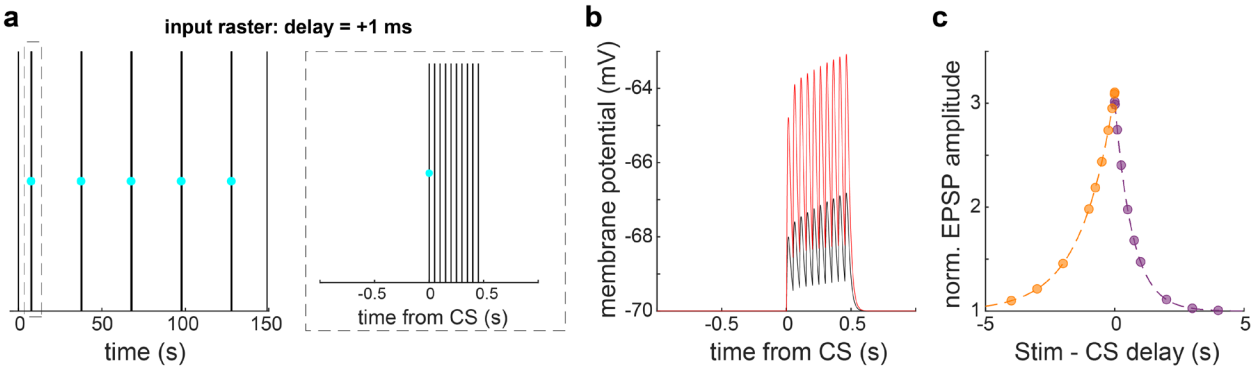

Supplementary Figure 12 (associated to Fig 3). Optimization of our BTSP model to match findings from Bittner et al. 2017

We performed simulations mimicking the experiments done in slices reported in Bittner et al. 2017 (their Figure 3). Our model here consists of the same leaky-integrate-and-fire neuron as elsewhere in our study, but with a single input with initial synaptic weight of 77 pA. This weight yields a 2 mV EPSP when the input fires a spike, which matches the average baseline stimulation-induced EPSP in Bittner et al 2017. BTSP was implemented as a pure potentiation rule (see Fig 3a) without synaptic normalization (weights were not bounded either), using the time constants estimated by Bittner et al. 2017 (1.31 s for the Pre-before-Post kernel, 0.69 s for the Post-before-Pre kernel).

a. The protocol consisted of 5 pairings of a BTSP-triggering complex spike (CS, cyan dot, modeling induction of a plateau in our LIF neuron) with an input spike-train of 10 regularly-spaced spikes at 20 Hz (black vertical lines). The delay between the CS and the beginning of the input train (Stim) was varied from -4 s to 4 s. For a given delay condition, there was an inter-pairing-interval of 30 s. To evaluate changes in EPSP amplitude due to BTSP, single spikes were added 7.5 s before the first CS and 21.5 s after the last CS. Panel a *left* shows an example protocol for the shortest delay (1 ms). The inset on the right shows the first pairing (zoom of the dashed rectangle on the left).

b-c. Two parameters were optimized to fit Bittner et al. 2017's results: maximum potentiation = 3.8 pA, scaling factor b = 1.1. The scaling factor value of 1.1 was kept for all BTSP models throughout the study. The 3.8 pA spike-wise maximum potentiation A_{BTSP} fits the in vitro experiments modeled here, but was not kept in models of place cells used elsewhere because the Bittner in vitro experiments were done in conditions with only one input active (i.e. no place field connectivity) and the initial synaptic weights of the stimulated inputs were relatively homogeneous (producing EPSPs ~ 2 mV). The Bittner dataset thus does not allow to determine the effective maximum weight change that would occur in vivo.

b. EPSPs during the first (black) and last (red) pairing for the protocol in panel a, illustrating the potentiating effect of BTSP with the parameters stated above.

c. Dashed lines correspond to the BTSP rule determined by Bittner et al. 2017 from their slice experiments. Data points correspond to our simulations (the final EPSP amplitude was normalized to the initial EPSP amplitude, as in Bittner et al. 2017). Compare to Figure 3D in Bittner et al. 2017.

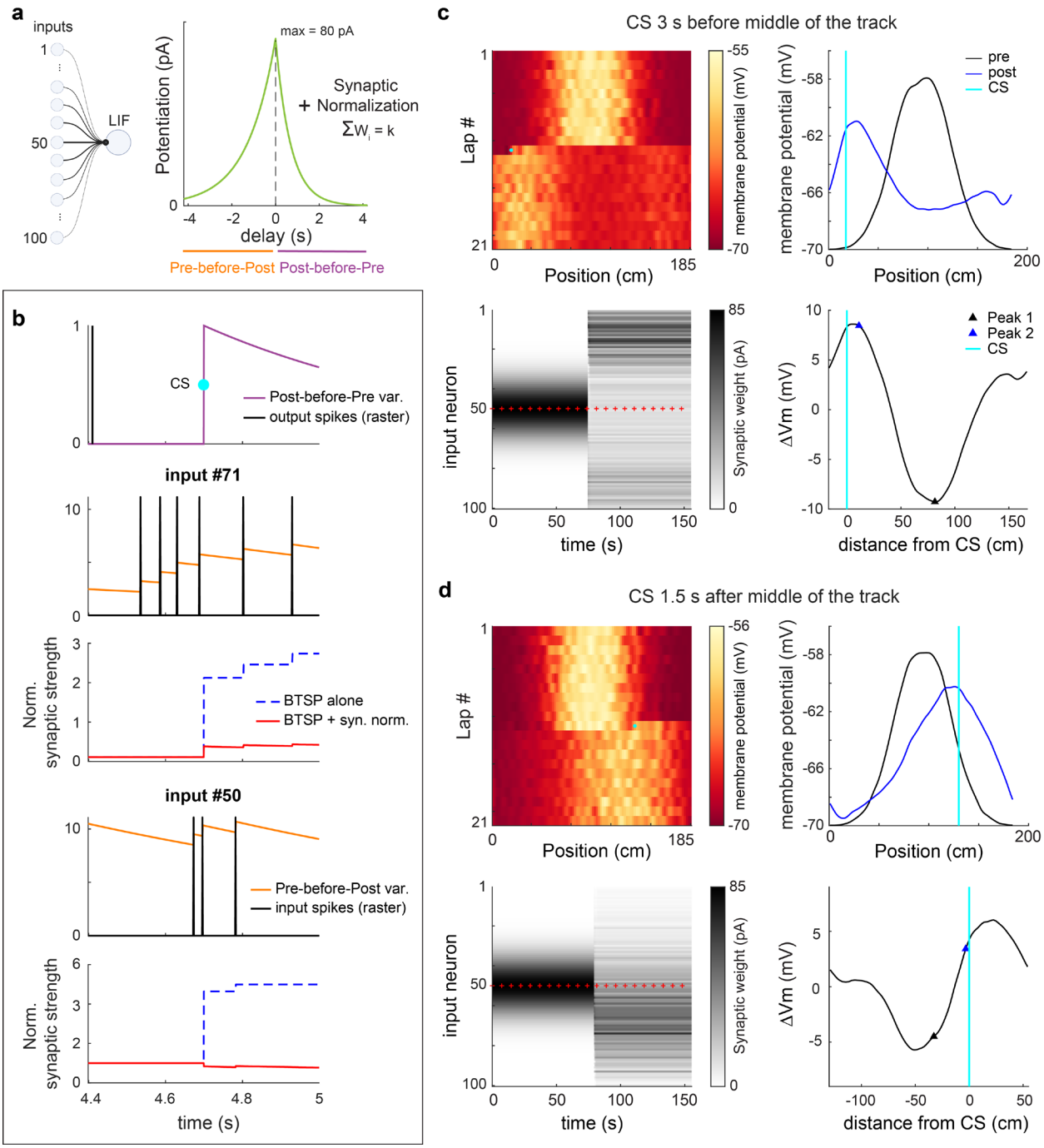

Supplementary Figure 13 (associated to Fig. 3)

Simulations of experiments as in Milstein et al. 2021: Effect of a single BTSP-triggering event on the pre-existing PF of our place cell model

a. Same place-cell model as in Fig 2, based on 100 spatially modulated input Poisson processes (with stable PFs) to a single leaky-integrate-and-fire (LIF) neuron. Plasticity was implemented following the potentiation kernel discovered by Bittner et al. 2017 (as in Fig S12) combined with a homeostatic synaptic normalization rule maintaining the sum of weights constant. In the examples shown in this figure, the maximum potentiation of the BTSP rule (i.e. before synaptic normalization) was set at 80 pA.

b. Plasticity variables (purple and orange traces) and synaptic weight dynamics (dashed blue and solid red traces) around the time of a complex spike (CS, cyan dot) triggering BTSP, for input 71 (which has a PF close to where the CS occurred) and input 50 (i.e. with PF in the middle of track and maximum initial synaptic weight). Potentiation following the rule in

panel a occurs at the time of CS based on the value of the pre-before-post variable for each synapse (orange), and it also occurs when an input spike coincides with a non-zero value of the post-before-pre variable started by the CS (purple). Normalized synaptic strength is the synaptic weight in pA divided by the maximum synaptic weight of the simulation (85pA – this is not a hard bound here but a consequence of maintaining the sum of weights constant). This example comes from lap 11 in panel d.

c-d. Simulations of experiments as in Milstein et al. 2021. Activity in our place cell model is simulated for a virtual animal running 21 laps on 185 cm linear track at a constant speed of 25 cm/s. A CS (cyan dot, BTSP-triggering event) is triggered 3s before the virtual animal reaches the middle of the track (**c**) or 1.5s after (**d**). *NorthWest*: lapwise membrane potential dynamics (Vm was averaged for each 100 spatial bin). The CS (cyan dot) causes a shift of the spatially modulated Vm. *SouthWest*: Synaptic weight dynamics for all inputs. Red plus-signs mark the start of a new lap. *NorthEast*: Smoothed Vm average for the 10 laps before or after CS. Compare to Figure 1C and S2 in Milstein et al. 2021. *SouthEast*: Difference between the pre-CS and post-CS averages. As in Milstein et al. 2021's Supplementary Figure 2A and network model optimization procedure, a CS occurring 3s before the middle of the track (i.e. PF center of mass of the input neuron with initial peak synaptic weight) causes a maximum increase in Vm of ~8mV (**c**).

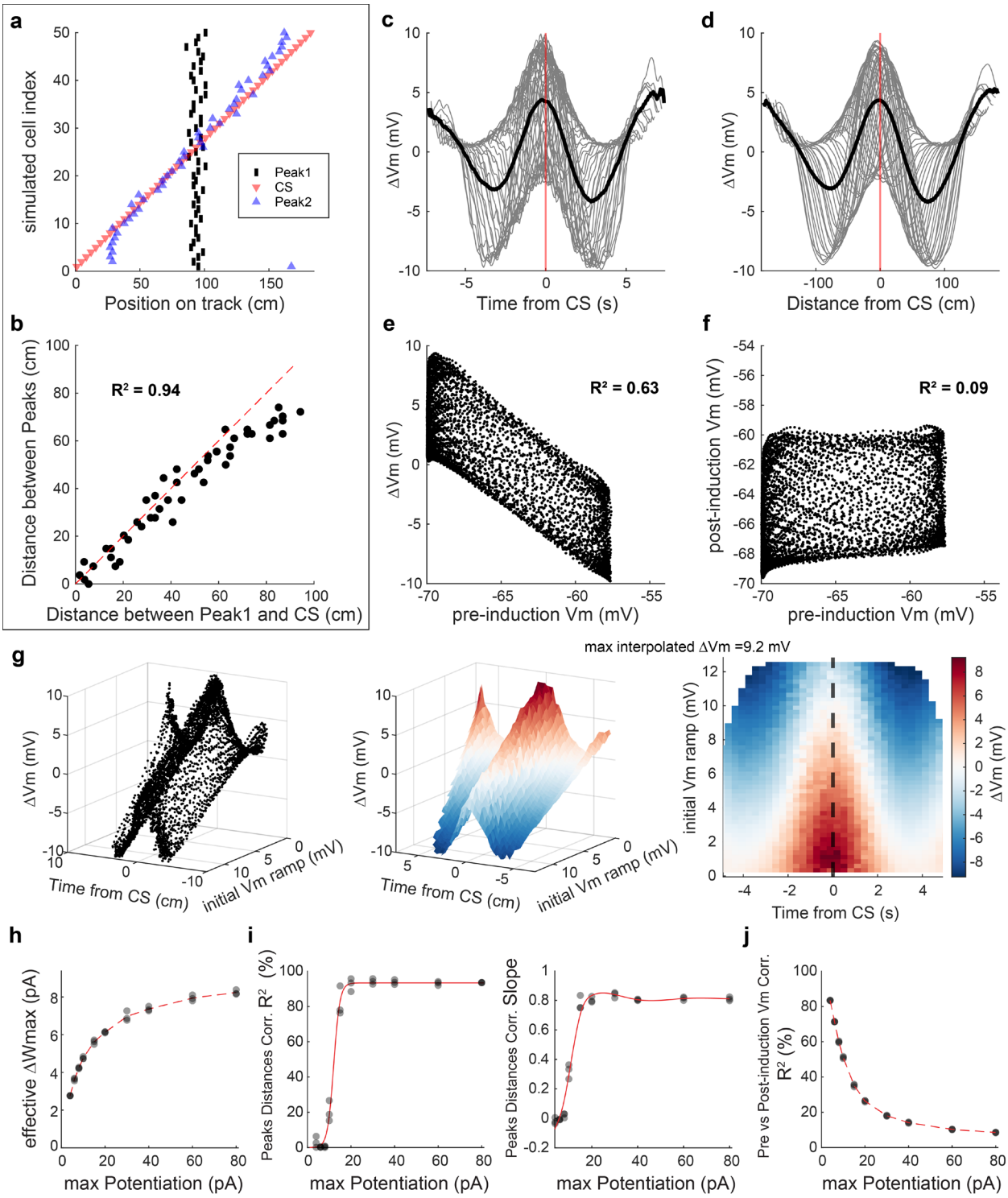

Supplementary Figure 14 (associated to Fig 3)

A combination of BTSP and synaptic normalization yields an emergent weight-dependent bidirectional plasticity rule and accounts for PF shifts observed in Milstein et al. 2021.

a. 50 Milstein-type inductions were simulated as in Fig S13, varying the time of CS systematically to span the whole track (185 cm of length, with animal speed of 25 cm/s as in Milstein et al. 2021, and a maximum potentiation of 80 pA before synaptic normalization). Compare to Figure 1D in Milstein et al. 2021 article.

b. The distance between Peak1 and Peak2 vs. the distance between the CS and Peak1 are correlated ($p < 0.0001$ computed by Pearson's correlation). Red dashed line is unity, not the regression line. Compare to Figure 1E in Milstein et al. 2021: the PF shifts observed are similar, especially when the CS occurs close enough to Peak1 (which is always the case in our simulations in Fig 3 because, by design, CSs always occur in-field).
c-d. Temporal and spatial profiles of CS-induced changes in membrane potential Vm (ΔVm). Grey lines are individual simulations (as in Fig S13c-d South-East) aligned on the CS time or position (red line), the black line is the average of all 50 simulated cells. The spatial profile (panel d) is computed from spatially binned and smoothed Vm as in Fig S13c-d North-East. Compare to Figure 2 in Milstein et al. 2021 (note that the x-axes cover a wider range in our case, and that ΔVm beyond 5s away from the CS are not well sampled in the Milstein dataset).
e. Changes in Vm are negatively correlated to initial Vm (5000 points, from all 50 simulations in panel a, using binned and smoothed Vm values as in panel d). Compare to Figure 3G in Milstein et al. 2021.
f. When the maximum potentiation parameter is high enough (here 80 pA), the correlation between pre and post-CS Vm is poor (low R^2). 5000 points from all 50 simulations using binned and smoothed Vm values. Compare to Figure 3H in Milstein et al. 2021.
g. Changes in Vm ramp (ΔVm) as a function of both time and initial Vm ramp from baseline (a proxy for initial synaptic weight in Milstein et al. 2021. Indeed, in our model, initial Vm is simply a noisy reflection of initial synaptic weights). *Left*: Same data as in panel c. *Middle*: Linear interpolation of the data on the left. *Right*: Heatmap of the interpolation, restricted to the range of 'time from CS' in Figure 3I of Milstein et al. 2021. The white band (ΔVm = 0) corresponds to equilibrium, i.e. the target synaptic weight when BTSP is triggered. This analysis shows that our model of BTSP as pure potentiation combined with an additional homeostatic synaptic normalization rule results in an apparent weight-dependent bidirectional plasticity rule like what was suggested in Milstein et al. 2021's Figure 5C.
h-j. Varying the maximum potentiation parameter of the BTSP rule affects the fit of the model to Milstein et al. 2021's experimental findings. For each value of the maximum potentiation parameter, we simulated 3 experiments (grey dots) like in panel a (each experiment including 25 simulated inductions, with CSs positions spanning the length of the track).
h. The effective maximum weight change (Effective ΔWmax) of the combined BTSP + synaptic normalization model is a non-linearly increasing function of the maximum potentiation parameter of the BTSP rule. A potentiation parameter of 80 pA as chosen in panels a-g corresponds to an effective ΔWmax of ~8 pA, similar to the effective ΔWmax for the parameters that we used in our main in silico experiments in Fig 3. Effective ΔWmax was computed as the maximum weight change in all simulations for a given set of parameters divided by the value of the Pre-before-Post plasticity variable of the given input cell at the time of maximum weight change. Effective ΔWmax is thus an estimate of the maximum weight change for a single input spike, excluding temporal summation, and is comparable to the maximum potentiation parameter of a bidirectional plasticity rule (such as the STDP rule in Fig 2, or Milstein et al. 2021's Figure 5C). However, note that because our model is not designed as a bidirectional plasticity rule but includes a heterosynaptic homeostatic rule, there is no true ΔWmax and the estimate will vary from simulation to simulation. This is because, in our model, weight changes are not only dependent on initial weight but also on the instantaneous sum of weights, and thus on the stochastic activity from all input cells.
i. Effect of the maximum potentiation parameter on CS-induced PF shifts characterized as in panel B. Both the strength of the correlation between the CS position and the PF shift (R^2, *left*) and the slope of the regression (*right*) reach a plateau at ~20pA, where PF shifts qualitatively fit the Milstein dataset.
j. Effect of the maximum potentiation parameter on the strength of the correlation between the pre and post-CS membrane potential, computed as in panel F. This correlation becomes low like in Milstein et al. 2021 for high values of the parameter, such as the 80 pA chosen for panels a-g.

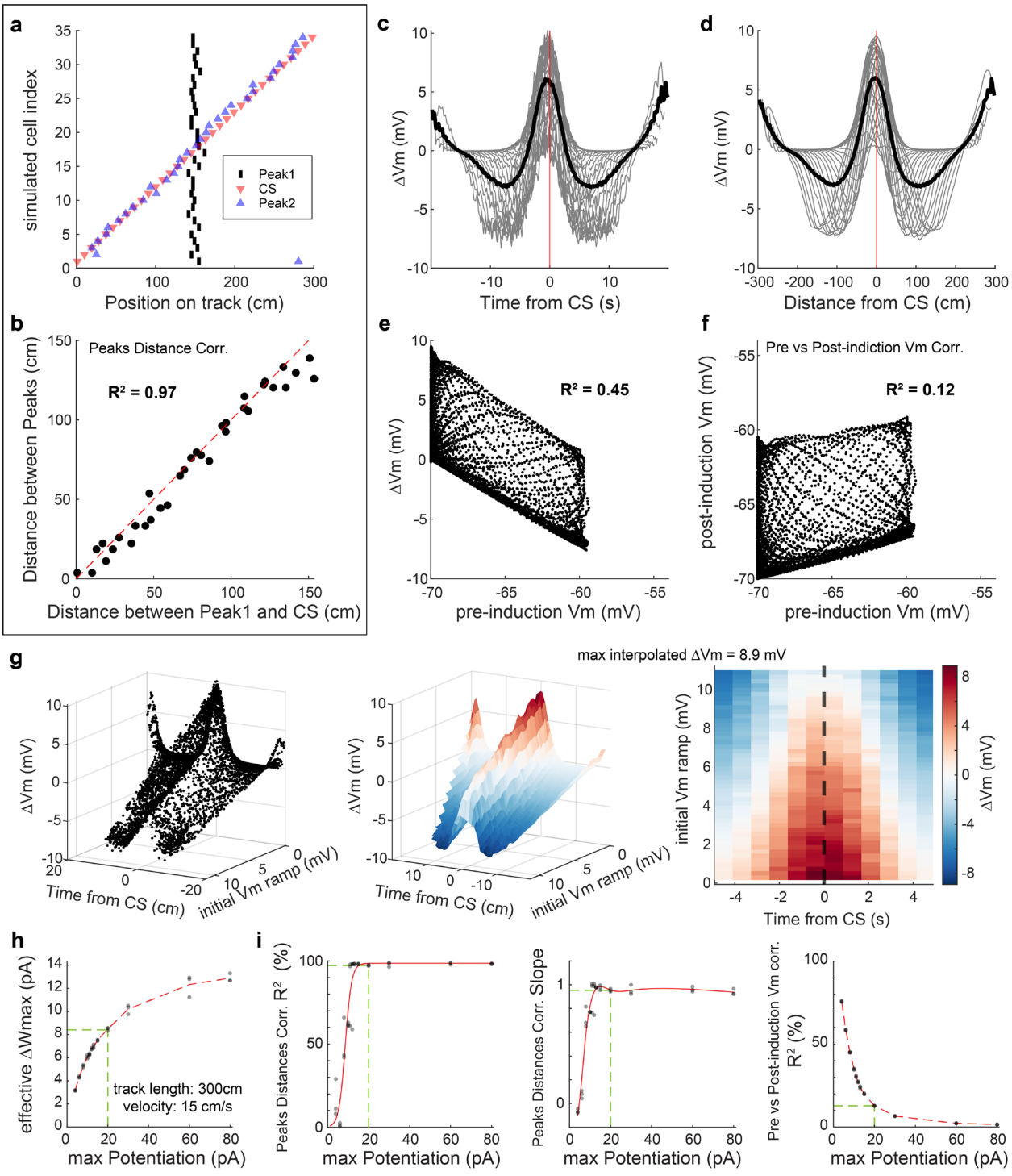

Supplementary Figure 15. (associated to Fig 3.)
Characterization of CS-induced PF shifts and emergent weight-dependence of the model used in Figure 3

a-g. Same as in Fig. S14 but for the parameters used in our main in silico experiments shown in Figure 3d-j, i.e. matching Dong et al. 2021's experimental conditions (track length = 300 cm, animal speed = 15 cm/s) and a maximum potentiation of the BTSP rule = 20 pA. The analysis was based on the simulation of 35 Milstein-type inductions for which the CS location was varied systematically to span the whole track.

a-b. PF shifts are well correlated with the CS location relative to the initial place field, close to the identity line. Even though we don't have a ground truth for these parameters, we took this as the main indicator that our model is consistent with Milstein et al. 2021 experimental findings and can be applied to study the effects of BTSP on PF shifting dynamics.
c-d. Temporal and spatial profiles of Vm changes, centered on the CS. Note that the x-axes are wider than in Fig. S10 because the track is longer and the animal speed smaller.
e. The correlation between the Vm changes and pre-induction Vm (a proxy for initial synaptic weights) is as strong as in Milstein et al. 2021.
f. The correlation strength between pre and post-induction Vm is low, as in Milstein et al. 2021.
g. The combination of BTSP and synaptic normalization, with the parameters used in Figure 3, results in an apparent weight-dependent bidirectional plasticity rule akin to the one proposed in Milstein et al. 2021. Note that it is slightly different from what we showed in Fig S14g as it is defined over a wider range of times relative to CS.
h-i. To determine a plausible maximum potentiation parameter for the BTSP rule, we tested different amplitudes (shown in Fig 3a) as in Fig S14h-j.
h. Effective maximum weight change resulting from the combination of homeostatic plasticity and each potentiation rule in panel a. Estimated as in Fig S14h. The green dashed line corresponds to the selected optimum (green kernel in Fig 3a).
i. Optimization of the BTSP maximum potentiation parameter to fit Milstein et al. (2021)'s experimental findings. The green dashed line indicates the optimal BTSP amplitude (minimal parameter value that maximizes the first 2 indicators and for which the third indicator is optimally low).

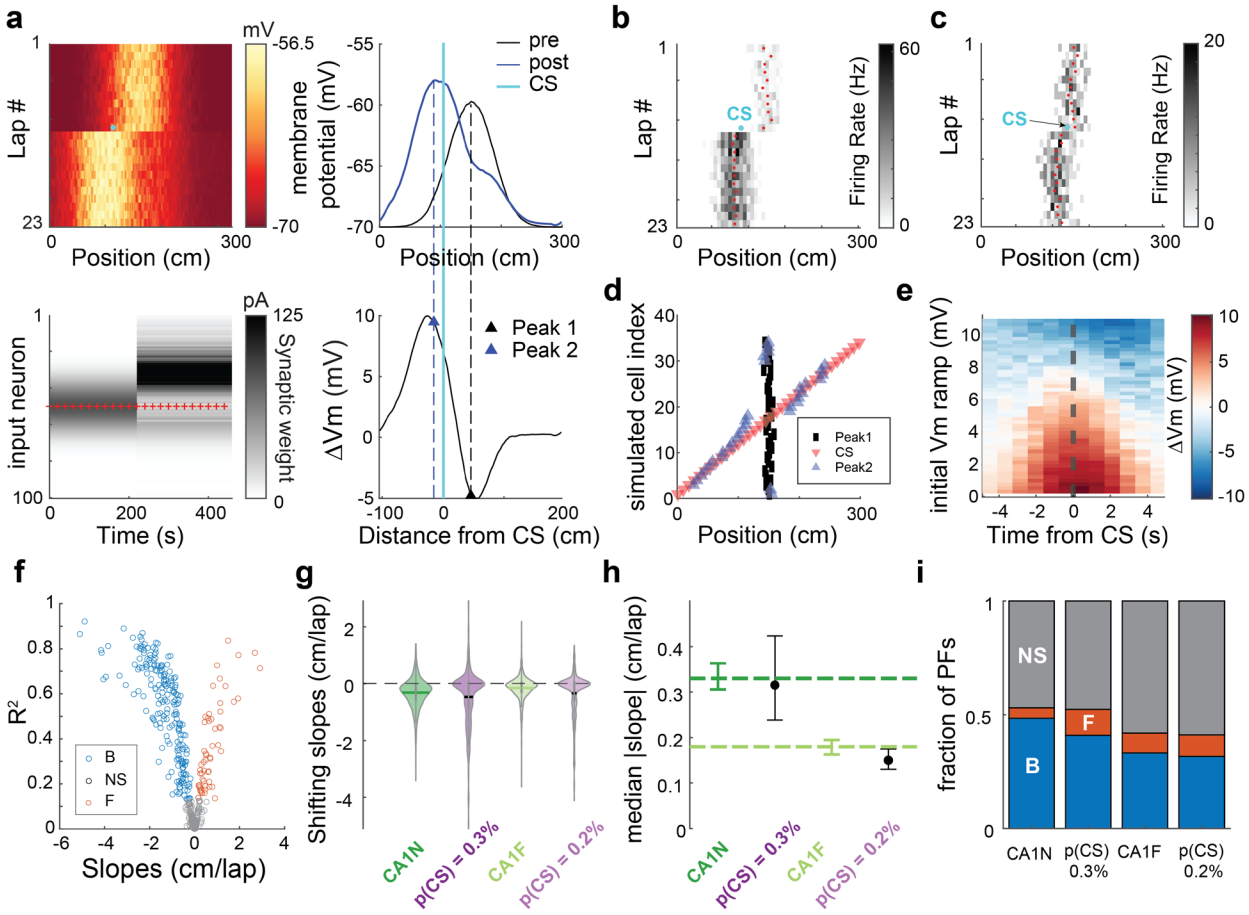

Supplementary Figure 16. (associated to Fig 3.)
BTSP modeled as a homosynaptic weight-dependent bidirectional rule can also cause CA1-like PF shifting.

We adapted the bidirectional model of BTSP developed in Milstein et al. (2021) to our spiking place cell model (baseline parameters, as in Fig 2c, track length = 300cm, animal speed = 15cm/s). Plasticity parameters were selected so that a single CS would lead to PF translocation with realistic firing rates when the CS occurs up to 5s from the current COM (e.g. panel b) and would maintain (i.e. not depress) the PF when the CS occurs close to the current COM (e.g. panel c). See methods. **a.** Simulation of a Milstein-type PF translocation experiment (compare to Fig S13c). On lap 11, a CS (cyan dot) was triggered 3s before initial COM. *NorthWest*: lapwise membrane potential dynamics. *SouthWest*: Synaptic weight dynamics for all inputs. Red plus-signs mark the start of a new lap. *NorthEast*: Smoothed Vm average for the 10 laps before or after CS. *SouthEast*: Difference between the pre-CS and post-CS averages. **b.** PF activity resulting from the simulation described in panel a (CS triggered 3s before initial COM). **c.** Same as panel b but for a CS triggered 0.5s before initial COM. **d.** 34 Milstein-type inductions were simulated as in panel a, varying the time of CS systematically to span the whole track (same as in Fig S15a). PFs are translocated near the CS location, except when the CS is too far from the initial peak (which maintains the initial peak but also produces a new secondary peak near CS). **e.** Changes in Vm ramp (ΔVm, a proxy for synaptic weight change) computed as in Fig S14g and S15g, revealing the weight-dependent bidirectional BTSP rule. **f-i** Simulations of 30-lap PFs with random occurrence of BTSP-triggering CSs, with probability p(CS), as in Fig 3 but using the weight-dependent bidirectional BTSP model from panels a-e. These simulations confirm that BTSP can yield distributions of PF shifts similar to what we observed in CA1, and that differences between novel and familiar conditions can be explained by differences in p(CS). Note that the estimate of p(CS) in the novel condition is lower than the estimate from Fig 3 in part because here firing rates tend to increase (within a realistic range) after a first CS occurrence (see panel B), thus increasing the number of CSs compared to simulations in Fig 3. **f.** Linear regression of the COM of 500 simulated PFs with p(CS) = 0.3%. **g.** Distribution of the regression slopes of the CA1 data (green) and models (purple, 500 samples each). Horizontal green or black bars: mean, whiskers: quartiles. **h.** median absolute slope from the distributions in g, with bootstrapped 95% CI. **i.** Proportions of backward (B), forward (F) and non-significantly (NS) shifting PFs comparing CA1 data and simulations in f-h.

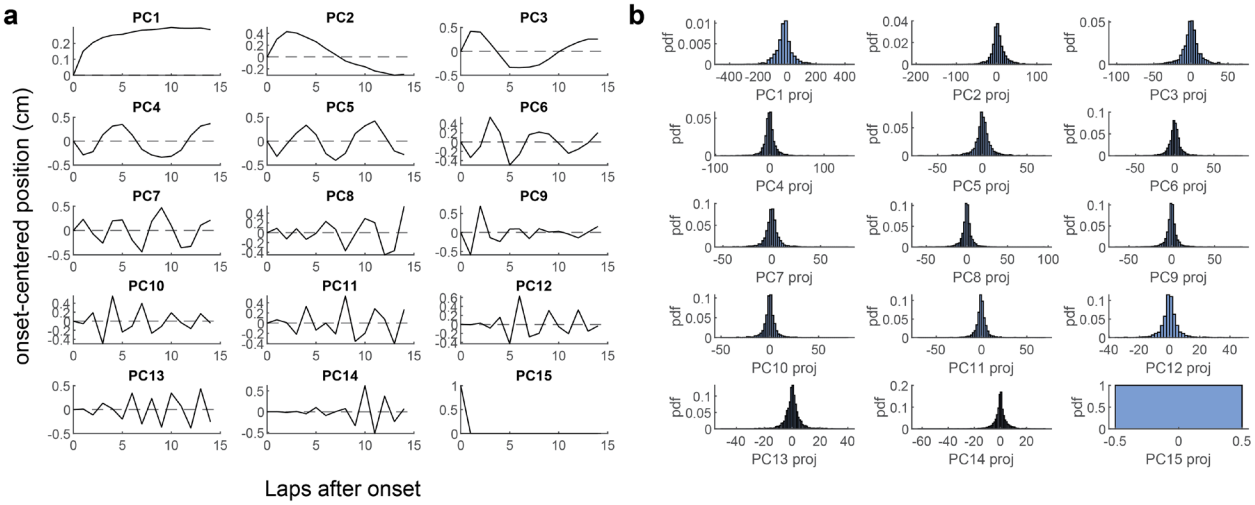

Supplementary Figure 17 (associated to Fig 5).

Principal components and their distribution for all CA1 and CA3 PFs trajectories combined

a. Principal components reveal non-linearities in PF trajectories. See Fig 5b for the explanatory power of each PC.

b. PC scores all follow unimodal distributions, revealing no clusters.

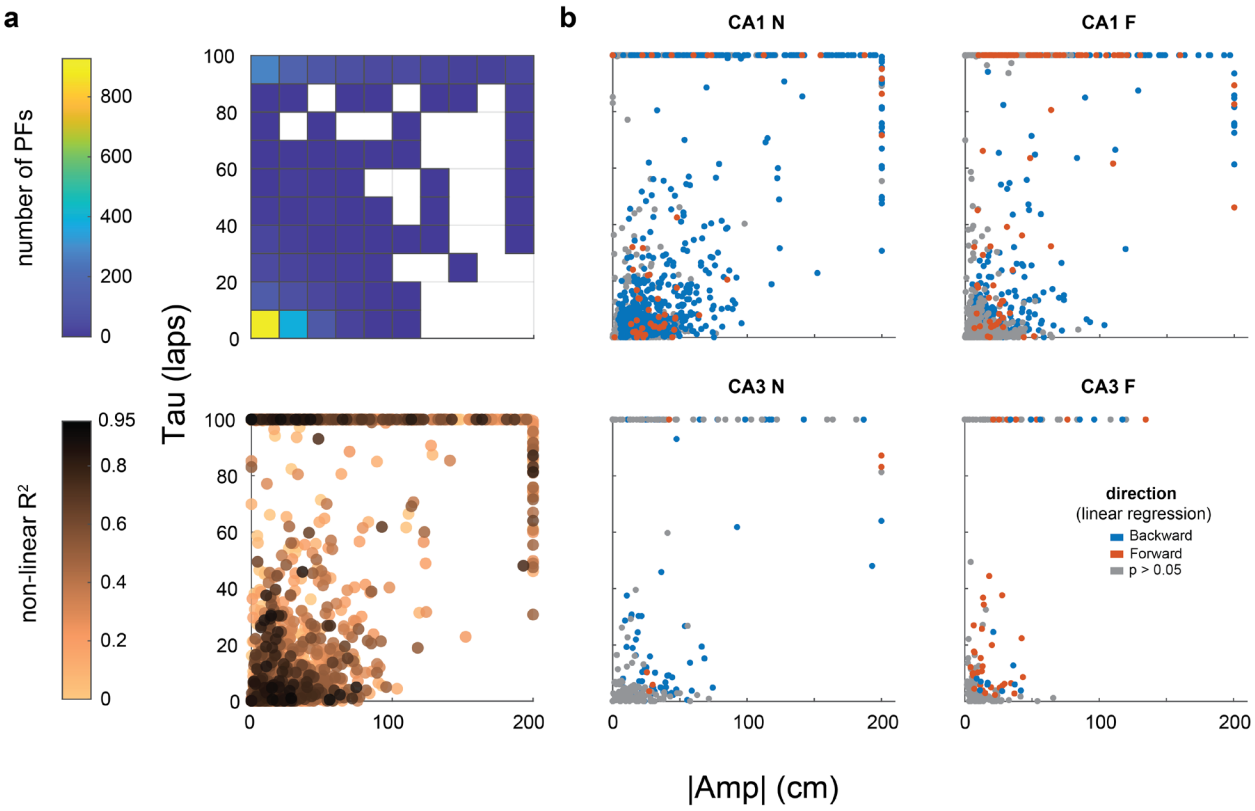

Supplementary Fig 18 (associated to Fig 6). Covariation of the non-linear regression parameters in single PFs

Absolute Amp quantifies the amplitude of the COM shift in respect to the initial position. Large tau values correspond to flat trajectories, i.e. linear shifting (when associated to a large Amp) or stable PFs (when associated to an Amp ~ 0).

a. *Top*: histogram of the number of PFs in each tile of the parameter space. *Bottom*: corresponding scatter plot, each dot corresponding to a single PF. There is not a clear correlation between Amp and Tau but most PFs are concentrated near the origin, with small Taus (<10 laps) and Amps < 40 cm. There is a second cluster with large Tau values corresponding to stable PFs and to PFs with linear-like dynamics. The nonlinear regression produces good fits (R^2) in both clusters. Note that the second group of stable and linear PFs appears as a cluster on the edges because of the fitting procedure that used bounds for |Amp| and Tau at 200 cm and 100 laps respectively.

b. Scatter plots of the non-linear regression parameters for each PFs, grouped by recorded subfield (CA1 or CA3) and environment familiarity (N or F).

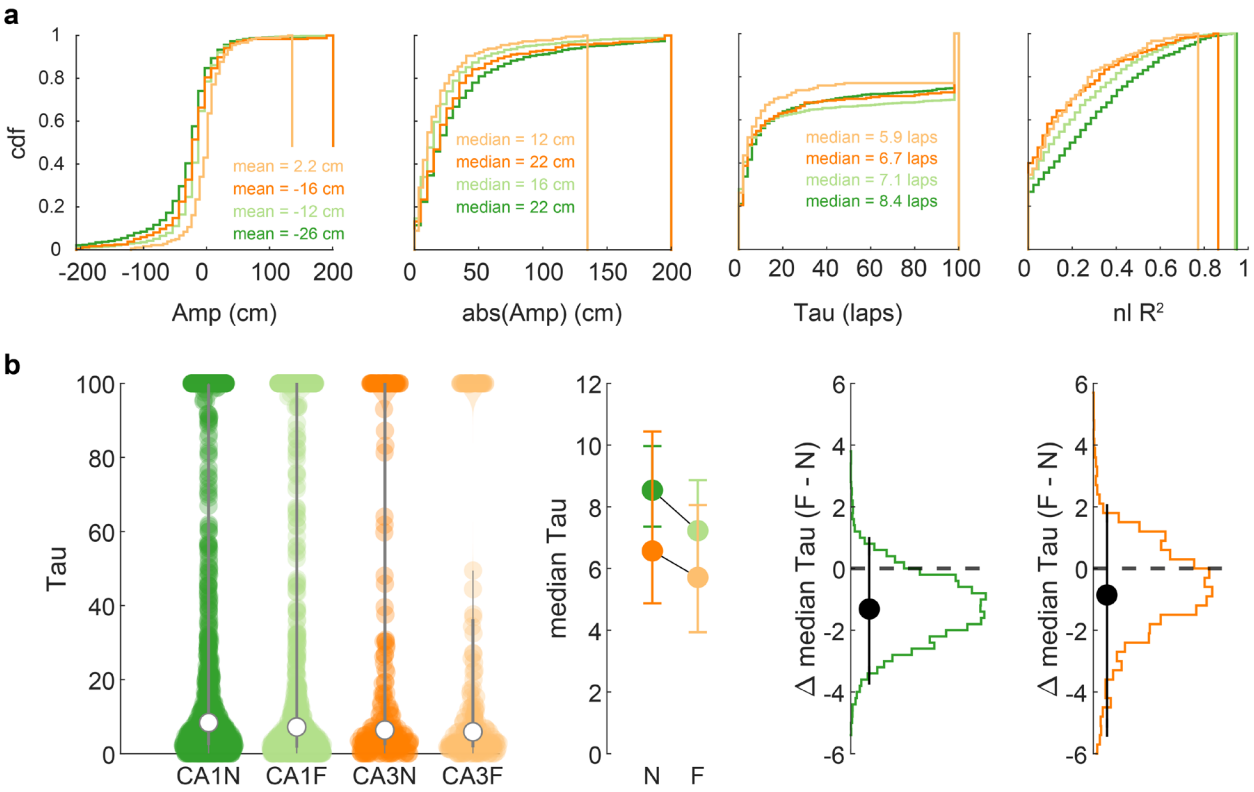

Supplementary Fig 19 (associated to Fig 6).

Distributions of non-linear regression parameters grouped by conditions

a. Cumulative density function estimates of the non-linear regression parameters and the goodness-of-fit (non-linear R-squared) for all PFs grouped by hippocampal subfield and environment familiarity. CA1 green, CA3 orange, lighter shades for familiar tracks.

b. Statistics on the parameter Tau of the nonlinear fits, done as in Fig 6f. *Far Left*: violin plots (same distribution as in panel a middle right), open circles are medians, grey bars quartiles. *Middle left*: Bootstrapped 95% CI of the medians. Right: bootstrapped difference between F and N, for CA1 (middle right) and CA3 (far right). Black error bars = 95% CI of the mean. No significant difference between groups was detected for this parameter. Sample sizes are reported in Fig 1.

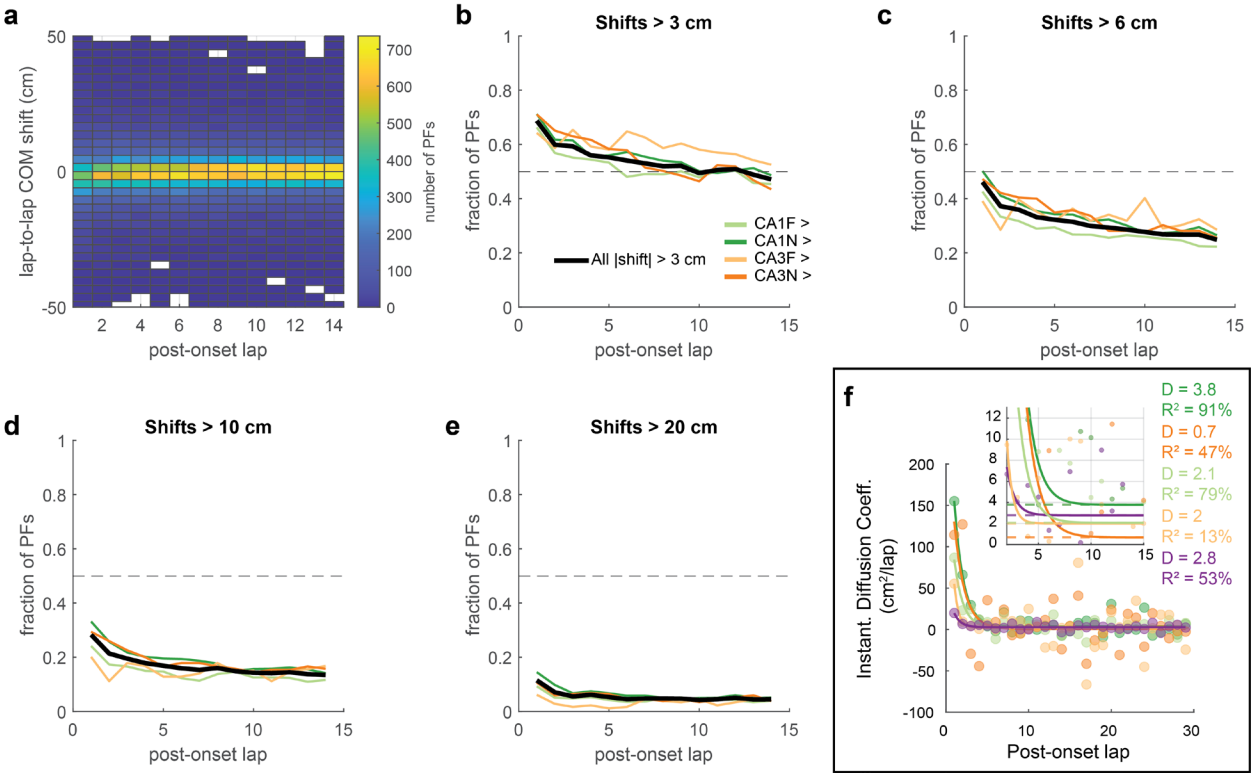

Supplementary Figure 20 (associated to Fig 7). COM shifts after onset

a-e Unsupervised analysis designed to detect whether COM shifts continue to occur long after PF onset. **a.** Distribution of $lap_{n+1} - lap_n$ COM shifts as a function of post-onset laps (based on the 2649 PFs trajectories in Fig. 5a). Automatic uniform binning algorithm. **b.** The proportion of absolute shifts larger than 3 cm (edge of the center bins in a) decreases after onset but stabilizes to a non-zero value. **c-e.** Using larger shift thresholds supports the same conclusion that sizeable shifts are more frequent right after PF onset but their probability relaxes to a positive constant. **f.** Alternative method of estimation of the diffusion coefficient D by fitting the derivative of the mean squared displacement (data points) to a decaying exponential p1*exp(-(x-1)/p2)+p3. The asymptotes (p3, dashed lines) correspond to the steady-state diffusion coefficient D and are similar to estimates in Fig 7c.

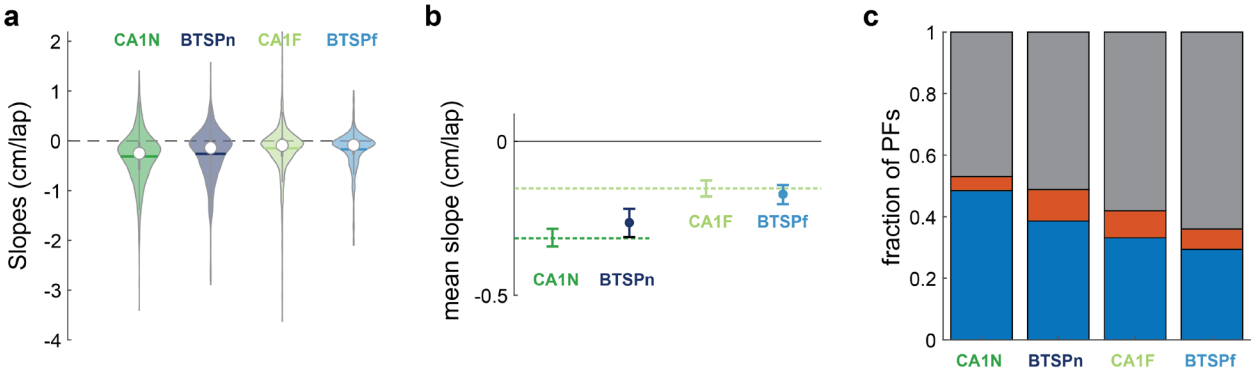

Supplementary Figure 21 (associated to Fig 7)
Linear regression analysis on BTSP models with dynamic p(CS)
BTSPn and BTSPf are models described in Fig 7d that were designed to fit the mean square displacement dynamics observed in the CA1N or CA1F populations of PFs. Here we checked how these two models compared to our findings based on linear regression of the COM (see Fig 1 and 3g). n = 500 PFs for each model. **a-b.** The distributions of linear shifting speeds are similar. **a.** violin plots: distribution, open circles: median, horizontal bars: mean, whiskers: quartiles. **b.** errorbars are bootstrapped 95% CI of the mean. **c.** Although the proportions of backward (blue) and forward (red) linear shifting do not perfectly match the experimental data, they confirm that higher p(CS) (BTSPn) yields more significantly shifting PFs than when p(CS) is lower overall (BTSPf).

Parameter	Value	Parameter	Value	Parameter	Value
Experiment		**Output**		**Synaptic plasticity**	
Animal Speed	15 cm/s	R_m	100 MOhms	Saturating synapses	yes
Track length	300 cm	τ_m	20 ms	$EPSC_{min}$	0 pA
Number of laps	30	V_{rest}	-70 mV	$EPSC_{max}$	85 pA
Inputs		V_{thresh}	-54 mV	$\tau_{prepost}$	20 ms
n_{in}	100 input neurons	V_{reset}	-60 mV	$\tau_{postpre}$	20 ms
Peak FR_{in}	10 Hz	SRA	no	A_{STDP}	0.5% of $EPSC_{max}$
PF_{in} sd	18 cm			Weight update	instantaneous
Connectivity sd	10 input neurons				
W_{max}^{init}	85 pA				
τ_{EPSC}	10 ms				

Supplementary Table 1. Baseline parameters.

	Mehta et al. 2000	**Yu et al. 2006**	**Model 1 (Fig 2c)**
Nb of simulations	not reported	not reported	100
Nb of laps	20	20	30
Track Length (cm)	200	200	300
Speed (cm/s)	50	not reported	15
Inputs			
n_{in} (nb of inputs)	100	1000	100
Neuron Type	Rate (gaussian current)	Poisson spiking from gaussian rate	Poisson spiking from gaussian rate
PF_{in} sd (cm)	12.7 cm	3, 12.7 and 30 cm	18 cm
Peak FR_{in}	\	not reported	10 Hz
Initial Connectivity	Gaussian - unreported SD	Gaussian or Skewed - unreported SD	Gaussian: SD = 10 input neurons.
Synaptic Efficacy (unit)	EPSC (Amps)	unitless G	EPSC (Amps)
Max input	1 nA	not reported	85 pA
Output			
Neuron Type	Rate	Spiking (LIF, parameters unclear)	Spiking (LIF, Song et al. 2000 parameters)
Spike-Rate Adaptation	Yes (Wang 1998 method)	No and Yes (Dayan & Abbott method)	No
Inhibition	Oscillatory (8Hz)	Divisive	No
Peak FRout	high (~50Hz on lap 1)	high (~ 50 to 100Hz)	average (~10 Hz)
Plasticity	STDP	STDP	STDP
Implementation	lap integration	local eligibility (Song et al. 2000)	local eligibility (Song et al. 2000)
A_{STDP} (Max Potentiation)	0.6% of $EPSC_{max}$ = 0.6 pA	0.5% of G_{max}	0.5% of $EPSC_{max}$ = 0.425 pA
Minimum Depression	$-0.9A_{STDP}$ = -0.54 pA	-0.525% of G_{max}	-0.5% of $EPSC_{max}$ = -0.425 pA
Time Constant (ms)	10	20	20
Saturating synapses (Upper Bound)	No	Yes (not reported)	Yes (hard bound : 85 pA)
Weight Update	end of lap	instantaneous	instantaneous

Supplementary Table 2. Comparison of our baseline model with seminal studies
PF width was reported as half-max in the original studies, which we converted to PF sd for comparison (sd = half-max width / 2.355).